DISSERTATION

Processing of Inorganic Silicates for Arduous Environments

by

Jorge Osio-Norgaard

B.S, University of Florida, 2016

M.S. University of Colorado, Boulder, 2019

A dissertation report submitted to the Department of Mechanical Engineering of the University of Colorado, Boulder in partial fulfillment of the requirements for the degree of Doctor of Philosophy, 2022

Committee Members:

Gregory L. Whiting

Rong Long

Mija Hubler

Chelsea Heveran

Carson Bruns

Abstract

Osio-Norgaard, Jorge (Ph.D., Department of Mechanical Engineering)

Processing of Inorganic Silicates for Arduous Environments

Thesis directed by Associate Professor Gregory L. Whiting

The work herein discusses a variety of processing techniques for silicates utilized in the

development of infrastructure. The first half of the work is focused on the chloride durability of

silicious alkali activated cementitious binders, focusing on the chloride binding potential of

zeolitic phases (*i.e.,* chabazite and faujasite) and the use of chemical admixtures to direct their

formation. It is shown that these zeolites can uptake chlorides, and their formation can be

successfully promoted. The second half of the dissertation is focused on in-situ resource

utilization for exploration and habitat building. The work pertains to the development of ceramic

and glass materials, their characterization and manufacture. Sintered ceramics and glasses are

produced via additive manufacturing and conventional sintering and melting methodologies with

properties suitable for construction.

Dedication

When I reflect on the six years of my doctoral career, on the twists and turns I have faced, and the hardships I have overcome I cannot help but think of the people who have made it all possible. This dissertation is a labor of commitment, passion, and love – therefore it should honor those who have made it possible. This work belongs to them as much as it belongs to me, because without them it would be incomplete.

To all my friends, you know who you are, I thank you. Particularly Daniela Blagoeva – thank you for journeying with me for more than a decade towards this accomplishment. I hope we have many more decades ahead of us.

This work is dedicated to Jorgen M. Osio-Norgaard, Ana C. Gabaldon, and Joaquin A. Osio-Norgaard. My dad, mom, and brother.

My parents immigrated to the United States 18 years ago to provide a better life for us. I thank them deeply every day. Even with the struggles of an immigrant's life, they provided us with the tools and access to a remarkable education. During my PhD, they have been the rock that anchors me and motivates me to pursue it until the end – no matter how many times I wanted to quit. During depressive episodes, they have been a beacon of light. They have given me everything, and without them I would not be brave or bold enough to venture forth into the world. So, this work is for you.

To my little brother, you are an inspiration. The family you have created with Stephen and your puppies, the work you have built, the admiration you have gained from those around you have always filled me with inspiration. I love you.

Para mi mama. Sin ti no seria nada. Me has dado el amor incondicional que he necesitado para ser exitoso. No hubiera llegado a alcanzar las estrellas sin tu apoyo. Te amo.

To my dad. You are my hero, inspiration, and best friend. This work is as much yours as it is mine. With you by my side I can overcome any obstacle I face in life, and I can reach any height in the world. I look up to you like I look up to no one else. I hope to be half the man you are one day. I love you.

Contents

Table of Figures

Table of Tables

CHAPTER 1: Introduction

Inorganic silicates are ubiquitous in our interactions with the environment, they are the primary components of the Earth's crust, and they are utilized in a wide variety of applications. From infrastructure to computing, inorganic silicates are used at every level of development. These silicates are often required to meet specific performance targets in arduous environments (*e.g.,* space, chloride rich environments, acid rich environments) that lead to reductions in durability and performance. This works seeks to address the processing of inorganic silicates for improved performance in arduous environments. Particularly, it seeks to address the chloride durability of alkali activated cements (AAC) and the manufacture of materials for off-planet applications from in-situ resources (ISRU). The first half of this work will focus on chloride transport in AACs particularly on the role and formation of aluminosilicate zeolites in the process of chloride transport. The second half of the work will focus on the development and processing of ceramic and glass materials for space applications. This chapter will introduce AAC and ISRU to facilitate the understanding of the processes described within.

1.0 Alkali Activated Cements

Aluminosilicate AACs are a family of novel cementitious binders that seek to, in part, replace traditional ordinary portland cement (OPC) concrete. OPC concrete produces 8% of all CO_2 emissions worldwide and suffers from a myriad of durability issues that lead to the decay of infrastructure [1,2]. AAC concretes provide a lower carbon, higher durability alternative to OPC concrete that could effectively increase the service life of structures [1-3]. AACs are different from OPC in a variety of ways, from their chemical composition to their activation and performance. Unlike OPC, which requires only water to begin its hydration reaction, AACs require the use of

an alkaline activator (*e.g.*, NaOH) to begin the cementation process [2]. AACs can be broadly divided into two categories: high calcium and low calcium. This distinction refers to the chemical composition of the precursor powders and their calcium content. This work deals primarily with low calcium metakaolin based AACs. These low-calcium AACs present a unique set of durability benefits and challenges in various arduous environments. To better understand this material, a brief discussion of its reaction kinetics is provided.

AAC reaction kinetics are complex and there are many models utilized to describe them, however they can be broadly described in terms of dissolution and reorientation, and gel formation [2]. Initially the alkali activator is added to the precursor powder, beginning the process of dissolution by breaking the covalent Si-O-Si and Al-O-Si bonds [2]. This process occurs simultaneously with the process of orientation and polycondensation where an amorphous network begins to form, similarly to the process by which zeolites are formed [2]. **Figure 1** from [4] provides a schematic of the reaction kinetics of ACCs, showing that in addition to amorphous aluminosilicate gel nanocrystalline zeolite phases can form in these cements. The formation of these zeolite phases has been widely discussed in [5,6] and in **chapter 5** of this work.
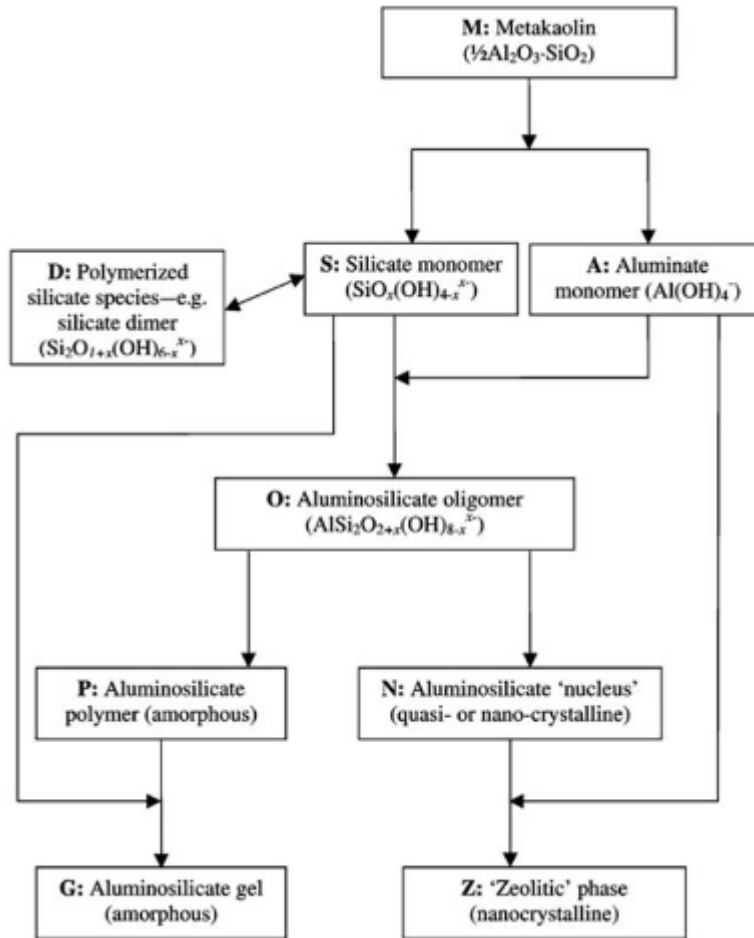
Figure 1: Schematic of AAC reaction kinetics, adapted from [4]

During the service life of a structure, it is exposed to a variety of arduous environments over a period of decades. Structures face a variety of chemical attacks from environmental and man-made sources with some examples being exposure to ocean chlorides, de-icing salts, sewage water, soil sulfates, and acid run off [3,7]. Each of these exposures to arduous environments affects either the structure of the aluminosilicate gel, its pore solution, or the reinforcing steel inside the AAC concrete. This work has chosen to focus on chloride transport in AACs, particularly on the role of the zeolitic phases in the process, which will be extensively discussed in **chapters 5**.

1.1 A Note on Cement Chemistry Conventions

Chapters 3 and 5 are focused on the chemistry of alkali activated cements, therefore cement

chemistry conventions are used to refer to reaction products. Cement chemistry conventions are

utilized to simplify the complex nature of cement products to convey the structure of the

materials more easily. **Table 1** provides a quick notation guide.

Table 1: Cement Chemistry Notation.

Compound	Cement Chemistry Notation
Calcium Oxide (CaO)	C
Silicon Dioxide (SiO_2)	S
Aluminum Oxide (Al_2O_3)	A
Potassium Oxide (K_2O)	K
Sodium Oxide (Na_2O)	N
Water (H_2O)	H

For example, **chapter 3** often refers to (C,N)-A-S-H gels, this stands for a "calcium/sodium

alumino-silicate hydrate" a series of gels that exist in the CaO-Na_2O-Al_2O_3-SiO_2 phase diagram.

2.0 In-Situ Resource Utilization

In-situ Resource Utilization (ISRU) leverages available lunar regolith, a primarily

silicious mineral, to produce the materials necessary for lunar exploration and colonization.

Lunar regolith is a mixture of mineral fragments, impact melt glasses and beads, agglutinates and

volcanic glasses in layers varying from 4-12 meters in depth, depending on the lunar region [8].

There are generally two categories of regolith available for ISRU Mare and Highland. These two

types of regolith (although still primarily silicious) have some distinctive features that make

them desirable for ISRU for example, Mare regolith contains the mineral ilmenite a possible

candidate for water and oxygen extraction [8,9].

There are many proposed approaches to ISRU ranging from various disciplines to produce oxygen, chemicals, metals, cements, ceramics, solar panels, and all other required necessities for a lunar base [10–14]. This work seeks to focus on the production of cements, ceramics, and glasses for the development of lunar habitats therefore it will briefly discuss the relevant developments in the field.

Various cement chemistries have been proposed for lunar ISRU applications, here we will briefly discuss the types of chemistries proposed and some of the studies associated with them. Traditional OPC concrete is one of the candidates for ISRU habitat development, in 2005 Khoshnevis et al. proposed a large scale direct ink writing additive manufacturing approach to OPC concrete for ISRU habitat development [15]. Terming it Lunar Contour Crafting, Khoshnevis developed a large scale OPC concrete printer that produced large scale high fidelity parts and proposed strengthening the OPC concrete utilizing glass fiber and other materials to improve the strength of the structures [15]. In addition to additive manufacturing techniques, OPC has been blended with regolith simulants the resulting properties have been studied [16]. Regolith has the potential to act like a pozzolanic material, but it is low reactivity and generally serves as filler [16]. Greater reactivity could be achieved by further reducing the regolith particle size potentially improving the strength of OPC [16]. Additionally, the microstructural development of OPC constituent tri-calcium silicate has been studied in microgravity, showing that lower gravity environments increase the porosity of the material, potentially leading to weaker compressive strengths [17].

In addition to OPC, geopolymers have been explored as binders for space exploration and have been tested in various conditions. Geopolymers have been manufactured out of BH-2 lunar simulant and cured under vacuum at lunar day temperatures which proved to be beneficial to

strength development [18]. Further studies have been conducted with BH-1 lunar simulant demonstrating that the rheology and reactivity of lunar geopolymers can be affected by the addition of alumina and other compounds [19]. Additional studies into geopolymers have been conducted yielding materials with acceptable compressive strengths and achievable chemistries making them feasible materials for space exploration [18–21].

One of the most widely proposed approaches to ISRU is the sintering of lunar regolith. Sintering lunar regolith produces hard ceramic-like materials with a range of compressive strengths ranging from insufficient for lunar construction, to exceeding the compressive strengths of concrete [14,22–25]. Various sintering mechanisms have been proposed ranging from techniques to additively manufacture structures to be subsequently sintered like in [26], and the work completed in **chapter 6** and techniques to directly sinter the lunar regolith [14,27–32]. Two popular approaches are microwave sintering and selective laser sintering, these approaches leverage low-energy devices to hear regolith to approximately 1100°C a suitable sintering temperature, right below the melting point of the material [28,30,33,34]. These elements leverage a minimalist approach to ISRU where the only material needed for construction is the regolith itself.

CHAPTER 2: Instrumentation and Processing

Chapter 2 presents a brief review of some characterization and processing techniques utilized to investigated and modify the inorganic silicates utilized in this dissertation. Additionally, chapter two discusses how the characterization techniques provide useful information to probe the process-structure-property relationships of the materials investigated.

1.0 Characterization Techniques

1.1 X-ray Diffraction

X-ray diffraction is a technique that utilizes X-rays as a means to assess the crystal structure of a material [35]. This technique can be utilized to identify unknown materials by matching their diffractograms to existing patterns, or to obtain valuable information related to the crystal structure, crystalline quality, orientation, and internal stress of the material [35]. This process is possible due to the nature of the interactions between X-rays and matter relying on X-rays waves diffracting off the periodic structure of a crystalline material [35]. Diffraction occurs when a wave (of any kind) interacts with an obstacle, waves interacting with a periodic structure will separate into multiple waves traversing different directions [35]. When the X-rays scattered by the atoms are in phase, constructive interference occurs leading to intensity peaks that describe the crystal structure of the material [35]. These peaks can used to characterize the material and to determine what minerals or structures are in it.

In this work XRD is utilized primarily to characterize the formation, and changes to various minerals in inorganic silicate systems. XRD is used to assess the crystallinity of various cements, ceramics, and glasses with the goal of better understanding their other properties. XRD

will yield insights into the process-structure-property relationships for these materials, such as the relationship between zeolite formation and the permeable porosity of alkali-activated cements in **chapter 5**.

1.2 Scanning Electron Microscopy, Energy Dispersive Spectroscopy & Wavelength Dispersive Spectroscopy

Scanning Electron Microscopy (SEM) is a technique primarily used to characterize the surface morphology and microstructure of various bulk materials [36]. Characterizing the morphology and microstructure of various materials becomes important in attempting to determine their composition and properties. SEM relies on a high energy electron beam, scanning across the surface to produce electron-specimen interactions which are then processed through a series of electromagnetic lenses and reconstituted into a grey-scale image for analysis [36]. Additionally, the electron beam-specimen interactions produce a series of X-rays that can be utilized to further characterize the surface of the bulk material [36]. These X-rays are utilized in both Energy Dispersive Spectroscopy (EDS) and Wavelength Dispersive Spectroscopy (WDS) techniques that can be used to both qualitatively and quantitatively determine elemental composition. In both techniques X-rays emitted from the surface of the material are captured in a detector from these characteristic X-rays the elemental composition of a material can be determined.

SEM along with EDS/WDS are commonly used in work with inorganic silicates to characterize the microstructure and composition of cementitious binders [6,37], yielding important information about the various phases found within the material. Additionally, WDS has been utilized to characterize the intrusion of harmful substances into the cementitious matrix to assess its durability [38]. In some of the work presented EDS & WDS are utilized to determine the

presence of bound chlorines in inorganic silicates, while SEM is utilized to demonstrate the morphology of inorganic silicate glasses.

1.3 Isothermal Conduction Calorimetry

Isothermal conduction calorimetry (ICC) is a technique utilized to measure the heat flow occurring during a chemical reaction. ICC leverages an isothermal environment to accurately assess the endo/exothermicity of a given reaction. The heat flow curves produced during these tests can then be interpreted to obtain points of interest during the measured reaction period. **Figure 2** shows a sample ICC curve for a cementitious binder. In the curve, several exothermic (positive) peaks can be observed. In cementitious binders these peaks indicate the dissolution of cement and the formation of various amorphous and crystalline phases within the cementitious binder [39–41]. These peaks are often not sufficient to fully characterize the material, as all they reveal is the presence of an endothermic or exothermic reaction, however, this technique paired with other characterization techniques such as X-ray diffraction can yield useful information. In this text, ICC is paired with X-ray diffraction to identify the formation of target minerals in a cementitious system, as these minerals for during an exothermic reaction. By observing the exothermic peaks in the ICC curves, we detect the formation of target zeolites, and particularly the age at which they form.
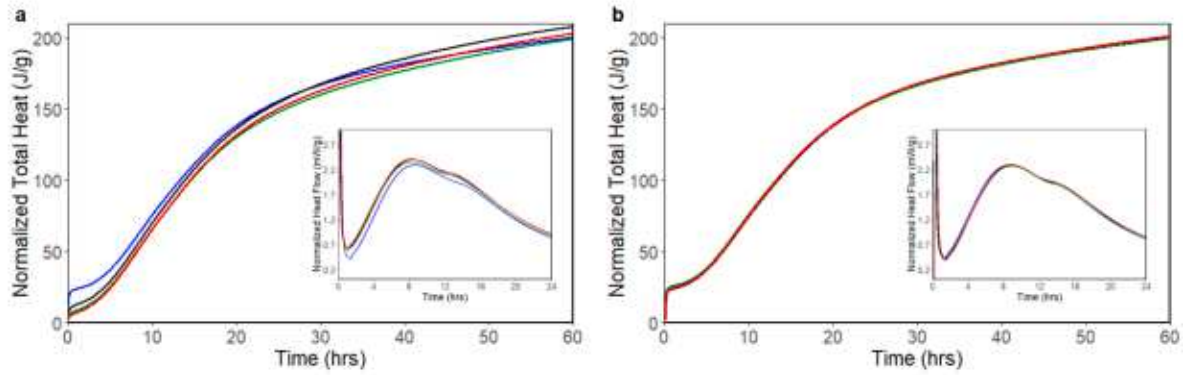
Figure 2: Sample ICC curve for a cementitious binder, total heat generated with insert indicating heat flow over time, reproduced from [42].

1.4 Nanoindentation

Nanoindentation is a characterization technique that allows for the determination of the micromechanical properties of a material. This technique utilizes a diamond tip that presses into a material leading to a displacement which is subsequently recorded [43]. Nanoindenters are often utilized to measure the modulus and hardness of a material, typically assuming elastic-plastic contact [43]. This assumption allows for analysis of the unloading curve which is used to determine stiffness, a measurement that is subsequently converted into a reduced modulus of indentation [43].

Indenters use a variety of different tips to extract modulus data, ranging from a pyramidal Vickers tip to a three-sided pyramidal Berkovich tip. A typical curve generated from indenting a material shows the loading and unloading behavior on the material, presenting load versus depth. Unloading curves from the indentation tests are typically analyzed by the methods put forth by Sneddon, and Oliver and Pharr [44]. These curves should be fit by the equation (1) where B, h_p and m are best fit constants, associated with the indent left on the sample, and depending on indenter shape and the plasticity of the material [44].

$$P(h) = B(h - h_p)^m \quad (1)$$

10

The modulus of the specimen can be related to the reduced modulus by equation (2)

$$\frac{1}{E_r} = \frac{1 - v_s^2}{E} + \frac{1 - v_i^2}{E_i} \ (2)$$

Where E is the modulus of the specimen, i represents indenter properties, and v represents the Poisson's ratios of the specimen and the indenter.

2.0 Processing Techniques

2.1 Chemical Admixtures

In inorganic silicate systems chemical admixtures are often employed to adjust or tailor material properties to meet the desired performance targets. In the manufacture of zeolites (alumino-silicate minerals), structure directing agents (SDA) are used to produce target zeolites (*e.g.,* Chabazite). These SDA are often organic positively charged molecules with desirable properties that are added during the synthesis process to facilitate the structuring of silicates into the target zeolites. Chemical admixtures are also utilized in the cement industry, where water reducing agents, set retardants, set accelerators, and plasticizers are commonly utilized to alter the properties of the cementitious system. These chemical admixtures are utilized to modify the fresh and hardened state properties of cement to facilitate its placement. Lastly, glasses are often modified by the addition of minerals and oxides during the melting process. These additions lead to a variety of improved properties (e.g. transparency, strength). This work showcases the addition of various chemical admixtures to silicate systems, from SDA, to MgO, and TiO_2 to improve cementitious binders, ceramics, and glasses. The addition of these chemical admixtures targets to alter the minerology or improve the reactivity of the systems and it is showcased in **chapter 5, 6** and **7**

2.2 Sintering

One of the studies within utilizes sintering to fabricate strong silica-based ceramic parts for space applications. Sintering is a process by which a solid material is formed through the heating and quasi melting of a powder material. In **chapter 6** we utilize sintering to transform a magnesium oxychloride-simulated lunar regolith cement into a ceramic material. Sintering of additively manufactured powder parts in theory would increase strength, reduce porosity, and improve other properties. **Figure 3** shows a diagram of the sintering process.
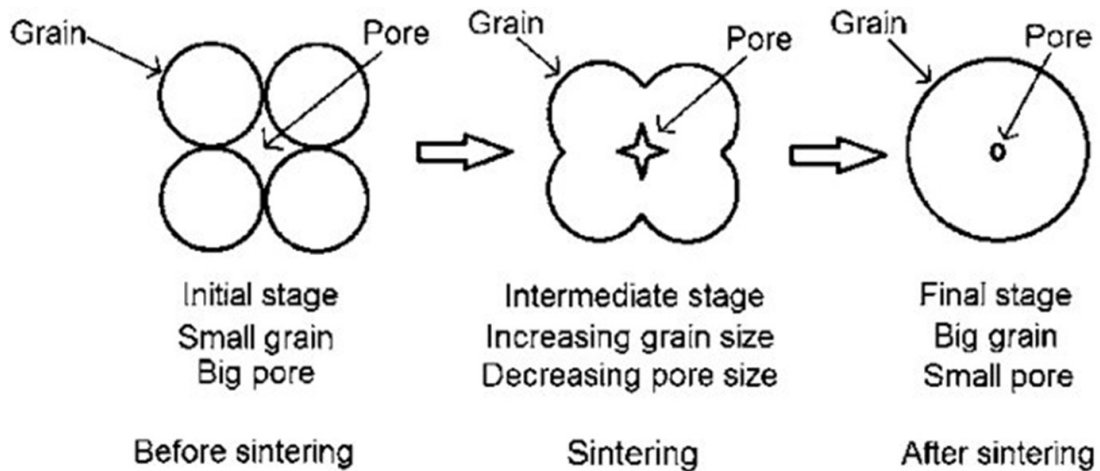
Figure 3: Powder sintering process reducing porosity [45].

2.3 Powder Binding Jetting Printing

Powder binding jetting (PBJ) printing is an additive manufacturing technique that utilizes both powder and a binding agent to produce complex 3-dimensional shapes. PBJ printing utilizes a powder reservoir that releases a layer of powder into a print bed, after that layer of powder has been spread by a roller a binding agent is applied on top of the layer. Subsequently another layer of powder is rolled on top of the moistened layer and the process is repeated. **Figure 4** shows a layer of powder being spread by a roller. PBJ printing is utilized in one of the studies within to produce complex shapes for sintering applications.
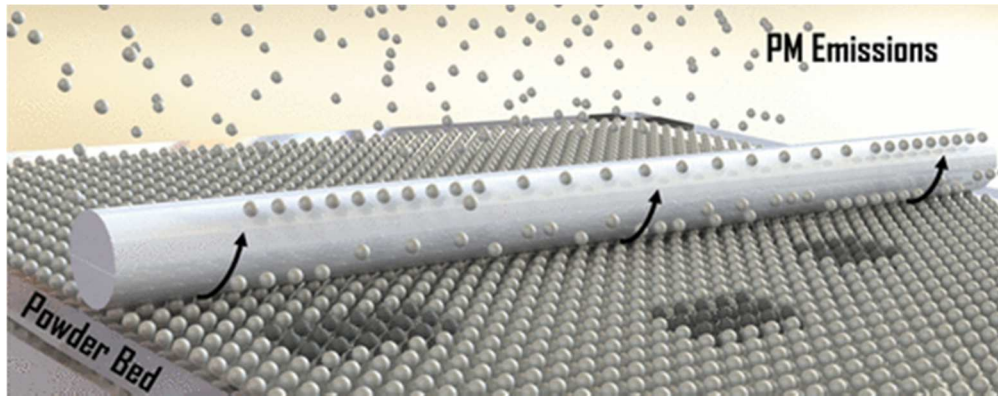
Figure 4: Powder Binding Jetting Printer, layer and roller to spread the powder [46].

CHAPTER 3: A Review of Chloride Transport in Alkali-Activated Cement Paste, Mortar, and Concrete

Chapter 3 presents a comprehensive review and meta-analysis of chloride transport in alkali-activated cements, a silicious material utilized in building construction. Chloride heavy environments are considered highly hostile to reinforced-steel concrete structures as these environments corrode the reinforcing steel, impacting the structural integrity of the material. This chapter assesses the main factors governing chloride transport in these cementitious systems. This chapter has been published in the journal *Construction and Building Materials* under the following citation: J. Osio-Norgaard, J. P. Gevaudan, and W. V. Srubar, "A review of chloride transport in alkali-activated cement paste, mortar, and concrete," *Constr. Build. Mater.*, vol. 186, pp. 191–206, Oct. 2018, doi: 10.1016/J.CONBUILDMAT.2018.07.119.

Abstract

In this review, we present a meta-analysis of experimental data concerning chloride transport in alkali-activated cement (AAC) paste, mortar, and concrete. Sixty-six (66) studies were reviewed with a primary focus on measurement methodology, mixture design, and process-structure-property relationships related to microstructural development (i.e., porosity, pore size distribution), chloride diffusion, and chloride binding. In general, this review elucidates that aluminosilicate precursors with high amorphous content and increased fineness and activating solutions with high alkalinities (Na:Al $\geq$ 0.75) and silica contents (Si:Al $\geq$ 1.5) in combination with heat curing (>40°C) lead to microstructural characteristics (e.g., binder gel chemistries) that improve chloride durability, even though interactions between these factors are not well understood. Descriptive statistics of reported AAC paste porosities and AAC concrete chloride diffusion coefficients by aluminosilicate precursor (i.e., fly ash, slag, calcined clay, natural clay,

binary blends) are presented, along with a summative discussion regarding new opportunities for advancing current scientific understanding of chloride transport in AACs.

Keywords: Alkali-activated cements; porosity; chloride transport.

1.0 Introduction

Chloride-induced corrosion is a pervasive durability issue that continues to plague reinforced concrete structures worldwide. Approximately 3.4% of the global GDP ($2.5 Trillion USD) is spent each year to prevent, mitigate, and repair civil infrastructure damage due to chloride-induced corrosion [47]. Waterborne and airborne chlorides in marine environments and chlorides from surface-applied deicing salts exacerbate risks of chloride-induced depassivation and subsequent corrosion of mild steel in reinforced concrete structures. Fortuitously, the alkaline pore solution of ordinary portland cement (OPC) paste induces chemical passivation of mild steel at early ages by creating a thin, dense, self-protective layer of iron oxides and hydroxides [48]. However, transport of chloride ions through the cementitious matrix and its resulting accumulation at the steel surface can depassivate this protective layer. Chloride anions react with metal cations, creating corrosion products and liberating protons that result in a more local acidic environment, promoting further depassivation.

Alkali-activated cements (AACs) have emerged as a potential alternative to OPC in recent years because of comparable—and occasionally superior—mechanical and durability properties and potentially lower environmental impacts [2,7,49]. AACs are synthesized by dissolving an aluminosilicate material (e.g., fly ash, slag, metakaolin) in a highly alkaline solution, most often in the presence of soluble silicates [50]. Precursor dissolution enables gelation and subsequent formation of an inorganic aluminosilicate polymer comprised of silica and alumina tetrahedra linked in three dimensions [49,51]. For a comprehensive review of AACs and

15

more detailed information regarding their synthesis, microstructure, and material properties, see [2,49]. Other helpful reviews concerning the durability of AAC materials include [5], [8], [9], and [7,52–54].

The objective of this work—and what distinguishes it from prior literature reviews—is to provide a comprehensive overview of the process-structure-property relationships of AACs as they pertain to chloride transport. <u>Sixty-six (66) studies were reviewed with a primary focus on measurement methodology, mixture design, and process-structure-property relationships related to microstructural development (i.e., porosity, pore size distribution), chloride diffusion, and chloride binding. These studies were selected because they explicitly investigated how physical and chemical properties of aluminosilicate precursors, activator content, and/or other processing parameters impact microstructural development and properties that affect chloride transport in AAC paste, mortar, and/or concrete.</u> The content of this review is organized into the following main topics: (1) chloride transport mechanisms and characterization methods, (2) factors that influence microstructural development and material properties that affect chloride transport in AACs, (3) a meta-analysis of published experimental data, and (4) limitations of characterization methods for chloride intrusion in AAC paste, mortar, and concrete. We conclude this review by highlighting challenges, limitations, and future opportunities to advance scientific understanding of chloride transport in AACs.

2.0 Mechanisms and Measurement of Chloride Transport in AACs

Chloride transport through porous cementitious materials is governed by three primary mechanisms: hydrostatic pressure, capillary absorption, and diffusion. Hydrostatic pressure drives chloride ions into the cement matrix by pressure gradients. If a hydraulic head of seawater is applied to a concrete surface, for example, chlorides will penetrate the surface [55]. In contrast,

capillary absorption is driven by small intermolecular forces within the pores sized in the 10nm-10µm range, enabling absorption of ionic liquids without assistance from external forces. Chloride ions also diffuse through cementitious media *via* concentration gradients. Provided that the concrete is sufficiently saturated (>80%) [56], high concentrations of chloride ions will diffuse into the bulk through all interconnected pores where there is an initially lower concentration of chloride ions.

Hardened-state material properties, including porosity, pore solution chemistry, pore size distribution, tortuosity, and chloride binding potential, are well known to affect the rate of chloride transport in cementitious materials [55], and although their measurement has been standardized for OPC concrete, oftentimes all of them are not assessed in one study. Standard characterization methods for ion transport in AAC concrete, however, are much less established. While AAC-specific tests and protocols for chloride ion transport are still emerging (see **Section 4**), early attempts at understanding mechanisms that underlie/influence these effects have been adapted from tests developed for OPC concrete. Specifically, these tests (see **Table 2**) include direct and indirect physical tests (i.e., sorptivity, porosimetry, permeability, water absorption), chemical tests (i.e., chloride penetration), and electrical tests (i.e., resistivity). Indirect physical tests focus on microstructural characterization (i.e., pore size, total porosity) or utilize proxy measurements (i.e., water absorption, permeability) and relate these properties to durability. While indicative of microstructural characteristics, these physical tests cannot directly measure chloride diffusion or chloride resistance, but they are a useful way to estimate how AACs may perform in the presence of an ionic chloride solution. Chemical tests (e.g., chloride ponding) are often used to directly assess (1) time-dependent chloride penetration, (2) chloride content through the sample thickness using an indicator such as $AgNO_3$, and (3) chloride binding using

solubility techniques [57,58]. From these tests, a diffusion rate (i.e., diffusion coefficient) can be

calculated. Lastly, resistivity methods are utilized to provide a quantitative measure chloride ion

transport, where decreased resistivity indicates higher degrees of chloride penetration. As is

further discussed in the context of our statistical analysis of reviewed literature in **Section 4**, each

of these methodologies has inherent limitations in their measurement that must be understood so

as to not obfuscate understanding of chloride intrusion in AACs.

Table 2: Summary aluminosilicate precursors[1], activators, and characterization methods[2] of properties that affect chloride transport in AAC paste, mortar, and concrete, as well as preconditioning regimes[3] performed prior to their measurement.

AUTHOR(S)	YEA-R	PRECURSOR(S)	ACTIVATOR(S)	PORE STRUCTURE	CHLORIDE DIFFUSION	CHLORIDE BINDING	PRECONDITIONING REGIME(S)	REF
AAC PASTE								
BAKHAREV ET AL.	2005	FA	NaOH + NaSi + KOH	BET	N/A	N/A	N/A	59
KOVALCHUCK ET AL.	2006	FA	NaOH + NaSi	MIP	N/A	N/A	OD (105°C)	60
SKAVARA ET AL.	2009	FA	NaOH + NaSi	MIP	N/A	N/A	N/A	61
WINNEFELD ET AL.	2010	FA	NaOH + NaSi	SEM†	N/A	N/A	N/A	62
MA ET AL.	2013	FA	NaOH + NaSi	MIP	N/A	N/A	Vacuum Freeze Dry	63
HLAVACEK ET AL.	2014	FA	NaOH + NaSi	Paste Bulk Density	N/A	N/A	N/A	64
ROY ET AL.	2000	S	NaOH + KOH + Na$_2$SO$_4$ + Na$_2$CO$_3$	MIP	In house diffusivity	N/A	N/A	65
COLLINS ET AL.	2000	S	NaSi + Lime	MIP	N/A	N/A	N/A	66
MELO ET AL.	2008	S	NaSi	MIP	N/A	N/A	ASTM D4404	67
BEN HAHA ET AL.	2011	S	NaOH + NaSi	SEM†	N/A	N/A	N/A	68
BEN HAHA ET AL.	2011	S	NaOH + NaSi	SEM†	N/A	N/A	N/A	69
PUERTAS ET AL.	2011	S	NaOH + NaSi	N/A	N/A	N/A	N/A	70
YE ET AL.	2017	S	NaOH + NaSi	MIP	N/A	N/A	Vacuum Dry (50°C) + OD (105°C)	71
ORTEGA, ET AL.	2000	UC	Ca(OH)$_2$	Water Absorption	N/A	N/A	OD (105°C)	72
DUXSON ET AL.	2005	MK	NaOH + SiO	BET	N/A	N/A	100°C	73
GEVAUDAN ET AL.	2017	MK	NaOH + NaSi	Modified A	N/A	N/A	Solvent exchange, OD (°C)	6
PAN ET AL.	2003	Binary (S+Red Mud)	NaSi + Sodium Aluminate	MIP	Ponding	N/A	N/A	74

LLOYD ET AL.	2010	Binary (FA+S), FA	NaOH + KOH + NaSi	Water Absorption	In house diffusivity	N/A	N/A	[75]
ZHANG ET AL.	2010	Binary (FA+MK), FA	NaOH + NaSi	MIP + BET	N/A	N/A	Solvent Exchange, OD (°C)	[76]
PROVIS ET AL.	2012	Binary (FA+S), FA	NaSi	µCT	N/A	N/A	N/A	[77]
ZHU ET AL.	2014	Binary (S+FA)	NaOH + NaSi	MIP, Water Absorption	Ponding	N/A	OD (65°C)	[78]
ISMAIL ET AL.	2014	Binary (S+FA)	NaSi	SEM[†]	N/A	N/A	N/A	[79]
YANG ET AL.	2014	Binary (S+FA)	NaOH + NaSi	MIP, Water Absorption	Short Term Salt Ponding	N/A	OD (105°C)	[80]
LEE ET AL.	2016	Binary (S+FA)	NaOH + NaSi	B, C	D, E	Acid-soluble chlorides	N/A	[57]
YAO ET AL.	2016	Binary (S+FA)	NaOH + NaSi	MIP	N/A	N/A	Solvent Exchange + OD (60°C)	[81]
NOOR-UL-AMIN ET AL.	2017	Binary (Bagasse ash+UC)	NaSi	N/A	Ponding	N/A	N/A	[82]
LONG ET AL.	2017	Binary (S+FA)	NaSi	µCT	N/A	N/A	N/A	[83]
REN ET AL.	2017	Binary, Ternary	NaOH + NaSi	MIP	Ponding	N/A	OD (105°C)	[84]
AAC MORTAR								
MIRANDA ET AL.	2005	FA	NaOH + NaSi	SEM[†]	N/A	N/A	N/A	[85]
CRIADO ET AL.	2011	FA	NaOH + NaSi	MIP	N/A	N/A	N/A	[86]
ASPROGERAKAS ET	2014	FA	NaOH + NaSi	N/A	NT Build 443	N/A	N/A	[87]
MONTICELLI ET AL.	2016	FA	NaOH + NaSi	MIP	F	D	N/A	[58]
MONTICELLI ET AL.	2016	FA	NaOH + NaSi	MIP, EN1015	Ponding	N/A	N/A	[88]
SHI ET AL.	1996	S	NaOH + Na$_2$CO$_3$ + NaSi	MIP	A	N/A	N/A	[89]
BROUGH ET AL.	2002	S	NaSi	SEM[†]	N/A	N/A	N/A	[90]
ZUDA ET AL.	2007	S	NaSi	Water Absorption	Bulk Diffusivity	N/A	N/A	[91]
AYDIN ET AL.	2012	S	NaOH + NaSi	N/A	N/A	N/A	N/A	[92]
PALOMO ET AL.	1999	MK	NaOH + NaSi	Water Absorption	N/A	N/A	N/A	[93]
CHI ET AL.	2013	Binary (S+FA), S	NaOH + NaSi	B	N/A	N/A	N/A	[94]
ISMAIL ET AL.	2013	Binary (S+FA), S	NaSi	B	E, G	D	OD (60°C)	[95]
ZHU ET AL.	2014	Binary (S+FA), S	NaOH + NaSi	MIP, Water Absorption	Ponding	N/A	OD (65°C)	[78]
KARIM ET AL.	2017	Ternary	NaOH	B, BS EN196	JIS A6203	N/A	N/A	[96]
AAC CONCRETE								

	Year							
ARHAM ET AL.	2009	FA	NaOH + NaSi	C	A, G, AASHTO T 259	N/A	OD (105°C)	[97]
KUPWADE-PATIL ET	2013	FA	NaOH + NaSi	MIP	A, D	N/A	N/A	[98]
CHINDRAPRASIRT ET	2014	FA	NaOH + NaSi	N/A	D, E	N/A	N/A	[99]
LAW ET AL.	2014	FA	NaOH + NaSi	N/A	A, AASHTO T259 & T277	N/A	N/A	[100]
GUNASEKARA ET AL.	2016	FA	NaOH + NaSi	AS10112.21, MIP	AASHTO T259	N/A	OD (105°C)	[101]
NUAKLONG ET AL.	2016	FA	NaOH + NaSi	B	Chloride Penetration Depth	N/A	N/A	[102]
GUNASEKARA ET AL.	2017	FA	NaOH + NaSi	N/A	N/A	N/A	N/A	[103]
AL-OTAIBI	2009	S	NaSi	RILEM CPC-11.3	A, ASSHTO T277	N/A	N/A	[104]
LIM ET AL.	2012	S	NaOH	N/A	Ponding Test	N/A	N/A	[105]
CHI ET AL.	2012	S	NaOH + NaSi	N/A	A	N/A	N/A	[106]
LAW ET AL.	2012	S	NaOH + NaSi	N/A	A, AASHTO T277	N/A	N/A	[107]
RAVIKUMAR ET AL.	2013	S	NaOH + NaSi	MIP	A, NT Build 492	N/A	N/A	[108]
MA ET AL.	2015	S	NaOH + NaSi	N/A	NT Build 442, NT Build 492	N/A	N/A	[109]
BALCIKANLI ET AL.	2016	S	NaOH + NaSi	N/A	A	N/A	N/A	[110]
PARTHIBAN ET AL.	2017	S	NaOH + NaSi	B	AASHTO T259 & T260	N/A	N/A	[111]
BEHFARNIA ET AL.	2017	S	NaOH + NaSi	B, BS 1881:	A, G	N/A	N/A	[112]
BONDAR ET AL.	2012	CC, UC	KOH + NaSi	N/A	A, F	N/A	N/A	[113]
BERNAL ET AL.	2012	Binary (S+MK), S	NaOH + NaSi	B	A, In-house diffusivity	N/A	OD (100°C)	[114]
ISMAIL ET AL.	2013	Binary (S+FA), S	NaSi	B	E, D, G, NT Build 492	N/A	OD (100°C)	[95]
BERNAL ET AL.	2015	Binary (S+MK), S	NaOH + NaSi	B	N/A	N/A	N/A	[115]
ALBITAR ET AL.	2017	Binary (S+FA), FA	NaOH + NaSi	B	Ponding Test	N/A	OD (110°C)	[116]
TENNAKOON ET AL.	2017	Binary (S+FA)	NaSi	N/A	A, NT Build 443	N/A	N/A	[117]
BABAEE ET AL.	2016	Ternary	NaOH + NaSi	N/A	Ponding Test	N/A	N/A	[118]
NOUSHINI ET AL.	2016	Ternary	NaOH + NaSi	B	AASHTO TP-95	N/A	OD (100°C)	[119]

[1]S = Slag; MK = Metakaolin; CC = Calcined Clay; UC = Uncalcined Clay; [2]A = ASTM C1202; B = ASTM C642; C = ASTM C1585; D = ASTM C1152; E = ASMT C1218; F = ASTM C1156; G = ASTM C1543; H = ASTM C1556; [3]OD = Oven Drying; μCT = X-ray Computed Microtomography; BET = Brunauer–Emmett–Teller Adsorption; MIP = Mercury Intrusion Porosimetry; SEM = Scanning Electron Microscopy[†] = qualitative description of porosity.

3.0 Factors Affecting Chloride Transport in AACs

In AAC concrete, chloride transport is influenced by (1) the type of precursor and its physical and chemical properties (i.e., crystallinity, fineness, chemical composition), (2) the chemistry of the alkali activating solution, and (3) curing regime [99]. The effect of these factors on properties that affect chloride transport is discussed in more detail in the following sections.

3.1 Precursors

The aim of this section is to briefly review AAC precursors utilized in the surveyed literature, address their variable chemical composition, and discuss how their physicochemical properties and reaction products influence chloride transport. The most common AAC precursors include (1) fly ash (FA), (2) ground granulated blast furnace slag (slag), and both (3) calcined (e.g., metakaolin) and (4) uncalcined aluminosilicate clays (e.g., kaolinite). The average chemical composition of each AAC precursor, based on the values reported in surveyed literature, is shown in **Figure 5**. The data were obtained by aggregating published precursor oxide analysis data from 66 studies concerning chloride transport in AAC pastes, mortars, and concrete. This compositional data will be used to explain some of the variability in bulk properties observed in the literature.

3.1.1 Physicochemical characteristics

In AACs, chloride transport is affected by the physicochemical properties of aluminosilicate precursors. More specifically, physical properties, such as crystallinity and fineness, limit the degree of reactivity. Increasing precursor fineness and lowering degrees of crystallinity accelerate the dissolution of the precursor, which leads to denser pore networks and improved chloride resistance [120]. Increased particle fineness in FA, for example, has been shown to increase compressive strength of resulting AACs [38], which, in many AAC systems, has been

linked to reduced porosity [81,121]. However, in slag-based AACs, increased fineness often

necessitates higher water demand, which, when coupled with higher reactivity due to a greater

surface area, results in excess hydration water, which has been noted by some researchers to

yield higher porosities and lower strengths [49]. Like single precursor systems, particle fineness

affects the reactivity of blended systems in similar ways [96]. When studying transport in any of

these single or binary precursor systems it is important to assess how the properties of each

precursor will affect the binder structure and, therefore, its bulk material properties.

3.1.1.1 Fly ash

FA is primarily composed of silicon dioxide (SiO_2), aluminum oxide (Al_2O_3), iron oxide

(Fe_2O_3), and varied amounts of calcium oxide (CaO). These oxides are contained in four major

crystalline mineral phases: quartz, mullite, hematite, and magnetite, which can form 10-50% of

the bulk ash, while the reminder is largely comprised of amorphous silicate glass [120,122,123]. FA is

classified according to its chemical composition into two major categories – Class F and Class C

– as specified by ASTM C618. These classifications depend on the chemical composition and do

not address crystallinity. Historically, while the class definition has varied [124,125], current

classification focuses on the combined content of silica, alumina, and iron oxides. To be

considered Class F, FA is required to possess a minimum of 70% by weight of the

aforementioned oxides, while a Class C FA requires a minimum of 50%. However, this

classification takes into account neither the crystalline content of the ash nor the compositional

variation of its glassy phases [120]. Average oxide compositions of FAs used as AAC precursors in

the literature reviewed herein are shown in **Figure 5**. As anticipated, information regarding the

crystallinity of FA is unavailable, given that only seven studies report FA crystallinity

[87,88,101,103,122,126,127]. However, recent studies have identified crystallinity as an important

processing parameter for AACs, and many have begun to report it and, in some cases, investigate

it explicitly. For example, Sweeney et al. conducted durability experiments that focused primarily on the amorphous content of SiO_2 and Al_2O_3 in FA [128].

While the majority of published FA studies reviewed herein focus on low-calcium FA (LCFA), a few studies have begun to investigate high-calcium FA (HCFA), because it is now commonly believed—despite experimental evidence to the contrary—that higher calcium contents lead to improved chloride durability. In **Figure 5** CaO outliers correspond to studies that purposefully investigated HCFA [62,75,98,102]. HCFAs typically contain lower alumina contents and several calcium-containing crystalline phases (e.g., Larnite) [62,75]. Generally, in the studies reviewed herein, HCFA AACs exhibited higher porosities and lower chloride resistance than their LCFA counter parts [62,75,98,102,129–131]. Currently the poor performance of HCFA compared to LCFA AACs in terms of chloride durability remains unexplained. These finding are of note, because, generally, slag and OPC precursors with high calcium contents demonstrate a higher resistance to chloride intrusion [132], suggesting that the mineralogical phase of calcium (i.e., crystalline vs. amorphous) is perhaps more important than the total amount in each precursor.
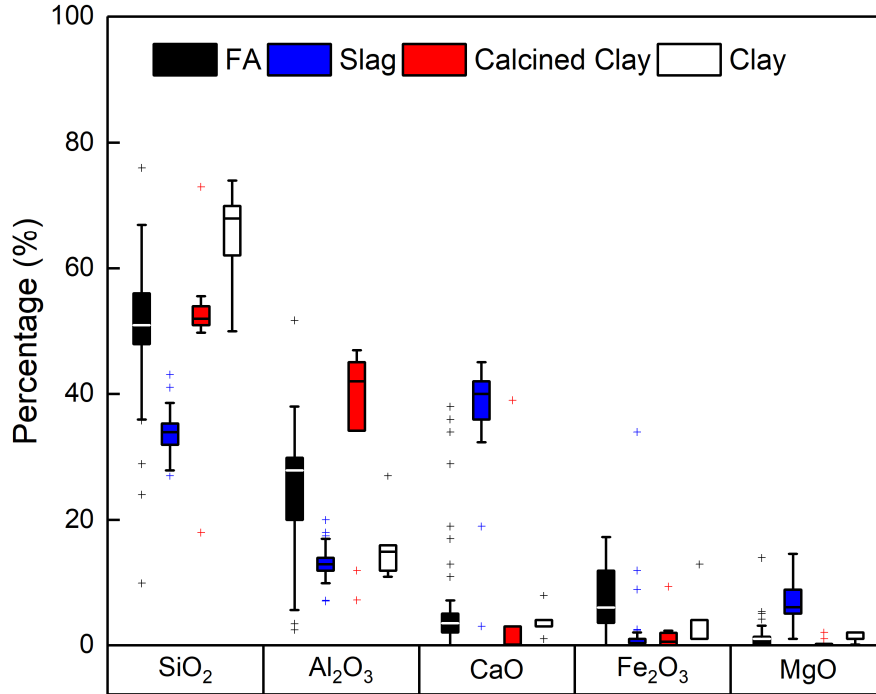
Figure 5: Average chemical composition of all aluminosilicate AAC precursors reported by the studies included in this review. Median data are represented by centerlines in the box plots.

3.1.1.2 Ground-granulated blast furnace slag

Ground granulated blast furnace slag, henceforth referred to as slag, is a highly vitreous, highly reactive, low-chemical-variability byproduct of the steel-making industry and, as asserted by Law et al., the most common material utilized in AAC production [107]. Primarily composed of glassy phases of CaO, SiO_2, Al_2O_3, MgO, and Fe_2O_3, slags usually contain high CaO (30-50%), but not as high as OPC (>50%) [89,107]. Although slags have low chemical variability, major differences between slags lie in their quantities of MgO, as shown in **Figure 5**. Additionally, out of all precursors, slags consistently contain the lowest quantities of both SiO_2 and Al_2O_3. Slag's glassy nature (>90%) imparts increased reactivity compared to FA, and early stage studies of synthetic slags identify a rapid release of glassy Ca^{2+} upon dissolution [133,134].

Slags for use in cement and concrete are currently classified according to ASTM C989 by their performance in a slag reactivity test, where 50/50 mixtures of slag and OPC are graded against an OPC control in terms of its compressive strength. Three reactivity grades of slag are reported: Grade 80, Grade 100, and Grade 120, which indicates slag's potential performance as a supplementary cementitious material (SCM) but is not indicative of its suitability as an AAC precursor. While more applicable classification schemes for slag and other AAC precursors remain to be developed, the current mission of RILEM TC 238-SCM is to define best practices for characterizing the reactivity of SCMs, including slag [135], which will likely also yield better proxy classifications for slag (and other) AAC precursors.

3.1.1.3 Uncalcined and calcined aluminosilicate clays

Naturally occurring, crystalline aluminosilicate clays can be utilized to produce AAC binders either in their raw or calcined form. A variety of natural clays can be subjected to calcination and subsequently used for alkali activation. Natural clays, like kaolinite, contain varying amounts of SiO_2 and Al_2O_3 and can be calcined (i.e., heated to temperatures of 400-1000°C) to achieve dehydroxylation, which induces crystalline-to-amorphous structural changes and, consequently, increases reactivity [136,137]. In general, increased calcination temperature lowers the degree of crystallinity of these clays. In the few studies reviewed herein, metakaolin was the most commonly utilized calcined clay to produce AACs that were subject to chloride durability tests. As a distinctly pure aluminosilicate, metakaolin precursors are high in SiO_2 and Al_2O_3, as evidenced by the calcined clay versus natural clay data shown in **Figure 5**. Bumamis et al. showed that the amounts of reactive silica and alumina in clay precursors were related to improved physical properties of the cement paste, such as density, water absorption, and porosity [138]. However, no definitive conclusion should be drawn about the average chemical composition

of all calcined clays used in alkali activation, given the limited number of published AAC studies concerning calcined clays and chloride transport [84,130,132,139,140] (see **Table 2**).

3.1.1.4 Blended systems

Numerous types of blended precursor systems have been utilized in AAC systems, and those that have been used to study chloride-related performance are included within the scope of this review. Blended systems range from FA/slag and slag/metakaolin binary systems to a variety of other binary and ternary systems that involve rice husk ash or red mud [49,141,142]. Despite these studies, much research is still needed to understand the physical properties and chemistries of combined precursors in blended systems and their impact on microstructural development and resulting material properties [142], especially as they pertain to properties that influence chloride transport. With a burgeoning understanding of heterogenous single precursor systems, it remains a scientific challenge to fully understand and predict structure-property relationships imparted by precursor blends.

A greater understanding of the role of the various glass and crystalline phases in blended precursors need be acquired. Out of the 24 reviewed studies addressing chloride diffusion and binding in binary precursor systems, only five studies attempted to characterize the crystallinity of the mixed precursors, and none discuss the complex dissolution kinetics of the different glass phases of each precursor in the system. As previously discussed, in general, blended slag-containing precursors with high calcium contents have exhibited greater chloride resistance. However, other non-slag high-calcium-containing precursor blends do not perform as well as low-calcium blends in terms chloride penetration than OPC controls [129,143], further substantiating that vitreous calcium phases are preferred to their crystalline counterparts.

3.1.2 Reaction products

The activation of aluminosilicate precursors leads to the creation of a variety of reaction products that depend on precursor chemistry and curing regime. Some of the reaction products observed are binder gels (e.g., C-S-H, C-A-S-H, N-A-S-H), and various authors additionally report finding crystalline phases, including hydrotalcite, zeolites, and other unreacted minerals.

In general C-A-S-H and N-A-S-H, the two main binder gels produced in alkali activation, create distinct microstructural characteristics (e.g., pores) that, in turn, affect chloride transport. In N-A-S-H binders, large macropores are often accompanied by small gel pores that exist within the gel, whereas a more continuous distribution of pore sizes are found in C-A-S-H gels similar to OPC binders. Lloyd et al. and Ma et al. show low-calcium FA-based AACs consist of homogenous N-A-S-H gels occupying much of the sample structure with pores much larger than capillary pores found in OPC [63,144]. Although important for diffusion, gel pores are difficult to investigate due to their small radius and current limitations of porosimetry equipment [61,144]. N-A-S-H binder gels continue densifying the cement matrix due to a process of continued gelation, which reduces pore space over time, temporally affecting chloride diffusivity [101]. Although continued gelation of N-A-S-H binder gels is beneficial, excessive gelation causes depletion of pore solution, which can accelerate steel corrosion in these systems [103]. Leaching of alkalis from the pore solution due to aqueous exposure can inhibit further gelation in N-A-S-H systems as they age [81]. This combination of natural leaching and continued gelation could hamper the long-term durability of N-A-S-H based cements. C-A-S-H and C-S-H gels have significant amounts of bound water, which may reduce the porosity of the system and explain lower water absorption [94]. However, Winnefeld et al. postulated that low-calcium FA-based AACs that produce N-A-S-H gel exhibit lower porosities than high-calcium samples because more binder gel (i.e., C-S-H, C-N-S-H) is formed in the latter [62], further suggesting the importance of calcium and the phase in

which it exists in the precursor. The inclusion of slag, which contains more vitreous calcium phases, into N-A-S-H based systems has been shown to produce both types of binder gels. In these blended systems the "dominant" binder gel controls the diffusion, and some studies indicated that C-A-S-H gels can reduce chloride diffusion in N-A-S-H gel-based systems [95]. Similarly, in other binary systems with a higher weight percent of a precursor that produces N-A-S-H gel, higher overall porosities have been reported [79,114]. However, in a system with FA and metakaolin, increasing the percentage of metakaolin by weight reduced average pore size due to the formation of more N-A-S-H gel [145], which could be attributed to the higher reactivity of metakaolin. Zhang et al. states that binary slag/metakaolin mixtures are chemically stable when immersed in seawater due to the structure of the aluminosilicate gel [76]. Contradictorily, there is evidence that N-A-S-H gels of FA-based systems when immersed in seawater undergo cation exchange between Na and Mg, thereby increasing the porosity of the system [146].

The increased formation of secondary reaction products, such as hydrotalcite and zeolites, is suggested to increase the chloride resistance of AACs. Hydrotalcite formation, for example, has been demonstrated to enhance chloride binding in slag-based AACs [147–149]. Hydrotalcite, due to its structure and large surface area, permits binding of anions. In slag-based AAC mixtures with high contents of MgO activated with NaOH, hydrotalcite-like phases were observed by Ben Haha et al., and it has been further reported that high MgO systems will preferentially form hydrotalcite by reacting Al with Mg until all Mg has been exhausted [69,150–152]. As a consequence, the production of hydrotalcite reduces the availability of Al for the formation of C-A-S-H and N-A-S-H gels [152,153]. Studies on the chloride uptake in hydrotalcite-like phases have yielded positive results, demonstrating the ability of these phases to uptake chlorides in highly alkaline solutions and in slag-based AACs [147,154,155]. Chloride uptake is sensitive to

changes in pH, chloride ion concentration, and strength of the pore solution [156]. One challenge is that, in some pure slag systems, hydrotalcite preferentially reacts with sulfate ions (from the potential decomposition of ettringite) instead of chlorides [157], if ettringite or other calcium sulfate phases are present in the system. Aside from hydrotalcite-like phases, some zeolites have been suggested to exhibit chloride-bearing potential [158]. Zeolites are aluminosilicate minerals (e.g., Faujasite, Mordenite) that occur in nature, and are often found in N-A-S-H based AAC [6,159]. Recent research by Jun et al. posits that alkali-activated FA contains other crystalline zeolite phases (e.g., Chabazite) that may be able to bear chlorides [158]. Gevaudan et al. shows that high silica availability, and high alkali content lead to high degrees of zeolitization [6]. Other authors have shown that mineralization can be induced in N-A-S-H-based systems with the addition of organic compounds and other mineral additives [41,160,161].

3.2 Chemical activators

Activating solutions generally contain (1) silica, often in the form of liquid sodium silicate (NaSi) solution, (2) alkali hydroxides, which not only provide the necessary high pH for activation, but also provide charge-balancing cations (e.g., Na^+, K^+, Ca^{2+}), and (3) water. Common activators include sodium hydroxide (NaOH), potassium hydroxide (KOH), and NaSi solutions. Additionally, calcium hydroxide $(Ca(OH)_2)$ [72], solid silicates (e.g., sodium metasilicate pentahydrate), and sodium-carbonate have also been used for activating aluminosilicate precursors.

Silica content, silica speciation, the choice of alkali metal, and their respective concentrations in alkali-activating solutions directly affects dissolution, precipitation, and, hence, the subsequent gelation and formation of different aluminosilicate binder gels. However, explicit mechanisms for how these activators influence hardened state properties, including chloride transport, needs further refinement [162]. For example, reactions with sodium carbonate as

activators are generally less reactive due to the acidic nature of the carbonate anion compared to reactions with hydroxides [163]. In addition, different metal cations (i.e., Na^+, K^+, Ca^{2+}) present in activating solutions have been noted to influence porosity and degree of dissolution [164,165]. Furthermore, the initial content and phase of the activator (liquid or solid) affects the microstructural development of AACs and properties that affect chloride transport [6,108,166]. Each of these factors are discussed in the following sections.

3.2.1 Silica content

Silica content has been defined in the literature as the amount of total silica in either the activating solution alone or the entire AAC system. The total quantity of silica in an AAC system is expressed as either the Si/Al or SiO_2/Al_2O_3 molar ratios. Oftentimes, however, the quantity of silica in the precursor is assumed to be a fixed amount and, thus, only the additional silica is reported as the silica modulus (Ms), or the ratio of SiO_2:Na_2O, in the activating solution.

Increasing available silica in activating solutions has been shown to lead to reduced pore sizes, regardless of precursor chemistry and, often, reduced porosity. In FA-based systems, for example, additional silica promotes the development of finer pore networks, reduced porosity, and, thus, reduced water permeability (generally Si:Al $\geq$ 1.50) [63,86]. Similar trends have been reported for slag-based systems [89]. Ye et al. [71] and Melo et al. [67] showed that higher silica content reduces porosity and results in a pore network with a smaller average pore size in slag-based AACs (in contrast, slags without added silica lead to unrefined pore systems [68,71]). Likewise, for metakaolin-based systems, Duxson et al. showed that Si/Al ratios less than 1.4 lead to higher-porosity systems [73], where many pores are interconnected, while Si/Al ratios greater than 1.65 result in smaller pores distributed in a more homogenous pore system.

In fact, data show that increased silica content, in general, correlates with reduced chloride diffusivity in AACs, regardless of precursor. Increasing the Ms in FA-based AACs, for

example, resulted in comparable chloride resistances of OPC and blended cements. However, the initial pH of these systems was insufficient to passivate the steel reinforcement or maintain a constant diffusion coefficient in the long term [100], demonstrating a durability tradeoff between a dense microstructure and passivation ability. In contrast, slag-based AAC systems with increased Ms have exhibited lower rapid chloride penetration test (RCPT) values and permeability values compared to OPC and improved non-steady-state diffusion behavior [104,109,167]. In binary FA-slag and bagasse ash-china clay systems, increased available silica content played a role in reducing chloride intrusion [75,82], further substantiating the important role of silica-containing activators. However, in studies on slag-based AACs, a Ms of 1.25 increased sorptivity due to the evolution of microcracks that can occur [89,107], which are well known to exacerbate chloride diffusion [168].

Experimental evidence suggests that the form in which silica is added (e.g., anhydrous sodium metasilicate, sodium silicate, colloidal silica, soda glass) will influence AAC reaction kinetics, microstructural development, and, consequently, its transport properties. Behfarnia et al. incorporated both micro- and nanosilica into slag-based systems in identical percentages and observed higher chloride resistance with the addition of microsilica only [112]. In a metakaolin-based system, Gevaudan et al. studied the influence of silica by adding either solid soda glass or a liquid (NaSi). The availability of silica from liquid NaSi enabled expeditious gel formation and reduced porosity in systems with the same SiO_2:Na_2O ratio compared to the solid silica-containing samples [6]. Ravikumar et al. utilized a solid and liquid form of NaSi, which led to a variety of different, inconclusive performances of slag-based cements in terms of chloride diffusion [108]. While the use of liquid NaSi reduced overall porosity, the mixture activated with anhydrous NaSi exhibited improved chloride resistance, which the authors attributed to changes in pore structure, pore solution chemistry, and resulting ionic conductivity [108]. Although the

effects of silica speciation are known to affect reaction kinetics [169], understanding the relationship between silica chemistry and durability remains a fundamental challenge for the field.

3.2.2 Alkali content

Expressed in different forms throughout the literature, alkali content, in general, refers to the quantity of elemental alkali metals (i.e., Na^+, K^+, Ca^{2+}) in the activator. Alkali content has been defined as the molarity of the solution (i.e., 4M NaOH), the percentage of metal oxide by weight of precursor (i.e., Na_2O per g of binder), or, in the case of liquid NaSi, the Ms of the solution (i.e., Ms=2.0).

Experimental evidence substantiates that higher alkali content (generally Na:Al≥0.75) promotes rapid dissolution of precursors and, hence, reduces chloride transport in all precursor systems due to a reduction in porosity. Higher alkali contents in both FA- and slag-based AACs have reduced porosities and reduced pore sizes, as indicated by lower water permeability and sorptivity of the samples [63,102108]. However, when alkali content is held constant, porosity and average pore sizes are variably affected by the type of alkali metal cations, regardless of precursor [59,90,162]. The observed lower porosities can be attributed to higher alkali content promoting a more rapid dissolution of the precursor [6,39,139,169,170]. The increase in chloride resistance due to reductions in total pore volume and pore sizes observed with a higher alkali content has also been observed (and discussed previously) with increases in silica content. Moreover, in FA-based systems, higher alkali content decreased the chloride diffusion coefficient, as expected, and affected the quantity of both free and bound chlorides in the cementitious matrix [99]. In slag-based AACs, increasing alkali concentration and holding the other factors constant (i.e., Ms, curing time), resulted in significant reductions to RCPT values were observed [110]. Reductions in RCPT values have been correlated with observed reductions in the

coefficient of non-steady-state diffusion with increasing alkali content [109]. Lastly in MK systems, higher alkali content – more than silica content – influenced the development of zeolitic crystalline phases that reduced overall porosity [6].

Alkalis from precursors and activators change the pore solution chemistry, which affects chloride intrusion and the ability of AACs to passivate steel. FA-based mixtures can provide adequate passivation to reinforcing steel, according to Bastidas et al. [171] and Criado et al. [86]. However, passivation has been shown to depend on the type of activator, the dosage, and the alkalinity of the solution such as utilizing a liquid NaSi and NaOH solution versus a solid NaSi and sodium carbonate activator due to the changes in the overall pH of the pore solution [132,170,172–174]. These findings are also applicable to slag-based (and some blended) mixtures, where high metal cation concentrations in the pore solution indicate the slag's ability to passivate steel [65,104]. For example, FA and slag mixtures with a higher volume of pores than a comparable OPC mixture exhibited lower susceptibilities to chloride ingress, which was attributed by the authors to repulsive ionic interactions between chlorides and pore solution chemistry [95].

3.2.3 Water content
Water content in OPC and AAC systems typically refers to the ratio of water to cementitious binder. However, depending on the system, whether it be paste, mortar, or concrete, water content can also be presented as the ratio of total liquid to total solids (L:S) used in the mixture.

Lower water-to-binder ratios reduce overall porosity in all AACs; however, experimental evidence also suggests that lower water-to-binder ratios reduce average pore sizes in slag-based AACs. In FA-based systems, decreased water contents have been correlated with lowered porosities [78,171], with the caveat that lowering water content increases binder viscosity, which can lead to air entrapment in the mixture [61]. In terms of average pore size, while both Zhu et al. [78] and Bastidas et al. [171] note no significant differences when decreasing water content, Skvára et al.

33

[61] reports a decrease in average pore size with decreasing water content. Related studies have

suggested that insufficient water may lead to lower reactivity [175]. In slag-based AACs, water

content imparted similar effects on porosity compared to FA; however, water content might have

a greater role in altering pore size [176]. Lower-water systems have been proven to exhibit

improved chloride resistance and decreased water and chloride permeability [75,78]. Changes in

average pore size is observed in binary FA/slag mixtures and in mixtures containing

slag/metakaolin [78]. In all binary cases, the higher the slag content, the more evident the effect

water content has on reduced porosity and average pore size [76].

3.3 Curing regimes

Heat curing in AACs is well known to lead to increased reactivity, reduced porosities,

and reduced average pore sizes. Microstructural differences develop due to changes in the

kinetics of the reaction. Higher temperatures promote increased precursor dissolution and affect

the overall generation of reaction products [39,169,170]. Higher curing temperatures, in general,

reduce porosity, sorptivity, and chloride penetration in AACs regardless of precursor. In alkali-

activated FA, water permeability was reduced with longer periods of heat curing [63]. Curing at

temperatures higher than 60°C and lower than 75°C decreased the volume of permeable pores

and decreased sorptivity, which is used in the literature as an indicator of higher tortuosity [63,119].

Heat curing has also decreased permeability in some natural clay-based AACs, which was

attributed by the authors to initial existence of water (due to polycondensation) that enhanced

crosslinking and induced subsequent blockage of pores, which led to reduced chloride ion

penetration [113].

Exploratory studies have elucidated that, unlike temperature, other curing conditions

(e.g., time, humidity) may impart differences to each individual precursor/activator combination,

but these variables have largely remained unexplored in the surveyed literature. Humidity

conditions, for example, change the water availability in the cement matrix and play a role in the kinetics and degree of reaction. Interestingly, a FA activated with NaOH exhibited reduced porosities when dry-cured as opposed to steam- or wet-cured [60], while FA-based binary systems cured in a submerged saline environment (full saturation) exhibited lower sorptivity and decreased chloride penetration, which was attributed to reduced leaching of pore solution during activation [177]. Additionally, the intrusion of salt into the matrix was found to be negligible [177]. Slag systems cured in high temperature and relative humidity above 80% performed better than air- and limewater-cured slag-based AACs [106]. Autoclaved slag cements (with no added silica and low Na_2O dosages) produced under high pressure, high heat, and high relative humidity conditions exhibited low porosity. This reduction has been attributed to the increased reaction of slag particles during curing [92]. Therefore, while high humidity is generally beneficial, for some systems, high humidity may prove suboptimal in achieving desirable microstructures.

In the reviewed literature, while blended precursor systems (e.g., slag/FA) are generally cured between 20-30°C, these curing regimes do not take into account the lower rate of dissolution of FA at those temperatures or the different humidities at which they must be cured. For example, FA is optimally cured at temperatures >60°C with [39] showing isothermal conduction calorimetry data that points to the low reactivity of FA when cured at temperatures lower than 30°C. [15] showed that FA activated with NaOH should be dry-cured. AAC chloride transport literature has yet to address the interactions of curing regimes with the physicochemical characteristics of blended precursors and the impact those interactions have on chloride diffusion and chloride binding.

4.0 Descriptive Statistics of Porosity and Chloride Diffusion

This section statistically describes data from the reviewed literature in order to (1) analyze the most studied experimental parameters, (2) discuss the variability of those parameters, and (3) elucidate porosity and chloride diffusion differences by AAC precursor. Variability of chloride diffusion measurements is supplemented with discussions on the limitations of current characterization methods.

4.1 Experimental Parameter Mapping

Figure 6 quantitatively summarizes the ranges of common experimental parameters explored in the reviewed literature through a codified scale (from 0 to 1). The scales correspond to actual magnitudes that vary for each parameter (see **Table 3**). For example, the most studied L:S ratio in pastes lies between codified values of 0.3 and 0.4, as shown in **Figure 6**. Based on **Table 3,** these codified values correspond to L:S ratios between 0.17 and 0.24. **Figure 6** illustrates that marked differences exist in the ranges of experimental parameters (Si:Al ratio, Na:Al ratio, curing temperature) that have been explored for different material systems (i.e., paste, mortar, concrete), which need be reconciled for appropriate comparisons between those systems. The data presented in **Figure 6**, in addition to aiding explanation of reported material properties related to chloride transport (see **Section 4.2**), may serve as a useful research tool for further experimentation of theoretical and practical studies on the chloride diffusion of AAC paste, mortar, and concrete.

In the literature, paste and mortar studies have a wider range of Si:Al and Na:Al ratios, while Ca:Al and L:S ratios remain largely unvaried in all three systems. Pastes generally explore these wider ranges of Na:Al and Si:Al ratios to understand microstructural development. However, the majority of Ca^{2+} comes from the usage of slag, given that Ca^{2+} that is rarely

supplemented in these systems. Across all parameters in the reviewed studies, AAC pastes have been investigated with large ranges when compared to AAC mortar and AAC concrete. For example, Na:Al ratios for paste (0.0-1.0) have a larger range than mortars and concrete, 0.4-0.6 and 0.5-1.2, respectively. In AAC concretes Si:Al and Na:Al ratios have been explored at wider ranges than paste and mortars in the reported literature. For example, AAC paste samples explore Si:Al and Na:Al ratios at ranges of 1.1-2.0 and 0.0-1.0, respectively, and AAC concrete are mostly studied at Si:Al and Na:Al ratios of 1.9-2.7 and 0.5-1.2, respectively. Contrastingly, minimal differences exist between Ca:Al and L:S ratios explored in the different material systems, which is due to the fact that the primary source of calcium in all studies is from fairly similar slags. The aforementioned ratios tend to be explored in the following ranges: 0.0-0.5 (Ca:Al ratio) and 0.4-0.6 (L:S). Although **Figure 6** provides useful information in terms of what parameters have been studied, the literature does not provide quantities of reactive silica, alumina, and calcium in their material systems, which means for more highly crystalline precursor systems, these values may be different than those reported [128].
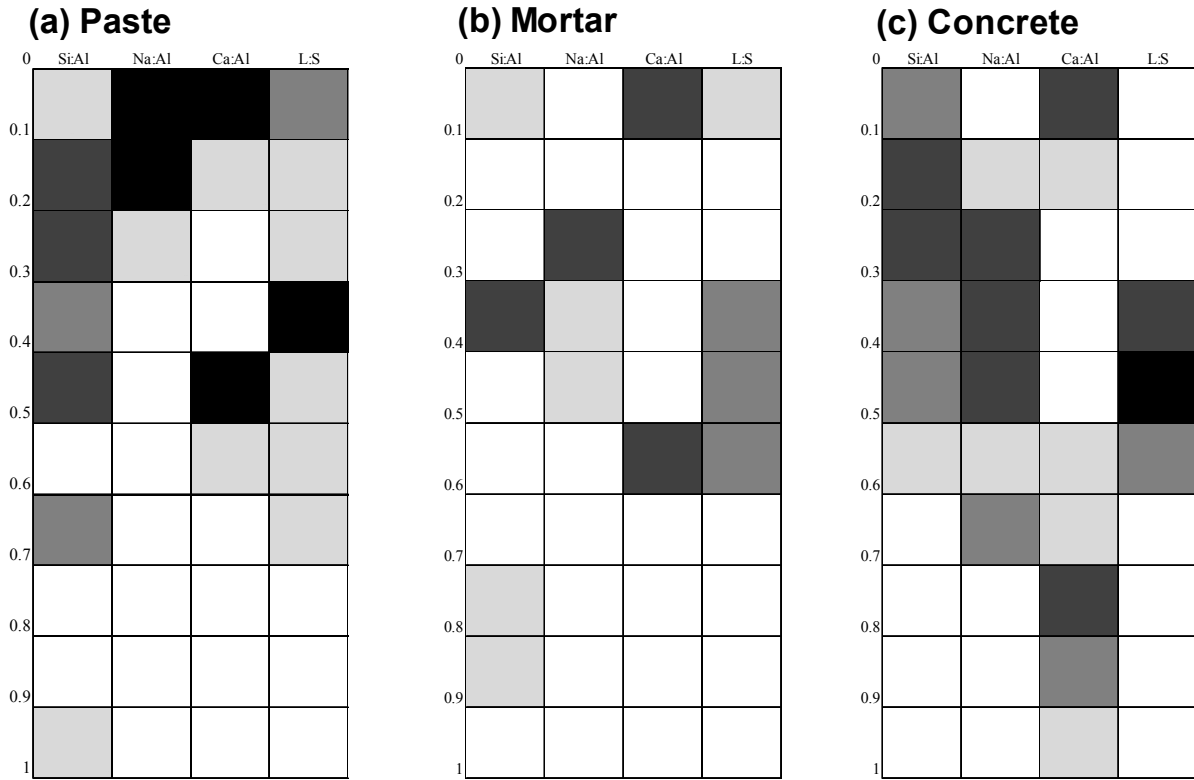
Figure 6: Experimental frequency of important parameters in porosity and chloride diffusion studies of different AAC material systems. Experimental frequency is categorized with distinct color ranges symbolizing: ■ ≥ 60 studies, ■ ≥ 30 studies, ■ ≥ 20 studies, □ ≥ 10 studies, □ < 10 studies. Ranges for the codified scale (0-1), which vary for each material system, are listed in **Table 2**.

Table 3: Range of codified values and parameter values explored in Figure 2. Paste outliers are the following: Si:Al > 5 (7), Na:Al > 5 (1), Ca:Al > 6 (6). Mortar outliers are the following: Si:Al > 5 (0), Na:Al > 5 (1), Ca:Al > 6 (1), L:S > 1 (3).

Codified Values	Paste				Mortar				Concrete			
	Si:Al	Na:Al	Ca:Al	L:S	Si:Al	Na:Al	Ca:Al	L:S	Si:Al	Na:Al	Ca:Al	L:S
Δ	0.43	0.50	0.60	0.065	0.35	0.18	0.49	0.06	0.40	0.24	0.34	0.07
0	0.69	0.00	0.00	0.15	0.39	0.04	0.0	0.21	1.54	0.01	0.01	0.18
1	5.00	5.00	6.00	0.80	3.84	1.85	4.88	0.80	5.51	2.40	3.45	0.88

Figure 7 presents the distributions of the experimental parameters reported in the

literature. The L:S ratio remains relatively unchanged between systems as evidenced by the small

variation in the mean. However, means of experimental parameters for Si:Al ratio, Na:Al ratio, and maximum curing temperature vary widely between material systems. The means of Si:Al ratios increase from paste (2.46) to concrete (2.73) systems, but decreases for AAC mortars (2.11). A similar trend is observed in the means of Na:Al ratios in paste (0.69) and concrete (0.95) mixtures with a decrease in AAC mortars (0.73). Finally, the means of maximum curing temperature vary from 37.4 °C to 75.2 °C to 47.6 °C for paste, mortar, and concrete, respectively. Contrastingly, the means of L:S ratios for paste, mortar, and concrete—0.39, 0.50, 0.49, respectively—remain relatively unchanged. In addition, AAC concretes exhibit the least variation in Si:Al ratio, Na:Al ratio, L:S ratio, and maximum curing temperature when compared to AAC pastes and mortars (see **Figure 7**), while AAC mortars exhibit the largest variations in Na:Al ratios, L:S ratios, and maximum curing temperature. Curing regimes are chosen in a seemingly arbitrary manner. Reported here are the maximum curing temperatures, but each individual mixture often uses a different set of temperatures with varying durations and humidities.
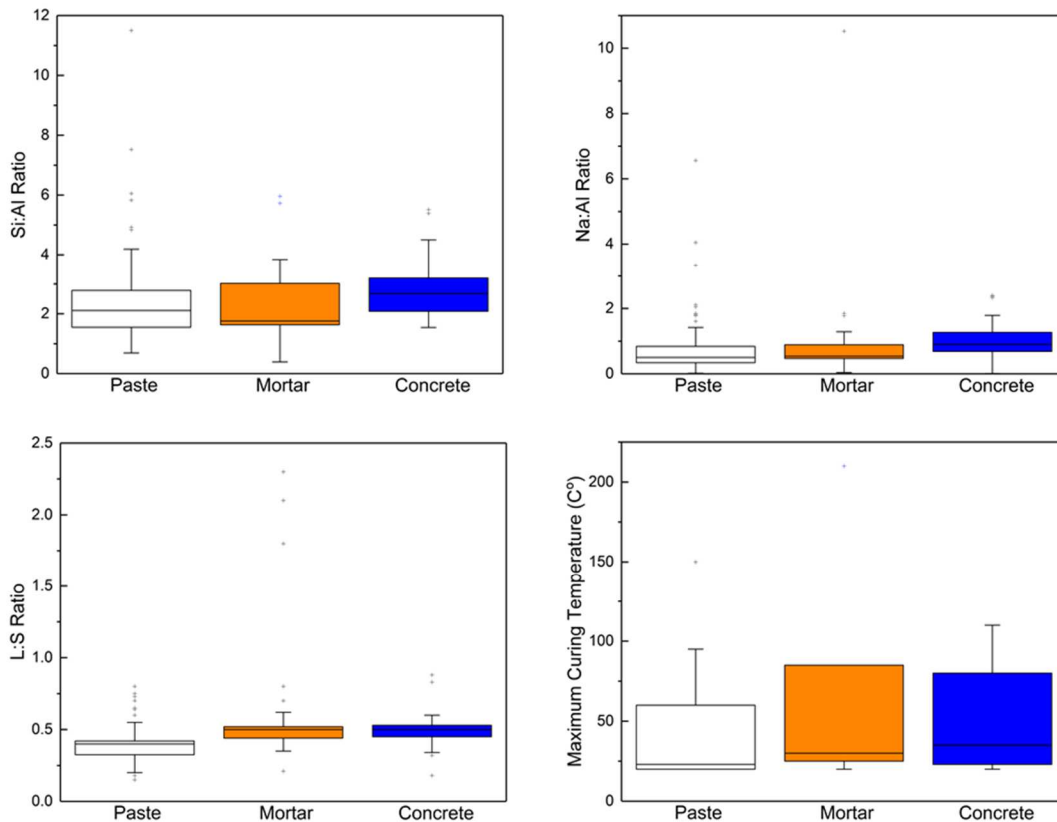
Figure 7: Investigated experimental parameters across AAC material systems (i.e., paste, mortar, and concrete) regardless of AAC precursor. Median data are represented by centerlines in the box plots.

4.2 Porosity of AAC pastes by precursor

Figure 8 shows the average reported porosities of AAC pastes by aluminosilicate precursor. Depending on precursor, AAC pastes have comparable or lower porosities when compared to OPC pastes. From the reviewed literature, the average porosity of AAC pastes is 26.7%. In contrast, OPC paste studies (sans SCMs) report higher porosities of 30%-34% [7,178,179]. In some cases when different precursors are used, AAC porosities are reported to be higher than OPC. For example, average porosities of natural clay-based AACs (36.2%) are higher than OPC (see **Figure 8**), which is expected, due to the higher crystallinity and lower reactivity of natural

clays. As a result, it is evident that, while porosities for AACs depend on the precursor, many have achieved comparable or lower porosities than OPC.

Statistical analysis of paste porosity data from the reviewed studies elucidate that increased exploration of experimental factors in AAC pastes yield high variability of porosities in the most oft-studied precursors (i.e., FA, slag, binary blends), as seen in **Figure 8**. FA, slag, and binary mixtures comprise approximately 85% of all AAC pastes in the surveyed literature, and the effects of different processing factors (and ranges of those factors) have been more thoroughly studied in these precursors than in less common precursors, like calcined and uncalcined clays, resulting in a wider range of paste porosity data reported in the literature (see **Section 4.1**). Interestingly, slag has been reported to have among the lowest chemical variability of any other precursor (**Figure 5**), yet slag-based AAC pastes exhibit the largest variation in reported paste porosity (**Figure 8**). This variability in achievable paste porosities is likely due to the wide range of activation solution chemistries and processing conditions employed in the surveyed literature, emphasizing further need for a more critical and holistic understanding of the role that relevant factors, like activation solution chemistry and precursor reactivity, have on AAC paste porosity.
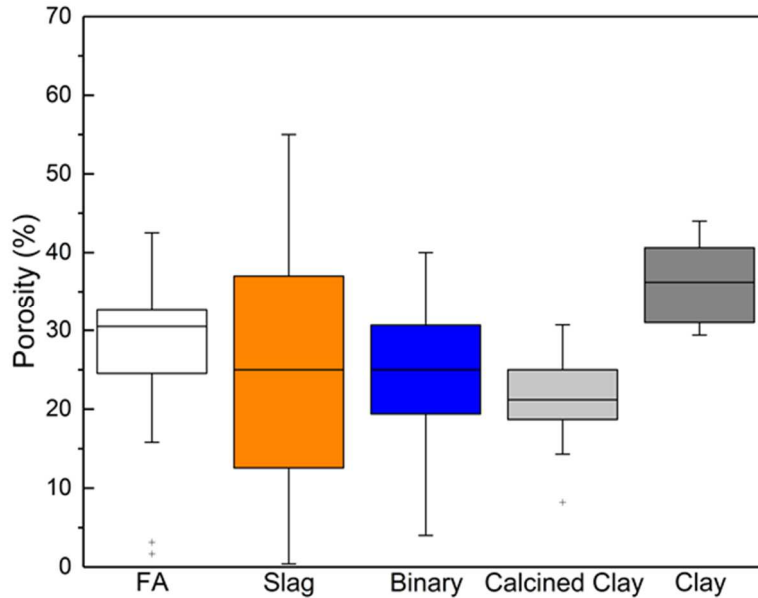
Figure 8: AAC paste porosity by precursor. Outliers: FA (3.13%, 1.67%) and calcined clay (8.2%). Median data are represented by centerlines in the box plots.

Descriptive statistics of the paste porosity data shown in **Figure 8** are summarized in

Table 4. The statistical distribution of paste porosity data was evaluated using the Anderson-

Darling (AD) goodness-of-fit statistical test for normality. The AD statistical test was modified

to identify other possible distributions (*i.e.*, exponential, Weibull, gamma, lognormal). Results

show that the porosities of AACs made with binary blends, calcined clays, or clays can be

described well using normal distributions. The normal distribution of the data may be due to the

low sample number (clay and calcined clay groups) or the decreased factor effect affecting

porosity (binary), but further research is needed to make more definitive conclusions. AD

statistical test results were inconclusive for determining the distribution of the reviewed porosity

data for both FA- and slag-based AAC paste. Such a result may be due to the porosity variability

arising from the effects of different processing factors (and ranges of those factors) in these

highly studied precursors (see **Section 4.1**).

Table 4: Descriptive statistics for AAC paste porosity by precursor.

Factor	N	Mean (%)	95% Confidence Interval (%)	Anderson-Darling Test (p-value)	Statistical Distribution*	Games-Howell Grouping
FA	48	28.04 ± 7.71	(25.80, 30.28)	1.57 (< 0.005)	N/A	A
Slag	68	24.27 ± 15.0	(20.63, 27.91)	0.92 (0.018)	N/A	A B
Binary	31	23.90 ± 9.19	(20.53, 27.27)	0.52 (0.171)	Normal	A B
Calcined Clay	11	21.16 ± 6.32	(16.92, 25.41)	0.35 (0.393)	Normal	B
Clay	15	36.18 ± 4.96	(33.43, 38.93)	0.33 (0.463)	Normal	C

Histograms included in supplementary information.

Significant mean porosity differences exist between clay-, calcined clay-, and FA-based AACs, while slag and binary mixtures exhibit similar mean porosities (**Figure 8**). In order to differentiate between mean porosities of precursors through an analysis of variance (ANOVA), the Levene statistical test was performed, which concluded that the porosity data have unequal variances between precursors (p-value < 0.01). As a result, the Welch statistical test was used to analyze mean differences. The normality assumption in this statistical test was not met by the porosity data of both FA and slag precursors, but it was deemed excusable due to robustness of the t-test statistic as evaluated by [180]. Results, shown in **Table 4**, demonstrate that natural clay-, calcined clay-, and FA-based AACs have distinct mean porosities than other AAC precursors. As expected, the mean porosity of natural clay-based AACs were highest of any other precursor, given the lower chemical reactivity of natural clay compared to other aluminosilicate precursors.

4.3 Chloride diffusion of AAC concrete by precursor

Figure 9 shows the average reported porosities of AAC pastes by aluminosilicate precursor. Generally, FA and slag-based (binary) AAC concrete materials have superior chloride diffusion coefficients when compared to OPC concrete. The chloride diffusion of OPC concrete is reported to be between 1E-11 and 1E-12 m^2/s without use of SCMs [95,117,181]. In contrast, similarly to AAC porosities, chloride diffusion coefficients largely vary by precursor. For example, clay-based AAC concrete has the most unfavorable chloride-diffusion coefficient, which is again expected, as clay-based AAC pastes possess the highest porosities amongst all pastes due to the lower reactivity of clays (**Figure 7**).

Statistical data of chloride diffusion coefficients of AAC concrete reported in the reviewed literature shown in **Figure 9** are summarized in **Table 5**. In contrast to the paste porosity data presented in **Section 4.2**, slag-based AAC concretes have exhibited lower variability than fly-ash based AAC concretes in terms of chloride diffusion coefficient (**Figure 9**). As seen in **Table 5**, chloride diffusion coefficients of slag- and clay-based AAC concrete were found to be described well using a normal distribution, while diffusion coefficients of binary blends were described well using a Weibull distribution. As previously performed for AAC paste porosity data (**Table 4**), the statistical distribution of chloride diffusion coefficients was determined using the Anderson-Darling (AD) statistical test for normality. The AD statistical test was modified to identify other possible distributions, yet results were inconclusive for the chloride diffusion data of FA-based AACs. No data yes exist on the chloride diffusion of calcined clay (*i.e.*, metakaolin) AAC concrete.
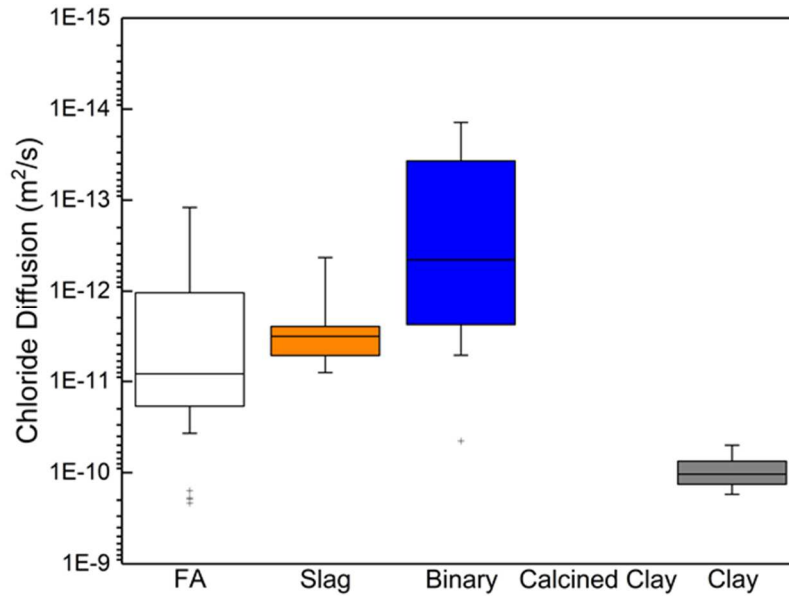
Figure 9: AAC concrete chloride diffusion coefficient by precursor. No data available on calcined clay-based AAC concrete. Median data are represented by centerlines in the box plots.

Table 5: Descriptive statistics for AAC concrete chloride diffusion coefficient by precursor.

Factor	N	Mean (m²/s)	95% Confidence Interval	Anderson-Darling Test (P-value)	Statistical Distribution*	Games-Howell Grouping
FA	43	2.63E-11 ± 5.42E-11	(9.6E-12, 4.3E-11)	9.11 (< 0.005)	N/A	A
Slag	33	3.73E-12 ± 1.98E-12	(3.0E-12, 4.4E-12)	0.46 (0.247)	Normal	B
Binary	10	5.46E-12 ± 1.4E-11	(0, 1.5E-11)	2.57 (<0.005)	Weibull	A B
Calcined Clay	0	N/A	N/A	N/A	N/A	N/A
Clay	10	1.06E-10 ± 4.18E-11	(7.6E-11, 1.4E-10)	0.27 (0.602)	Normal	C

Histograms included in supplementary information.

As seen in **Table 5**, all precursors exhibit uniquely different means in chloride diffusion coefficient, with binary blends having similar chloride diffusion coefficients to both fly ash- and slag-based AACs. Similar to the statistical analysis of porosity data (**Table 4**), the Levene test was used to test the null hypothesis of equal variances, which was rejected and the alternative hypothesis was accepted (p-value < 0.01). As determined by the Games-Howell means difference comparison, seen in **Table 5,** all AAC precursors had statistically different mean

45

chloride diffusion coefficients with the exception of binary blends, which had a statistically similar means to both slag- and FA-based AAC concrete. As was the case in the previous analysis of porosity, the normality assumption in these statistical tests was not met by the chloride diffusion coefficient data for both FA and binary blend concrete, but it was deemed excusable due to robustness of the t-test statistic, as evaluated by [180]. Results shown in **Table 4** and **Table 5** demonstrate that natural clay-based AACs have the highest mean paste porosity and chloride diffusion of any other AAC precursors. Again, this result is to be expected, given the lower amorphous contents and, thus, lower reactivity of uncalcined clays versus calcined clays and other industrial aluminosilicate precursors, like FA and slag.

5.0 Challenges and Opportunities in the Study of Chloride Intrusion in AACs

Despite advances in experimental studies that investigate chloride transport in AAC materials, a number of challenges and development opportunities exist to further scientific understanding of chloride transport in AACs and to fully elucidate similarities and differences between the chloride resistances of AAC and OPC paste, mortar, and concrete. For example, current test methodologies that are employed to study the chloride transport properties of AAC paste, mortar, and concrete are based on tests that were previously developed for OPC-based binders and do not account for the differences in the chemistry of AAC binders. New methods and advanced characterization techniques, like X-ray micro-computed tomography, provide opportunities for more accurate measures of transport-relevant properties. Together, these improved methods and tools will likely lead to new materials science approaches to minimize chloride transport, such as enhancing chloride binding in AAC binders. The following sections discuss these challenges and potential opportunities in more detail.

5.1 Addressing limitations of chloride diffusion test methods

While the strengths of chloride diffusion test methods lie in their ability to quantify relative increases or decreases in chloride penetration resistance, inherent limitations in physical, chemical, and electrical resistivity methods used to characterize chloride ingress can obfuscate and impart inaccuracies on the response by affecting factors (e.g., preconditioning, instrumentation, test duration, aggregate volume content, saturation degree, quantification, precursor and pore solution chemistry) that are important for determining actual chloride transport. For example, given that chloride transport is governed by three distinct mechanism, which all can contribute to chloride transport phenomena, each test either isolates one mechanism or confounds multiple mechanisms into one measurement. Additional limitations of each type of characterization method are discussed in this section.

For physical characterization methods, the primary limitation concerns preconditioning regimes for C-A-S-H and N-A-S-H gel systems. Ismael et al. showed that preconditioning procedures associated with test methodologies in OPC concrete for porosity, water absorption, and permeability impart structural and chemical changes to AACs [182]. Therefore, the authors of [182] suggest that the selection of preconditioning methods should depend on the amount of bound water in the cement in an attempt to preserve the integrity of the binder gels. C-A-S-H gels tend to chemically bind water, while N-A-S-H gels physically bind water, so the removal of water via vacuum or oven drying from C-A-S-H gels leads to the potential for more structural damage. The authors recommend that C-A-S-H gel-based binders be preconditioned through a solvent exchange process utilizing acetone without the use of heat or vacuum, while, for N-A-S-H gels, vacuum drying paired with acetone for solvent exchange should be the primary preconditioning regime. In the same study, a 50/50 blend of LCFA and Slag cement showed no chemical changes

upon oven dried, but some pore collapse was still noted, thereby suggesting that appropriate preconditioning regimes blended systems remain a significant challenge.

Chemical characterization methods often provide the most direct measurements of chloride diffusion; however, they are limited by the following factors. Ponding tests are typically conducted over a minimum of 90 days, and the chemical extraction processes are time-consuming. In addition, Yang et al. noted difficulty with precise differentiation between free and bound chlorides in AACs [80]. The effect of volume and type of aggregates in distorting diffusion coefficients adds to the difficulty of interpreting chemical characterization results [87,111,183]. Furthermore, while ASTM C642 has been the primary method of saturating specimens in the literature to attempt steady state diffusion, saturation is not always easily achieved [184]. For OPC concrete samples, Bu et al. [185] suggests vacuum-saturating specimens over a period of 24 hours to ensure full concrete saturation. However, while this practice is not necessarily best for all AACs, as some are prone to microcracking (as noted above) and pore solution leaching, it provides a more accurate methodology for those AAC-based binders that can resist vacuum saturation. A potential methodological solution would consist of extracting AAC pore solution and creating a saturating solution with a near identical composition to minimize leaching.

Electrical characterization methods of chloride diffusion have been explored by many researchers. Bernal et al. [114], Balcikanli et al. [110], Shi et al. [89], and Andrade et al. [186]report that results of RCPT experiments are mainly dependent on pore solution chemistry as opposed to the nature of the pore structure. Noushini et al. verified the last assertion by finding that, while some AAC systems have denser matrices than their OPC counterparts, they exhibit relatively low resistivity values [187]. In addition, Ravikumar et al. reconciled the values of RCPT with those of non-steady state diffusion to understand any potential damage accelerated test methods might

cause to the AAC microstructure due to the high temperatures induced by electrical currents [188].

Resistivity methods for measurement of chloride ions in AACs could be improved by modifying the work on of Weiss et al. [189] on OPC concrete, where pore solution is extracted and its resistivity is measured separately to create a correction factor for the resistivity of the cementitious binder. A methodology like this would aid in accounting for the variable pore solution chemistries of AACs.

In summary, results from physical, chemical, and electrical resistivity tests can vary due to limitations of those characterization methods. Despite these limitations, however, these standard methods of characterization, while developed for OPC concrete mixtures, have been essential to advance the state of knowledge regarding AAC and chloride transport. Further research should use the best practices discussed here protect the microstructural integrity of the materials, and to obtain more realistic results.

5.2 Advanced characterization techniques

Chloride diffusion is a complex mechanism that often necessitates a suite of tests tailored to address challenges of varying length scales and other limitations explained herein. The use of advanced characterization methods, such as non-invasive X-ray micro-computed tomography (μCT), are emerging as part of a new generation of methods being employed by researchers to attempt to fully characterize the microstructure of AAC and to relate microstructural understanding to resulting material properties that influence chloride transport. Provis et al. [190] and Long et al. [83]for example, employed a μCT to observe the development of AAC microstructure over time [77,83]. One advantage of μCT is that it eliminates a need for sample pre-conditioning. Discontinuing harsh pre-conditioning regimes, as Ismail et al. recommend, will enable better understanding between indirect and direct testing [191]. This particular method does face its own challenges, however, in terms of time and data required to obtain fully characterized

AAC pore networks. Additionally, Dehghan et al. [132] showed how to use electron microscopy and µXRF techniques to characterize how chloride ions travel through different high and low calcium binders. These techniques allow for simultaneous quantification of chlorides and chloride diffusion coefficients in the cementitious matrix utilizing a faster and less labor-intensive process than traditional methodologies, while providing maps of chloride intrusion and agglomeration in the sample. Currently these techniques are limited by the quality of available calibration curves and the sensitivity of the equipment [132].

 Such improvements in characterization methods will result in a deepened understanding of the relationship between accelerated testing and *in situ* behavior. Additionally the work of Criado et al. implores future studies to take into account the redox potential of pore solution chemistries, since they will lead to different electrochemical signals [172,192]. This need, expressed by Duxson et al. in 2007, aims to move promising results from preliminary testing to field research, which is essential to substantiate real-world performance [193]. Additionally, due to its industry status as a new cementitious binder, more longitudinal studies need be performed on AACs to (1) understand how each influential factor described herein affects long-term microstructural development and both water and ion transport and (2) substantiate sufficient durability in both mild and aggressive environmental conditions.

5.3 Enhancing chloride binding in AACs

As previously discussed, the work of Ke et al. elucidated the chloride binding potential of hydrotalcite and hydrotalcite-like phases in carbonate-activated slags [147,154–156]. Although this work identifies mineral phases in slag based-AACs that bind chlorides and subsequently delay their transport through the pore network, more experimental work ought to be carried out to determine which phases of AACs, crystalline or amorphous, can bind, bear, or precipitate to reduce chloride diffusion. After identifying phases with exceptional chloride binding capacity,

further experimental work should be dedicated to controlling and manipulating mineralization in AAC pastes to enable the preferential formation of those minerals and ultimately enhance chloride binding potential.

6.0 Conclusion

This review provides a process-structure-property assessment of the factors that impact chloride transport in alkali-activated cement (AAC) paste, mortar, and concrete. The reviewed literature indicates that physicochemical precursor characteristics, such as greater fineness and lower crystallinity, play a crucial role in dissolution, reactivity, and microstructural development of AACs leading to improved durability outcomes. Furthermore, the reviewed literature suggests that simply the presence of calcium alone in a precursor is not an indicator of improved chloride durability, but that the phase of the calcium (i.e., amorphous, semi-crystalline, crystalline) is perhaps a better predictor of increased durability. This behavior is particularly poignant when the durability of HCFA was compared to LCFA and slag AACs, where HCFAs were the worst performers. Understanding and predicting the behavior of blended AACs in terms of chloride durability remains a scientific challenge, because the physicochemical characteristics of amalgamated precursors result in different reaction kinetics and microstructural development.

Additionally, through a meta-analysis of published experimental data, the literature suggests that, in general, higher silica content (Si:Al ratio), higher alkali content (Na:Al ratio), lower water content (L:S ratio) improve chloride resistance. Contrastingly, while higher silica content is generally beneficial, experimental evidence suggests that it can lead to continued gelation in N-A-S-H based AACs, creating a trade-off between beneficial lower porosities but detrimental reductions in pore solution. This continued gelation further suggests that a greater

51

understanding of silica chemistry is necessary to address long-term chloride durability. Finally, as expected, heat curing improves porosity and, consequently, chloride resistance regardless of aluminosilicate precursors.

Evidenced by data from supporting literature, there is a clear need for overcoming limitations of chloride transport characterization methods that were developed for ordinary portland cement (OPC) concrete *via* advanced techniques, like X-ray computed micro-tomography and electron microprobe analysis, to better assess chloride transport in AAC paste, mortar, and concrete. Furthermore, improved mineralogical understanding of chloride binding is essential to advance scientific understanding and, ultimately, to inform the design and engineering of durable alkali-activated materials for applications in chloride-laden environments.

Acknowledgments

CHAPTER 4: Zeolites Faujasite and Chabazite Can Adsorb Chloride from Synthetic Alkali-Activated Cement Pore Solution

Chapter 4 builds on the work from Chapter 3 providing a qualitative assessment of the chloride binding potential of minerals naturally formed in alkali-activated cements. This chapter shows that the zeolites faujasite and chabazite adsorb chlorides from the highly alkaline cementitious pore solution. The ability of these zeolites to adsorb chlorides in this environment demonstrates the possibility of their role in mitigating chloride diffusivity in alkali-activated cements, something speculated in Chapter 3. This work has been published in the journal *Materials* under the following citation J. Osio-Norgaard and W. V. Srubar, "Zeolite Adsorption of Chloride from a Synthetic Alkali-Activated Cement Pore Solution," *Materials*, vol. 12, no. 12, p. 2019, Jun. 2019, doi: 10.3390/ma12122019.

Abstract

This work presents experimental evidence that confirms the potential for two specific zeolites, namely chabazite and faujasite (with a cage size ~2-13 angstroms), to bear small amounts of chloride from synthetic alkali-activated cement (AAC) pore solution. Four synthetic zeolites were first exposed to a chlorinated AAC pore solution, namely two faujasite zeolites (*i.e.*, FAU, X-13), chabazite (*i.e.*, SSZ-13), and sodium-stabilized mordenite (*i.e.*, Na-Mordenite). Mineralogy and chemical composition were subsequently investigated *via* X-ray diffraction (XRD) and both energy- and wavelength-dispersive X-ray spectroscopy (WDS), respectively. Upon exposure to chlorinated AAC pore solution, FAU and SSZ-13 displayed changes to their diffraction patterns (*i.e.*, peak shifting and broadening) characteristic of ion entrapment within zeolitic aluminosilicate frameworks. Elemental mapping with WDS confirmed the presence of

small amounts of elemental chlorine. Results indicate that the chloride-bearing capacity of zeolites is likely dependent on both microstructural features (*e.g.*, cage sizes) and chemical composition.

Keywords: Alkali-Activated Cements; Zeolites; Chloride Binding; Durability.

1.0 Introduction

Given the worldwide prevalence of chloride-induced corrosion in reinforced concrete, the mechanisms of chloride transport and chloride binding in ordinary portland cement (OPC) paste, mortar, and concrete are generally well understood. Chlorides are transported *via* hydrostatic pressure, capillary absorption, and diffusion [194] and can be bound either as Friedel's salt in cement paste containing limestone or by hydrotalcite in cement paste containing dolomitic mineral phases [195]. These chloride-binding mechanisms are advantageous, given that they chemically retard the rate of chloride ingress.

Despite previous postulation that zeolites could serve a similar function in alkali-activated cements (AACs), analogous chloride-binding mechanisms in AAC paste, mortar, and concrete have not yet been reported. Zeolites, microporous aluminosilicate minerals found in a variety of low-calcium AACs rich in sodium-stabilized aluminosilicate hydrate (N-A-S-H) gels, have been suggested as prime mineral candidates for chloride adsorption given their widespread industrial use as molecular sieves, and adsorbents for anions like SO_4^{2-}, PO_4^{3-} [149,194,196–198]. Recent evidence from Gevaudan *et al.* [6] and Jun *et al.* [158] suggest that two specific zeolites—faujasite and chabazite—have the potential to improve chloride resistance (*i.e.*, reduce bulk porosity and enhance chloride binding), thereby delaying the onset of chloride-induced corrosion. However, neither study presented experimental evidence that confirms the potential for these zeolites to physically or chemically adsorb or entrap chlorides in relevant environmental conditions.

54

The aim of this work was to ascertain whether zeolite minerals commonly found in AAC cement paste, particularly faujasite (FAU), mordenite (MOR), and chabazite, (CHA) are capable of bearing free chlorides. FAU-type zeolites have been observed as reaction products in studies from 2007 to the present [6,193,199–201] with [7] discussing the mineralization dynamics of FAU in alkali-activated metakaolin and how early formation of FAU can lead to reduced permeable porosity. With regards to the presence of MOR in alkali-activated binders, precursors containing MOR, one of the most common naturally occurring zeolites [202], have been frequently activated and reported in the literature [203–208]. Due to MOR's particular reticence and poor solubility in high pH environments [206], a portion of unreacted MOR often remains in the paste. Lastly CHA-type zeolites have also been identified, studied, and reported in the literature [158,209]. In this study, the synthetic zeolites, namely two faujasite zeolites that differed only in their respective cage sizes (*i.e.*, FAU, X-13), chabazite (SSZ-13), and sodium-stabilized mordenite (Na-Mordenite), were exposed to chlorinated AAC pore solution. Zeolite mineralogy and chemical composition were subsequently investigated using *via* X-ray diffraction (XRD) and both energy- and wavelength-dispersive X-ray spectroscopy (EDS/WDS), respectively

2.0 Materials and Methods

2.1. Materials

Faujasite zeolites, FAU (cage sizes ~2-13 angstroms) and X-13 (cage size ~13 angstroms), were obtained from Sigma Aldrich and Fisher Scientific, respectively. Chabazite zeolites (SSZ-13) were provided by Alfa Aesar. Na-Mordenite zeolites (MOR) were supplied by ACS Materials. Sodium hydroxide (NaOH) pellets (97% purity) and powder sodium chloride (NaCl) (97% purity) were provided by Fisher Scientific.

2.2. Methods

Using a modified version of exposure conditions found in Ke *et al.* [156], 1 gram of the powdered zeolites was first exposed to 40ml chlorinated synthetic AAC pore solution with a composition of 0.9M NaOH and 0.1M NaCl for 14 days under constant agitation. The pore solution composition was chosen based on previously published chloride durability studies [156,172] that emphasize the role of alkali hydroxide concentration, while stating that silica, calcium, and aluminum concentrations are typically less than 5mM and that their role on corrosion are negligible in comparison. Pore solution extractions from multiple AACs show that the concentration of alkali hydroxides is at least two orders of magnitude higher than other constituents [75].

Samples were then centrifuged at 4000 rpm for 6 min, and the supernatant was extracted. Solids were rinsed and filtered with 60 mL of deionized water to remove any salts that may have crystallized on the surface and allowed to dehydrate at ambient conditions.

2.2.1 X-Ray Diffraction (XRD)

Qualitative powder XRD analysis of the control and exposed zeolite samples was performed with a Siemens D500 X-ray diffractometer. Samples were analyzed from 5 to 65° 2θ using Cu Kα radiation with a step size of 0.02° and a 2 s dwell time per step. Version 9 of MDI's Jade XRD software was used to identify changes in the control and exposed zeolite diffraction patterns [6].

2.2.2 Energy- & Wavelength-dispersive X-ray Spectroscopy (EDS & WDS)

Using a JEOL-8230 electron microprobe, EDS was utilized to initially screen zeolites for improved chemical mapping. An acceleration voltage of 15 keV and a beam current of 20 nA were used to obtain spectra. With the same instrument, WDS was used to create elemental composition maps of Si Kα, Na Kα, Ca Kα, and Cl Kα. For all samples two Cl Kα maps were aggregated utilizing National Institute of Health (NIH) ImageJ software to obtain better resolution. A similar acceleration voltage of 15 keV, a beam current of 20 nA, and a dwell time of 15 ms were used to obtain all maps.

The electron beam was defocused to 0.5 μm providing a 1:1 ratio between the beam and pixel size. Resulting maps measured approximately 500 μm x 500 μm in area.

3.0 Results

3.1 XRD

Upon exposure to chloride-laden synthetic AAC pore solution, both FAU and SSZ-13 exhibited evidence of peak broadening, shifting, and intensity reductions in comparison to their respective control diffraction patterns (**Figure 10**). Crystallographic theory indicates that these shifts can be due to lattice strain due to the incorporation of ions into zeolitic aluminosilicate frameworks, which has been discussed for both cationic and anionic sorption processes of zeolite [210,211156]. Therefore, the peak shifting and broadening provided indication that these zeolites may have adsorbed free ions (*e.g.*, Na, Cl) from the AAC pore solution. However, these diffraction patterns alone were insufficient to confirm whether FAU and SSZ-13 adsorbed or entrapped free Cl rather than Na (or a combination of the two) in their ionic state. X-13 (**Figure 10b**) and Na-Mordenite (**Figure 10d**) indicated little to no changes to their diffraction patterns after exposure. Of note, the diffraction pattern for Na-Mordenite was the only zeolite sample to indicate the presence of crystalline NaCl post-exposure.
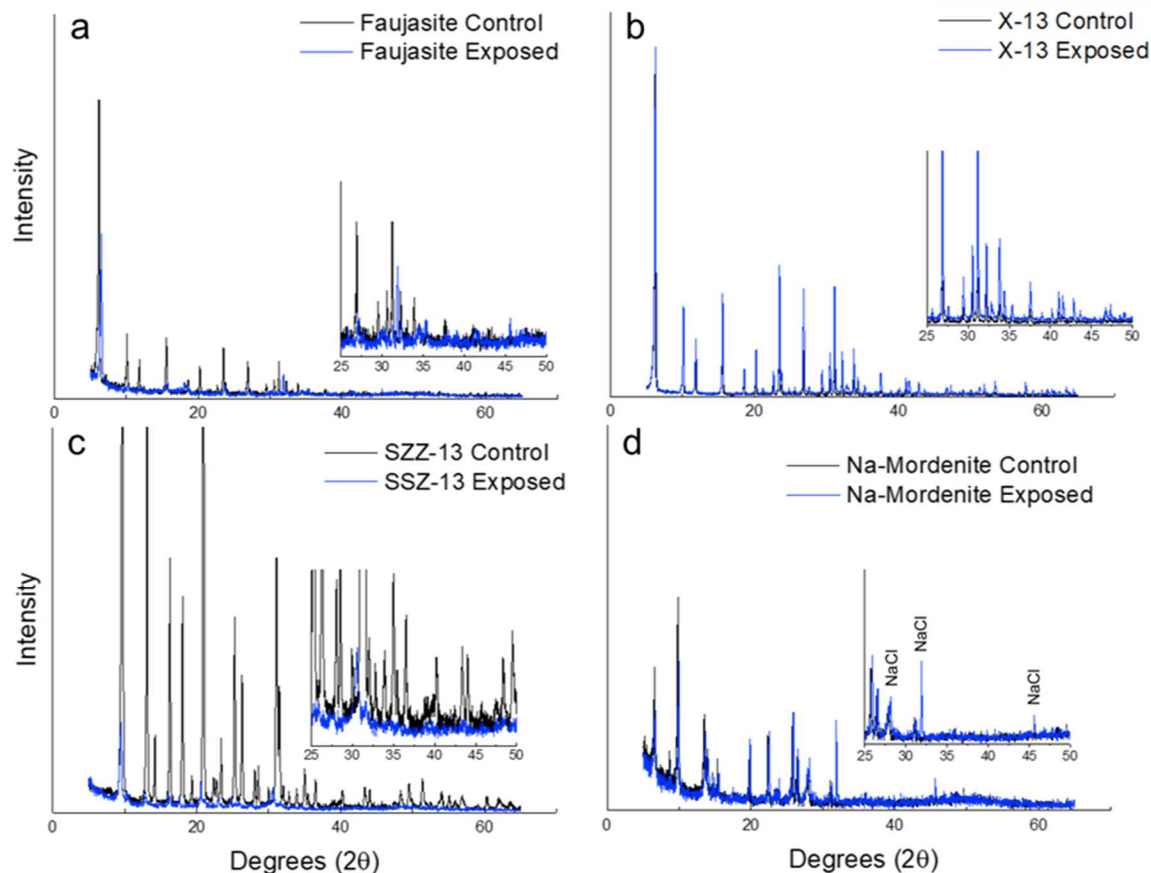
Figure 10. Diffraction patterns of (a) faujasite (FAU) (cage size ~2-13 angstroms), (b) faujasite (X-13) (cage size ~13 angstroms), (c) chabazite (SSZ-13), and (d) sodium-stabilized mordenite (Na-Mordenite).

3.2 EDS & WDS

After confirmation *via* EDS that elemental chlorine was present in FAU and SSZ-13 (**Table 6**), WDS elemental composition maps were obtained to substantiate the presence of small amounts of free chlorides (**Figure 11**). Elemental composition maps for Na-Mordenite and X-13 were also generated, but yielded no presence of Cl higher than background levels. **Figure 11a** and **Figure 11c** indicate that chloride is present in some siliceous regions (*i.e.*, regions of high Si) of FAU and SSZ-13. Silicon (Si) maps were used in this study to visualize the geometry of the aluminosilicate

zeolites. The Na and Cl maps in **Figure 11** suggest that small amounts of elemental chlorine are adsorbed by FAU and SSZ-13 without being bound as NaCl, while **Figure 11c** does indicate the likelihood of the presence of some NaCl in the SSZ-13 sample. Understandably, this result could be interpreted as the formation of crystalline NaCl in FAU and SSZ-13. However, it is of note that both FAU and SSZ-13 zeolites also contain Na before exposure, and significant presence of crystalline NaCl would be detected *via* XRD. The overlap between Si and Na is more prevalent and serves as an indicator that, in this instance, the Na is more than likely part of the original structure of the FAU and SSZ-13 zeolites.

Table 6: Summary of evidence indicating the chloride-bearing potential of zeolites.

Sample	Zeolite	XRD Peak Shifts or Broadening	XRD NaCl Presence	EDS Chlorine Presence	WDS Chlorine Presence
FAU	Faujasite	Yes	No	Yes	Yes
X-13	Faujasite	No	No	No	No
SSZ-13	Chabazite	Yes	No	Yes	Yes
Na-Mordenite	Mordenite	No	Yes	No	No
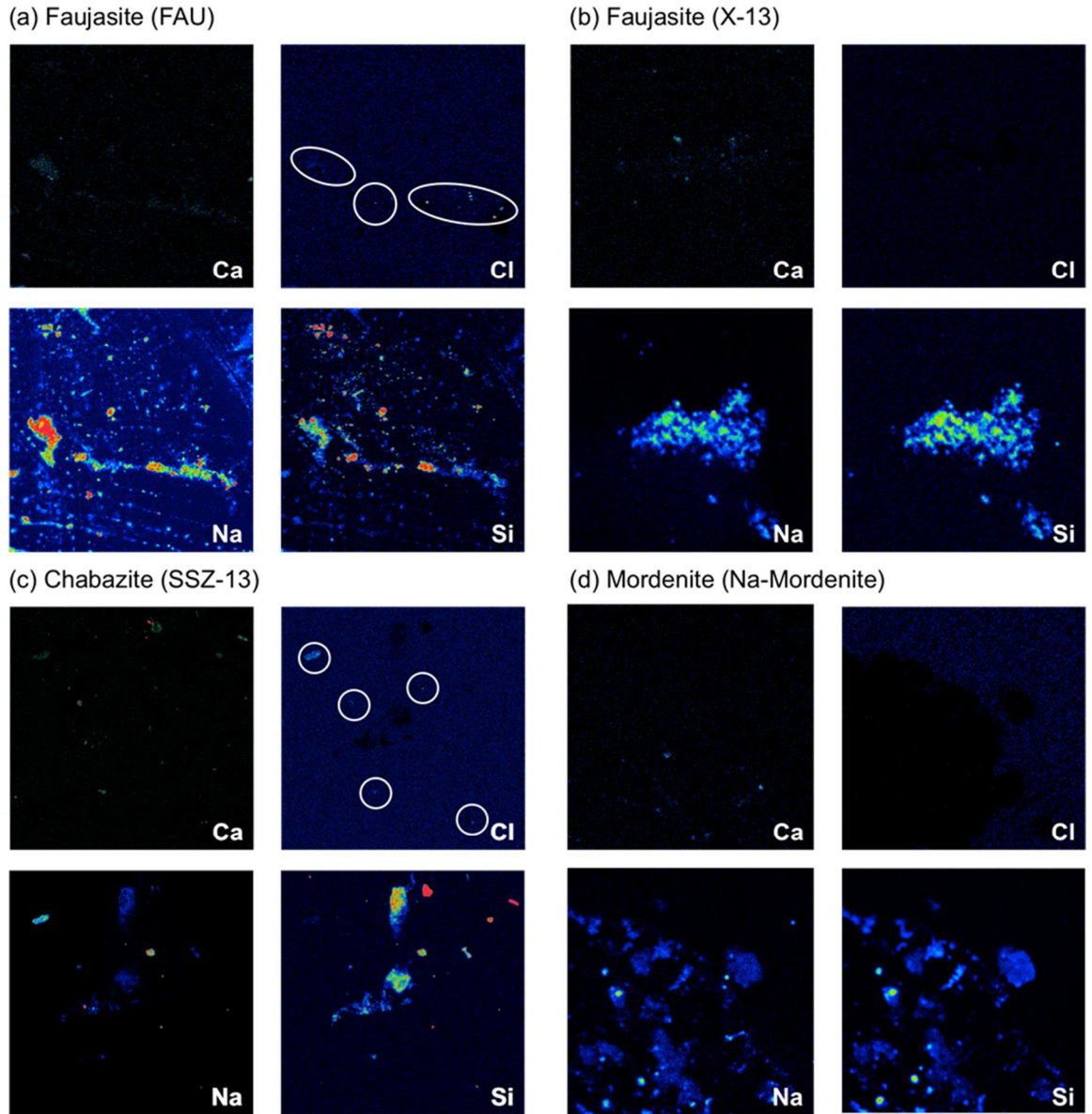
Figure 11: WDS elemental composition maps of chloride-exposed (a) faujasite (FAU), (b) faujasite (X-13), (c) chabazite (SSZ-13), and (d) mordenite (Na-Mordenite).

4.0 Discussion

Taken together, XRD, EDS, and WDS substantiate clear evidence that, while some zeolites are capable of bearing chloride, the capability likely depends on microstructure features, such as cage size, and chemical composition. FAU and X-13—two faujasite zeolites that differ only in cage size—behaved differently in terms of their potential for chloride adsorption. X-13 has, on average, larger zeolitic cages than faujasite, which may enable chloride ions to flow through more freely. Contrastingly, SSZ-13 has a similar average cage size to X-13 but a different chemical composition (*e.g.*, Si:Al ratio [212]), which indicates that cage size is not the only influencing factor.

5.0 Conclusions

This work presents experimental evidence of chloride-bearing potential for two zeolites—faujasite (FAU) and chabazite (SSZ-13)—commonly formed in alkali-activated cement (AAC) paste, mortar and concrete. Results from X-ray diffraction and both energy- and wavelength dispersive X-ray spectroscopy indicated that these zeolites contained small—but non-trivial—amounts of elemental chlorine that was adsorbed from a chlorinated synthetic AAC pore solution after 14 days of exposure. Another faujasite zeolite (X-13) with a larger average cage size than FAU did not exhibit a similar potential to adsorb chlorides. Taken together, these results suggest that the chloride adsorption potential of zeolites is likely linked to both microstructural features and chemical composition. Further research is needed to elucidate and leverage the explicit chloride-uptake mechanisms in these (and other) zeolites, which would enable the design of more chloride-resistant AAC paste, mortar, and concrete.

W.S; visualization, J.O. & W.S.; supervision, W.S.; project administration, W.S.; funding acquisition, W.S.

CHAPTER 5: Silica-Modifying Chemical Admixtures for Directed Zeolitization of Metakaolin-based Alkali-Activated Materials

Chapter 5 discusses the role of chemical admixtures in the formation of potentially beneficial zeolites in an alkali activated cement system. The chapter addresses the formation of zeolites in these mixtures, and their impact on relevant fresh and hardened state properties to better understand controlled zeolitization. This chapter finalizes the discussion of chloride transport in alkali activated cements by demonstrating that zeolitization can be induced. This chapter has been published in *Cement and Concrete Research* under the following citation: Silica-modifying chemical admixtures for directed zeolitization of metakaolin-based alkali-activated materials J Osio-Norgaard, AN Aday, X Chen, SL Williams… - Cement and Concrete Research, 2021

Abstract

The effect of using trimethyladamantyl-ammonium hydroxide (TMAAOH) as a silica-modifying admixture to induce early-age mineralization during alkali-activation of metakaolin was investigated and reported herein. In all material formulations, the use of TMAAOH induced early-age mineralization, increased mixture stiffening in the fresh state, and lowered total heat of reaction. In activating solutions with silica moduli above unity (Ms >1.0), mineralogy results demonstrate that TMAAOH induces the nucleation and growth of metastable zeolitic phases, which correlated with increased permeability and increased plastic shrinkage of the paste. When TMAAOH was added to activating solutions with silica moduli near unity (Ms ~1.0), the controlled formation of crystalline, silica-rich faujasite was observed, which correlated with reduced permeability and lower plastic shrinkage. Together, these results demonstrate for the first time that silica-templating agents such as TMAAOH can be exploited in the deisgn of new

chemical admixtures that directly influence the dynamics of zeolitization in alkali-activated materials.

Keywords: zeolites; mineralization; alkali-activated cements; rheology.

1.0 Introduction

Alkali-activated materials (AAMs) are a class of aluminosilicate cementitious materials produced by mixing aluminosilicate precursor powders (*e.g.*, fly ash, slag, metakaolin) with alkaline activating solutions (*e.g.*, NaOH, KOH). In general, AAMs can be classified by the cemenititous binder that composes them, which varies depending on the calcium content available in the precursor [213]. Low-calcium AAM binders, which contain significantly lower calcium than conventional Portland cement (PC) [193,214,215], predominantly consist of a sodium-stabilized aluminosilicate hydrate framework (*i.e.*, N-A-S-H), although other alkalis can be used as charge-balancing cations. The short-range structure of NASH as a 3D aluminosilicate network has been recently studied and reported in [215].

The distinct chemistry of low-calcium AAMs has permitted their versatile utilization in a wide range of applications from construction [216], water filtration [160], soil stabilization [214], and nuclear waste containment [41], among others [203,217,218]. In the construction industry, AAMs offer a promising alternative to PC materials in certain applications due to lower cradle-to-gate CO_2 emissions, comparable mechanical properties, and, in some cases, improved durability [52,142].

1.1 Mineralogical Composition of AAMs

Understanding and controlling zeolite formation is a critical factor in developing durable microstructures in low-calcium AAMs. The combination of low-calcium aluminosilicate

precursors (*e.g.*, metakaolin, clays) and both high-temperature and high-humidity curing conditions often induces the formation of zeolites [6]. The type, amount, and thermodynamic stability of zeolites that form can vary widely [5,219]. Zeolites are well known to affect the physical, mechanical, and durability properties of AAMs [5]. Zeolitization in AAMs has been linked with reduced porosity [6], potential chloride binding [158,194], mitigation of acid degradation [220], decreased efflorescence due to reduced sodium leaching [7], and heavy-metal and radioisotope immobilization [217,221,222].

Zeolite formtion in AAMs is identical to the sol-gel processes utilized to create synthetic zeolites. Both processes involve Si, Al, and alkali metals (*e.g.*, Na^+, K^+). Gevaudan *et al.* identified that both sodium-to-alumina ratio (Na:Al) and silica availability (*i.e.*, liquid vs. solid silica additions), along with environmental conditions during curing (*i.e.*, temperature, relative humidity) are critical factors that affect the formation of crystalline zeolite phases [6]. More specifically, high silica availability and high Na:Al ratios can lead to the early-age formation of faujasite zeolites in metakaolin-based AAM pastes [6]. Other studies have confirmed that zeolite formation is favored at high alkali (*i.e.*, Na:Al > 1) and low silicon contents (*i.e.*, Si:Al $\leq$ 4), and when cured at elevated temperature and humidty [223,224].

In synthetic chemistry, zeolization can be precision-tailored using organic cationic templating agents (*e.g.*, quaternary ammonium compounds) [225–227]. Briefly, templating agents physicochemically interact with dissolved silica species and induce the nucleation and growth of zeolites in a templating fashion. The resulting zeolite mineralogy and metastability depends precisely on how oxide tetrahedra are structured into specific geometric arrangements [225].

These arrangements are primarily driven by the host-guest interactions between the organic cation and the silicate species that surround it. These interactions are influenced by the size and

shape of the organic molecule, its hydrophobicity (or hydrophilicity), hydrothermal stability, and the rigidity or flexibility of its molecular bonds [225]. Diverse in their functionality, templating agents guide the stabilization of the aluminosilicate framework by initiating the formation—and ultimately dictating—the crystal size, morphology, and chemical composition of zeolites. A thorough review of the structure-directing agent phenomena can be found in [225].

1.2 Scope

The purpose of this study was to use an organic templating agent, namely trimethyladamantyl-ammonium hydroxide (TMAAOH), as a structure-directing chemical admixture for the express purpose of inducing early-age zeolitization in low-calcium AAMs. In addition to zeolitization, the associated effects on reaction kinetics, fresh-state behavior, and bulk material properties of AAM pastes were investigated and reported herein.

2.0 Materials and Methods

2.1 Materials

Metakaolin (MK) (MetaMax) was supplied by BASF (Georgia, USA). The chemical composition of the MK used in this study was previously reported by the authors in [6], and its X-ray diffractogram can be found in **Figure S1**. Reagent-grade sodium hydroxide (NaOH) pellets with >97% chemical purity and sodium silicate (NaSi) M_s=2.5 ($SiO_2 = 27$ wt%, $Na_2O = 11$ wt%, $H_2O = 62$ wt%), were obtained from Sigma-Aldrich (St. Louis, MO, USA). TMAAOH was obtained from SACHEM (Austin, TX, USA). **Figure 12** shows the structure of TMAAOH. Lastly, ethanol (200 proof) was obtained from Fisher Scientific (Hampton, NH, USA).
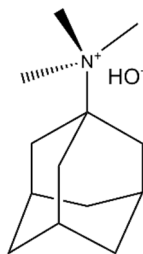
Figure 12: Chemical structure of TMAAOH

2.2 Experimental Methods

2.2.1 Mixture Design & Sample Preparation

Twelve MK-based AAM paste mixtures were prepared by varying the Si:Al and Na:Al ratios according to the mixture design parameters listed in **Table 7**. A liquid-to-solid ratio of 2.0 was held constant across all samples. A TMAAOH:SiO_2 ratio of 0.02 was selected based on previous research reported in zeolite synthesis literature [228–231].

During preparation, the activating solutions were prepared by slowly dissolving the NaOH pellets in deionized (DI) water before adding sodium silicate. After having equilibrated for 24 hours at ambient conditions, the activating solution was manually mixed with MK then together with TMAAOH. The paste was then mechanically stirred for 3 minutes.

While some freshly mixed materials were tested for rheological (section 2.2.2) and calorimetric (section 2.2.3) behaviors, for all subsequent testing, the remaining materials were cast into 12x24mm HDPE cylindrical molds and cured under ambient humidity and pressure at 80 °C. After 7 days' curing, characterization experiments, including X-ray diffraction (XRD), plastic shrinkage, and permeable porosity, were conduced. Additional XRD patterns were also collected after 3 days of curing.

Table 7: Paste mixture formulations without and with TMAAOH addition. Silica modulus (Ms) is equivalent to the SiO2/Na2O molar ratio in the chemical activating solution. Si:Al, Na:Al, TMAAOH:SiO2 refer to the molar ratios of the final mixture.

Mixture	MK (g)	NaSi (mL)	NaOH (g)	Na_2O/100g of Binder	Si:Al	Na:Al	Ms	TMAAOH:SiO$_2$	L/S
1	30	25	5	25.9	1.57	0.92	1.26	0	2.0
2								0.020	
3			10	38.8		1.37	0.84	0	
4								0.020	
5			15	51.7		1.84	0.63	0	
6								0.020	
7		45	5	36.1	2.03	1.28	1.62	0	
8								0.020	
9			10	49.0		1.74	1.19	0	
10								0.020	
11			15	61.9		2.21	0.94	0	
12								0.020	

2.2.2 Rheological Flow Curves

The rheological properties, namely yield stress and plastic viscosity, of MK-based AAM pastes, were determined with a MCR 301 rotational rheometer (Anton Paar, Graz, Austria). A 25 mm diameter stainless steel parallel plate geometry was used for all measurements, and the top plate was cross-hatched to minimize the influence of slip. The temperature was kept constant at 23 ± 0.1 °C, and the gap between the top and bottom plates was maintained at 1 mm. Prior to each test, approximately 700 µL of freshly mixed paste was transferred to the rheometer and subjected to pre-shearing at 50 s^{-1} for 30 seconds, followed by a 60 second rest period. The purpose of these pre-conditioning steps is to reduce the effects of shear history on the pastes and ensure reproducibility in testing [232]. The testing protocol consisted of linearly increasing the shear rate from 0 to 50 s^{-1} in 10 discrete intervals over a period of 100 seconds. At each shear rate, the shear stress was measured, and these data were used to generate flow curves. The pastes were modeled as Bingham plastic fluids [233]. Each flow curve was used to calculate yield stress and plastic viscosity according to the Bingham equation:

$$\tau = \tau_0 + \mu\dot{\gamma} \qquad (1)$$

where τ is the shear stress, τ_0 is the yield stress (Pa), μ is the plastic viscosity (Pa-s), and $\dot{\gamma}$ is the shear rate (s^{-1}).

2.2.3 Isothermal Conduction Calorimetry (ICC)
A TAM Air 8-channel ICC (TA Instruments, New Castle, DE, USA) was used to evaluate the overall heat output of the fresh paste mixes and to identify any zeolitization-induced heat (as described in [41]). The ICC bath temperature was set to 80 °C and allowed to reach equilibrium over 3 days. Afterwards, an hour-long gain validation was performed. Initial and final baselines were measured for 1 hour to minimize signal noise. Around ten grams of freshly mixed paste was poured into glass ampules and placed in the calorimetry chamber at 80 °C. Heat flow data were collected for seven days for all mixtures, and data were normalized by the total mass.

2.2.4 X-Ray Diffraction (XRD)
Qualitative powder XRD analysis was performed with a Siemens D500 XRD (Bruker Corporation, Billerica, MA, USA). Samples were soaked in ethanol for 24 hours after curing to halt time-dependent chemical reactions. Subsequently, these were powdered and mixed with additional ethanol to form a slurry, which was then pipetted onto a single crystal silicon no-background plate. All samples were analyzed from 5 to 65° 2θ using Cu Kα radiation with a step size of 0.02° and a 2s dwell time per step. XRD was performed at 40kV and 30mA.

2.2.5 Hardened-State Properties: Shrinkage, and Permeable Porosity
Cylindrical specimens were removed from the curing chamber and demolded. Height and diameter measurements were taken using calipers. Dimensional plastic shrinkage was calculated by subtracting the diameter of the mold from the average diameter of the specimens after seven days of curing and determining a percent difference. After physical measurements were taken, samples were dewatered using an ethanol gradient to mitigate microcracking according to the following procedure. Samples were initially exposed to a 10% ethanol and water solution for one hour. Every

subsequent hour the ethanol percentage was increased by 20%. Once samples were exposed to a 90% ethanol solution, they were exposed to a 100% ethanol solution overnight [6]. After samples were fully saturated, they were massed (M_{sat}) and placed in an oven at 60 °C for 24 hours [182,234]. Subsequently, the dry masses (M_d) of the samples were obtained. Bulk density was determined by dividing M_d by the cylindrical volume (V_c) calculated from height and diameter measurements for each sample. Lastly, permeable porosity was calculated as the difference between M_{sat} and M_d normalized by the density of ethanol (0.789 g/cm^3) and divided by the sample cylindrical volume:

$$Porosity = \frac{(M_{sat} - M_d)}{0.789 * V_c} \qquad (2)$$

3.0 Results and Analysis

3.1 Effect of TMAAOH on Rheological Properties

The yield stress and plastic viscosity of each paste formulation are reported in **Figure 13**. Data substantiate that the addition of TMAAOH increases both the yield stress and plastic viscosity of the pastes, especially at low Ms and high Si/Al ratios. For example, in the mix with Ms of 0.63 and Si:Al ratio of 1.57, addition of TMAAOH quadrupled the yield stress and doubled the viscosity. Such increases were even more substantial as the Si/Al ratio increased to 2.03, regardless of the Ms value.

The rapid increase in both yield stress and viscosity suggests that TMAAOH interacts chemically with the silicate species in the activating solutions. While a low-Ms value (*i.e.*, with high alkalinity) induces rapid dissolution of the precursor and creates (alumino)silicate oligomers in solution [235–238], a high Si/Al ratio also favors production of the oligomers [239,240]. In either case, these negatively-charged oligomers are stabilized by the cationic sites of TMAAOH, the process known as the "templating effect" of organic molecules. As a consequence, the stabilization of

70

oligomers stiffens the mixture and yields discernible increases in both the yield stress and viscosity of AAM pastes [241,242]. Thus, fresh state evidence indicates that TMAAOH induces a templating—and stiffening—effect during alkali activation of MK as it does during pure zeolite synthesis [243].

This study, in line with previous research, shows that TMAAOH-free MK pastes have yield stresses < 2 Pa (**Figure 13**) [237,244]. The addition of TMAAOH increases the yield stress of all Si:Al=2.0 samples from ~2 Pa to between 11-16 Pa (**Figure 13**).
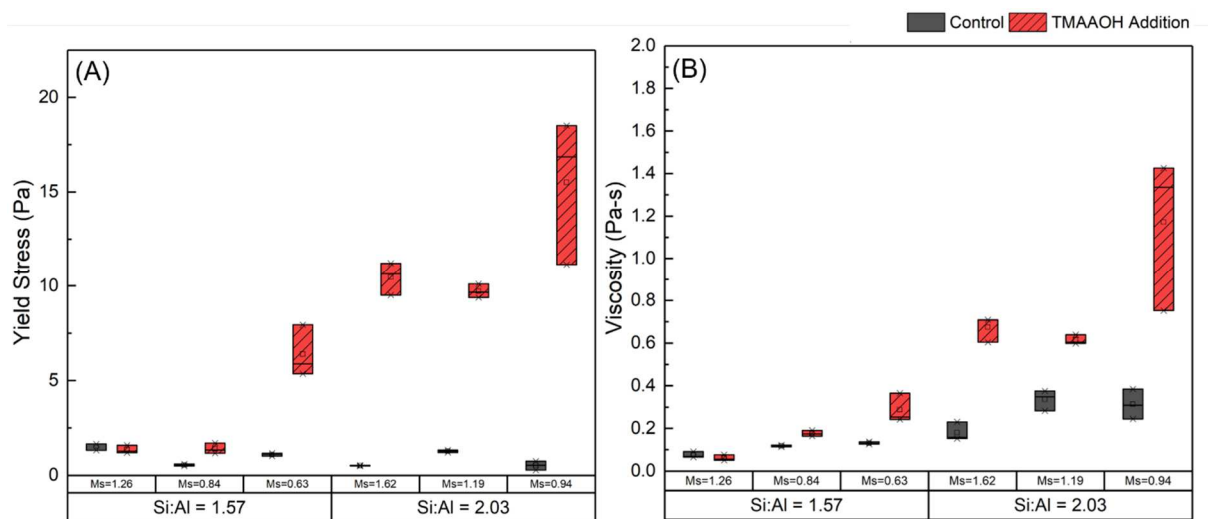
Figure 13: (a) Yield stress and (b) plastic viscosity of MK-based AAM pastes without and with TMAAOH addition. Error bars represent ± one standard deviation (n=3).

3.2 Effect of TMAAOH on Mineralogy

Figure 14 and **Figure 15** present the mineralogical data obtained from the AAMs at Si:Al ratios of 1.57 and 2.03, respectively. It is evident that TMAAOH induced the formation of zeolites, such as faujasite (Si:Al = 2.3), chabazite (Si:Al = 2.1), and sodalite (Si:Al = 1.0), in comparison to non-supplemented controls [245–247]. As explained previously, TMAAOH templates local silica oligomers during alkali activation, which mimics the direct *in situ* crystallization methods for pure zeolite synthesis [225,248]. In this methodology, aluminosilicate gels, produced during alkali-activation,

precipitate onto the organic template, which facilitates zeolite nucleation and growth [231].

Mechanistically speaking, TMAAOH catalytically reduces the thermodynamic activation energy

to nucleate zeolites [225,230,249–251].

The zeolite types induced by the TMAAOH were silicon-rich faujasite and chabazite or

aluminum-rich sodalite. Silicon-rich chabazite has been previously identified in MK and fly ash

activated materials, however, extended-time studies (>84 days) have revealed that this zeolite

phase is largely metastable [252] and will thermodynamically transition to other more stable zeolitic

phases over time. The identified zeolites were found to depend on the Ms value of the activating

solution as discussed in the following section.
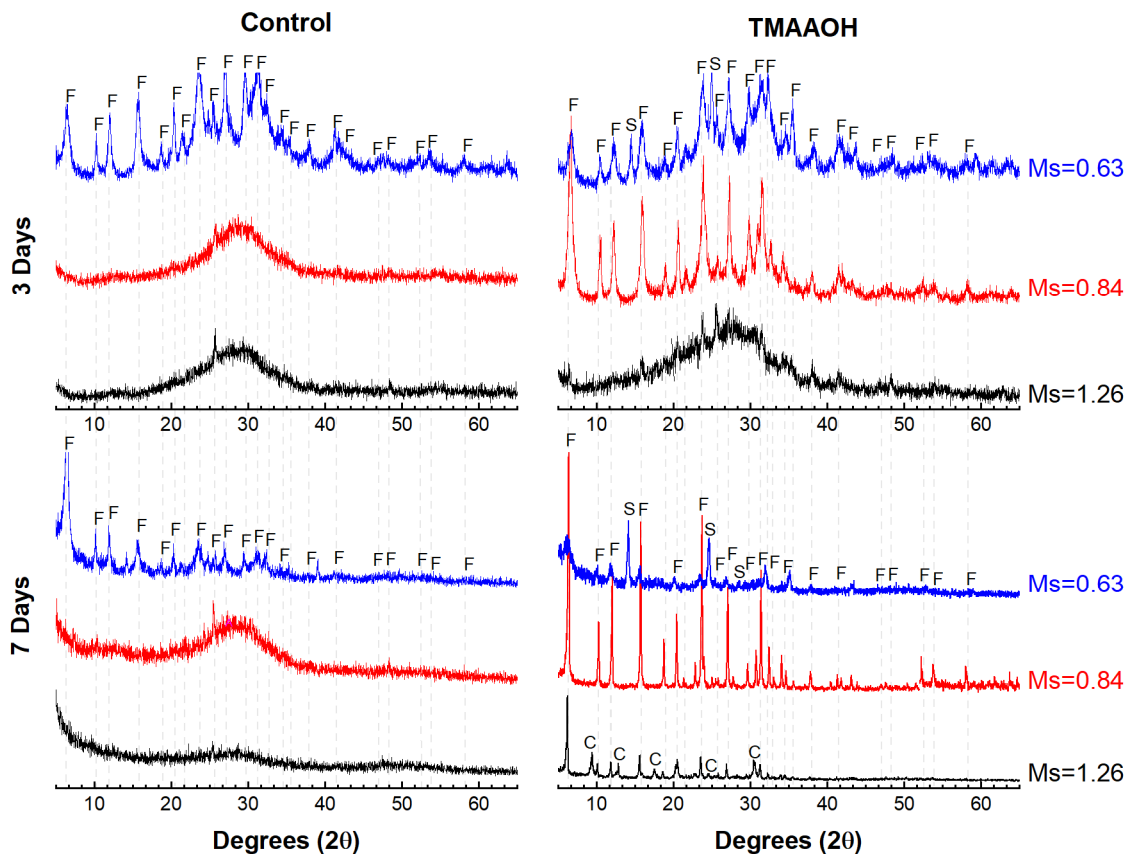
Figure 14: X-Ray diffractograms of alkali-activated MK with Si:Al=1.57 at three (72 hours) and seven days (168 hours). C=Chabazite (Si:Al = 2.1, PDF 00-019-1178), F=faujasite (Si:Al = 2.3, PDF 00-012-0228), S = Sodalite Octahydrate (Si:Al = 1.0).

In activating solutions with silica moduli (Ms) higher than unity (>1.0), zeolite nucleation induced by TMAAOH favored silicon-rich minerals (*i.e.*, chabazite and faujasite). From **Figure 14** and **Figure 15**, it is evident that chabazite only forms after 7 days of curing in formulations with: (Si:Al = 2.0, Na:Al = 1.28), (Si:Al = 1.57, Na:Al = 0.91), and (Si:Al = 2.0, Na:Al = 1.38). These formulations have Ms values of 1.19, 1.26, and 1.62, respectively. It is well known that a Ms >1.0 promotes the formation of silica oligomers (*e.g.*, bridged cyclic tetramers, cyclic trimers, and linear trimers), which would yield better interaction with TMAAOH, as previously explained [239,240]. Besides interacting with the initial activating solution, the TMAAOH, with a lower ratio of charge per molecule size compared to Na^+, more likely stabilizes higher Si:Al aluminosilicates that possess a lower number of balancing negative charges [253]. During alkali-activation, nucleation of these zeolites results from precipitated aluminosilicate gels similar to the 'gel 2' described in [254] (Si:Al ~2.0).

In contrast, the use of activating solutions with Ms lower than unity (Ms = 0.63) yields the formation of low Si:Al zeolites as verified by the formation of sodalite in formulations with (Si:Al = 2.0, Na:Al = 1.74). In these low-Ms activating solutions, the majority of silica species are monomers with remnant dimers and trimers [238–240,255]. These species are highly reactive and favor the rapid formation of low-Si:Al gels termed "gel 1" [239,254]. Moreover, the formation of sodalite zeolites may also be due to an out-competition of Na^+ over the $TMAA^+$ cations for sorption surface sites on precursor particles, as seen in a similar system with combined organic-inorganic cations [256]. XRD data confirm TMAAOH's utility in inducing early-age mineralization in AAMs [257,258].
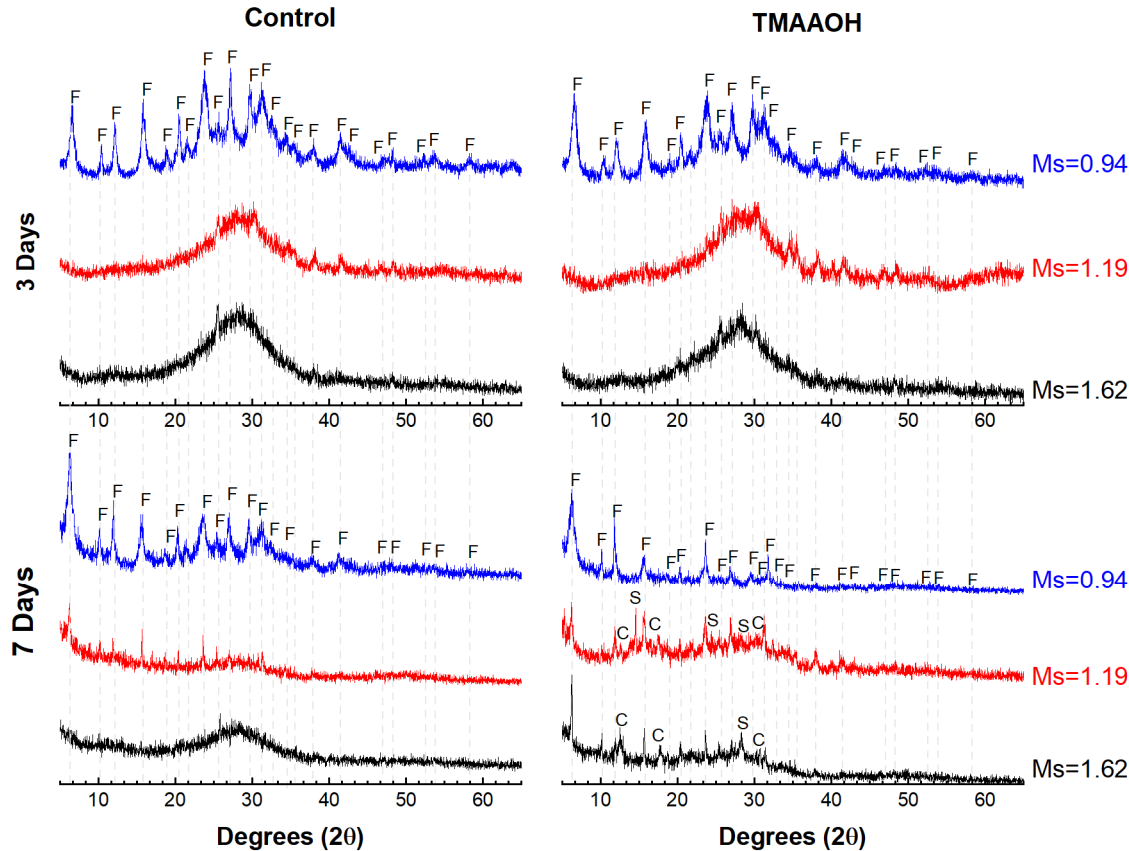
Figure 15: X-Ray diffractograms of alkali-activated MK with Si:Al=2.0 at three (72 hours) and seven days (168 hours). C=chabazite (Si:Al = 2.1, PDF 00-019-1178), F=faujasite (Si:Al = 2.3, PDF 00-012-0228), S = Sodalite Octahydrate (Si:Al = 1.0).

3.3 Effect of TMAAOH on Reaction Kinetics

Figure 16 shows the heat evolution of the MK pastes without and with TMAAOH addition. The exothermic peaks exhibited in this figure correlate with mineral formation (see **Figure 14** and **Figure 15**) and provide direct evidence of mineralization thermodynamics occuring in these samples. For example, (Si:Al = 1.57, Na:Al = 0.91) formulations with TMAAOH and Ms = 1.26 exhbit higher heat evolution during alkali activation (100.7 J/g) and reach peak heat at earlier timepoints (~30 hours earlier). These results correlate well with XRD, which substantiate that TMAAOH addition in these samples increases the degree of mineralization (content of minerals) by forming silicon-rich zeolites, such as faujasite and chabazite.
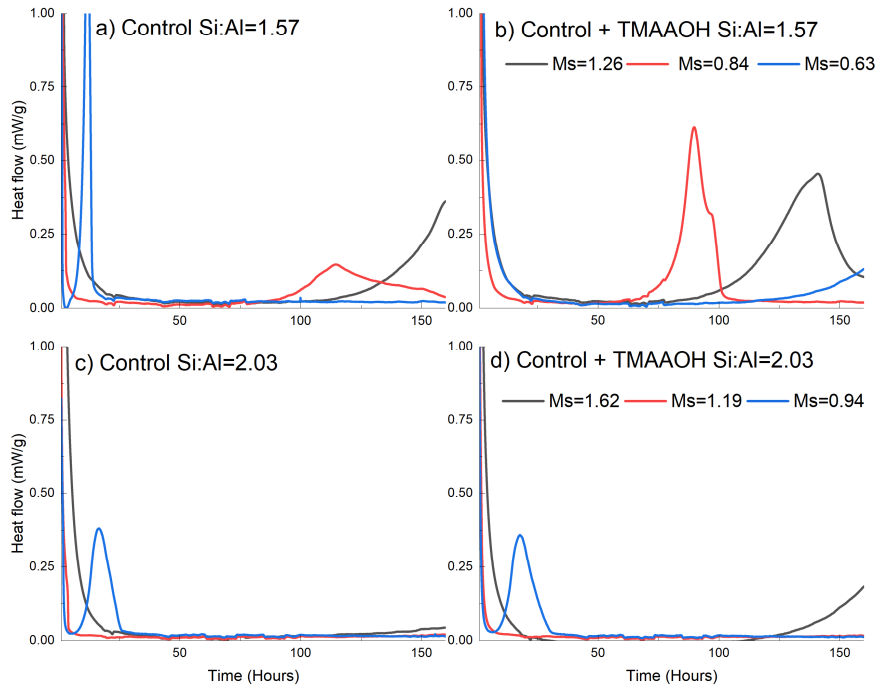
Figure 16: Normalized heat flow curves of alkali-activated MK paste formulations with Si:Al=1.57 and Si:Al=2.03, as indicated within the figure (168 hours).

As observed in **Figure 16b**, formulations with TMAOOH at Si:Al=1.57 and increasing Na:Al ratios resulted in rapid early-age mineralization. For example, control samples (**Figure 16a**) with a Na:Al=1.84 displayed two exothermic peaks before 3 days, which correlated with faujasite formation in the first 10 hours as observed *via* XRD. Alternatively, samples with TMAOOH exhibit one initial peak and the formation of both faujasite and sodalite (**Figure 14**). Hence, only in the presence of TMAAOH and a low Ms, zeolite nucleation is accelerated and occurs in the first few hours upon activation. This finding is consistent with the *in-situ* crystallization mechanisms of 'gel 1' explained earlier. While the formation of low Si:Al 'gel 1' proceeds rapidly [259,260], evidence obtained herein indicated that TMAAOH further accelerated this process *via* zeolitization

in this sample. Similar TMAAOH-induced acceleration was observed for formulations of the same silica content and lower Na:Al ratios.

Samples with a Si:Al=2.03 (**Figure 16c** and **Figure 16d**) exhibited similar behavior regardless of TMAAOH addition. Further analysis of the total heat released from these samples is summarized in **Table 8.** The results indicate that a slight increase (8%) in total heat at 7 days is observed for formulations with TMAAOH and activating solutions with Ms values near unity (Si:Al =2.0, Na:Al = 2.2). An increase in total heat, as discussed previously, indicates a larger extent of mineral (*i.e.*, faujasite) formation. Contrastingly, formulations with the same silica content and TMAAOH but activated with solutions of higher Ms yield up to 35% lower heat of reaction. Reductions in the heat flow produced during alkali activation and curing are beneficial in regard to reduced thermal shrinkage.

Table 8: Total heat flow from isothermal calorimetry data for all AAM formulations.

Ms	0.63		0.84		0.94	
Na/Al	1.84		1.37		2.2	
Si/Al	1.57		1.57		2.03	
Sample	Control	TMAAOH	Control	TMAAOH	Control	TMAAOH
Heat (J/g): 3 days	109.6	67.5	89.3	84.3	73.6	81
Heat (J/g): 7 days)	116.6	80.5	111.7	117.6	79	85.7
Ms	1.19		1.26		1.62	
Na/Al	1.74		0.91		1.28	
Si/Al	2.03		1.57		2.03	
Sample	Control	TMAAOH	Control	TMAAOH	Control	TMAAOH
Heat (J/g): 3 days	75.1	74.2	54.9	47	81.3	45.9
Heat (J/g): 7 days)	80	78.7	83.6	100.7	88.7	56.5

3.4 Effect of TMAAOH on Permeable Porosity and Plastic Shrinkage

The permeable porosities of samples without and with TMAAOH are shown in **Figure 17**. As previously discussed, formulations with Ms >1.0, TMAAOH induced the formation of chabazite, a metastable phase (see **Figure 14** and **Figure 15**). As expected from the authors' previous work [6], the formation of this metastable phase leads to an average increase in the permeable porosity (see **Figure 17**). For example, formulations Ms=1.62 and Ms=1.19 form chabazite and exhibit an increase in mean permeable porosity of 10% at 7 days. Interestingly, chabazite in Ms=1.26 samples do not reveal significant changes in mean permeable porosity, but a larger data variance is observed. In addition, Ms=0.63 samples, which were activated with the lowest Ms activating solution, demonstrated rapid mineral formation (**Figure 16**), which led to an increase (7%) in the mean permeable porosity after seven days of curing.
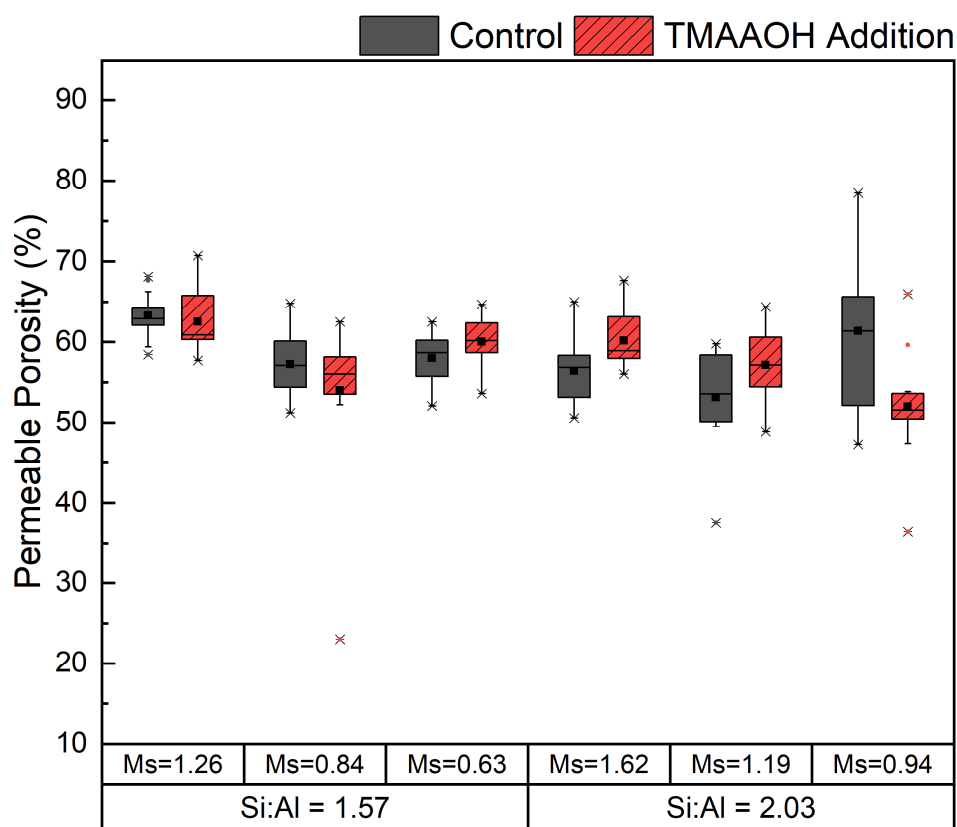
Figure 17: Permeable porosity of MK pastes without and with TMAAOH addition after 7 days of curing, n = 9.

AAMs activated with TMAAOH and Ms near unity demonstrate an equal or lower permeable porosity as those without TMAAOH (**Figure 17**). This lower permeable porosity is attributable to a greater extent of faujasite formation. Early-age faujasite mineralization was confirmed *via* XRD (**Figure 14** and **Figure 15**) and evidenced in calorimetry measurements (**Figure 16** and **Table 8**). More specifically, TMAAOH addition reduced the mean permeable porosity in mixtures with Ms=0.84 and in mixtures with Ms = 0.94) 1% and 16%, respectively (see **Figure 17**). As explained by the authors in [6] and further confirmed by [261], the controlled growth of a silicon-rich zeolite (*i.e.*, faujasite) lowers the permeable porosity in low-calcium AAMs. Interestingly, these reductions in permeable porosity seem to be unrelated to the framework density of the zeolites formed.

Although chabazite (15.1T/1000A) and sodalite (16.7T/1000A) have greater framework densities than faujasite (13.3T/1000A) and are thereby less porous, the mixes in which these zeolites developed exhibit a greater permeable porosity than those where exclusively faujasite formed. This perhaps indicates that the time at which the zeolites develop has a greater influence on permeable porosity than the type of zeolite formed. These results provide a limited picture of the effect of TMAAOH on the porosity and microstructure of the alkali activated metakaolin. The high water content of the samples and the tests inability to assess the mesoporosity of the formed zeolites indicate that further testing should be performed to observe changes in other meaningful properties such as the pore size distribution. The results of the permeable porosity should serve as a proxy measurement to initially assess some of the potential microstructural changes.

Figure 18 shows the plastic shrinkage measurements of all pastes. In line with permeable porosity results, the plastic shrinkage of AAMs is lowered when TMAAOH is included as a chemical admixture with activating solutions with a Ms ~1.0. In samples without TMAAOH, there is an expected increase in shrinkage with increases in both Na:Al and Si:Al ratios [262]. Different shrinkage mechanisms apply to TMAAOH-supplemented samples. When TMAAOH is added to AAM mixtures, the rapid nucleation of some stable zeolites (*e.g.*, sodalite) and metastable phases (*i.e.*, chabazite) can result in the formation of silicon-rich N-A-S-H binders susceptible to shrinkage [6]. As previously noted, these mineral dynamics are a result of Ms > 1.0 in the activating solutions. At Ms ~1.0, plastic shrinkage is decreased by 20%, due to a stable increase of faujasite forming in these samples, as evidenced by XRD and isothermal calorimetry. These rudimentary measurements of both permeable porosity and plastic shrinkage provide an initial picture of the impact TMAAOH has on the hardened state properties of these AAM mixtures. However, further studies should be conducted to elucidate the impact TMAAOH (or other SDAs) have on the

various types of shrinkage experienced by these materials (*e.g.* drying shrinkage). Taken together, these results illustrate the potential efficacy of using TMAAOH in combination with activating solutions with Ms ~1.0 to achieve a denser microstructure and lower permeable porosity.
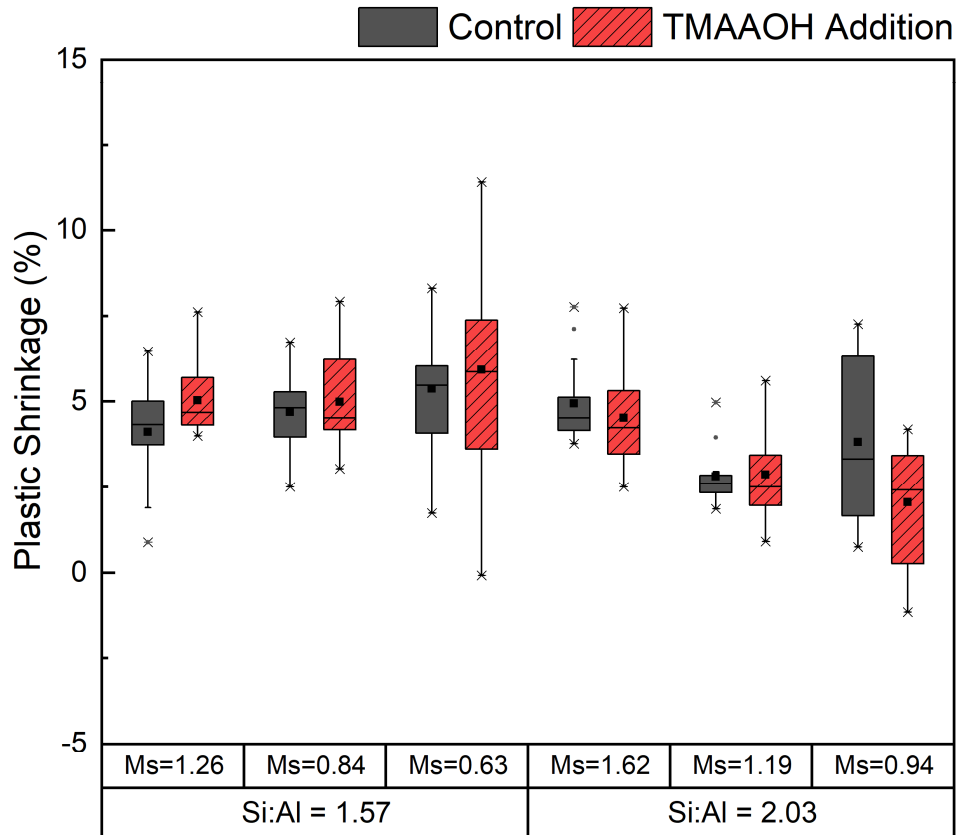
Figure 18: Plastic shrinkage of alkali-activated MK paste formulations without and with TMAAOH addition after 7 days of curing (n = 9).

4.0 Significance and Future Research

By merging the fields of artificial zeolite synthesis with AAMs, this proof of concept work demonstrates that organic templating agents can be used to manipulate reaction kinetics, early-age

microstructural development, and both fresh- and hardened-state properties of AAMs. Incorporating templating agents as novel AAM admixtures could increase their tailorability and lead to performance improvements. For example, the controlled development of early-age faujasite in this study could lead to beneficial mineralogical and microstructural changes. We showed that, when templating agents are utilized in activating solutions with a Ms near unity, the early-age formation of faujasite can reduce the volume of permeable pores – a critical factor that reduces chloride diffusivity and, in general, improves long-term durability [6]. Moreover, it is suspected that faujasite and chabazite themselves have the potential to affect chloride transport by increasing chloride binding [37], which could lead to increased chloride binding within these microstructures. Beyond the zeolites templated in this study, other zeolites like 13X FAU, a well-known CO_2 sorbent [263], could be templated to increase CO_2 capture in geopolymer pastes. The potential for process-structure-property exploration into how various templating agents and their chemistries interact with geopolymerization to mineralize the desired zeolites provides a fruitful new area of research related to *mineralization* or *zeolitization admixture* technology.

Furthermore, the work herein demonstrated that templating agents could be developed into a new class of *viscosity-modifying admixtures* for geopolymer pastes. Our results show that the incorporation of TMAAOH increased yield stresses of MK geopolymer pastes regardless of Si:Al or Na:Al ratio. Future research is needed, however, to test a suite of chemically tailored viscosity modifying admixtures, which could be developed using one or more various templating agents in combination. Developing various viscosity-modifying admixtures would widen the range of AAM applications, especially those involving additive manufacturing in 3D concrete printing.

It is important to note that this work has some inherent limitations. A limited number of mixes were explored, all with high liquid to solids ratios, which generally led to high porosities.

Additional research would be needed to design and optimize mixtures with SDAs for specific applications to achieve target physical and mechanical properties and acceptable durability performance.

5.0 Conclusion

In this study, we demonstrated that TMAAOH could be utilized as a new chemical admixture in AAMs to induce the early-age formation of silicon-rich zeolites. TMAAOH is observed to directly affect the polycondensation of silica species during alkali-activation, which manifested as quantifiable increases in yield stress and plastic viscosity of the mixtures. Such increases were observed to be much higher for mixtures activated with silica moduli near unity (Ms ~1.0). This observation indicates that TMAAOH will preferentially interface with short-chained silica oligomer species.

The enhanced formation of faujasite *via* TMAAOH templating is attributable to its capability of nucleating a high Si:Al framework. The results suggest that TMAAOH follows a direct *in situ* crystallization methodology, which favors the precipitation of aluminosilicate gels and consequent zeolite nucleation. When TMAAOH was utilized with Ms above unity (Ms >1.0), samples were observed to form faujasite and chabazite (**Figure 14** and **Figure 15**), two well-known silicon-rich zeolites. The formation of chabazite, a metastable zeolite, led to increases in permeable porosity and plastic shrinkage. Contrastingly, the controlled formation of faujasite with activating solutions having a Ms ~1.0 and TMAAOH resulted in reduced permeable porosity and plastic shrinkage. Lastly, the total heat of reaction for samples including TMAAOH was lower than their control formulations.

The results presented herein indicate the need for further investigation into the potential for structure-directing agents to serve as potential mineralization or zeolitization admixtures to

tailor the fresh- and hardened-state properties of AAMs. Furthermore, this study highlights the possibility of investigating other templating agents for material-modifying properties, as well as an ability to induce the formation of useful zeolites. For example, this new class of chemical admixtures could promote the formation of functional zeolites in AACs that further densify the microstructure, increase chloride binding, reduce chloride transport, and enhance *in situ* CO_2 sequestration.

6.0 Acknowledgments

CHAPTER 6: Sintering of 3D Printable Simulated Lunar Regolith Magnesium Oxychloride Cements

Chapter 6 begins this dissertations discussion of ISRU and its applications for space exploration.

It details the applications of powder binder jetting printing as a means of additive manufacturing,

and it explores the usage of sintering as both a strengthening mechanism for magnesium oxychloride cements and a water and chloride recovery mechanism to minimize the usage of scarce materials. This chapter has been published in *Acta Astronautica* under the following citation: Sintering of 3D printable simulated lunar regolith magnesium oxychloride cements

J Osio-Norgaard, AC Hayes, GL Whiting- Acta Astronautica, 2021

Abstract

This study investigates the formulation, processing, hardened state properties, and additive manufacturing of sintered 3D-printable simulated lunar regolith magnesium oxychloride (MOC) cements. Sintering of these materials up to 1200 □ leads to full decomposition of the lunar regolith based MOC cement with release of HCl and water, which could potentially be captured and reused without compromising material properties. The sintering process reduces porosity and increases compressive strength, particularly when the material is initially pre-dried. 3D print manufacturing of the simulated lunar regolith cement is demonstrated using a powder binder jetting technique, showing expected pattern reproduction suitable for the manufacturing of small-scale parts. This material and processing approach could provide opportunities for future lunar fabrication of parts using additive manufacturing and in-situ resources, reducing the need for dedicated manufacturing facilities, distant transport of materials, and minimizing water demands through partial recovery during processing.

Keywords: Magnesium oxychloride cement, ISRU, sintering, additive manufacturing

1.0 Introduction

Additive manufacturing using in-situ resources (ISRU) can facilitate future off-planet habitation by enabling development of infrastructure and other objects without the need for dedicated manufacturing facilities or distant transport of materials. Previous research into ISRU for the production of cementitious binders [12,13,264–266], makes it clear that a large demand for water exists. As water is a scarce off-planet resource, water demand for infrastructure directly competes with the demand for other crucial applications. As such, there is benefit in developing methods to recover water from these cementitious binders while producing a material that meets specific performance targets.

Lunar regolith based magnesium oxychloride (MOC) cements are a promising candidate for water recovery. These cements are based on the reaction between MgO and a $MgCl_2$ solution (**equation 1**) producing an assortment of gel phases that lead to a high-compressive strength binder that can incorporate a large amount of filler material, such as lunar regolith [267]. The properties of MOC cements depend on a variety of parameters such as: precursor molar ratios (e.g. $MgO:MgCl_2$, $MgO:H_2O$), curing temperature, and the calcination temperature of the MgO [267].

$$5MgO + MgCl_2 + 13H_2O \rightarrow 5Mg(OH)_2 \cdot MgCl_2 \cdot 8H_2O \ (1)$$
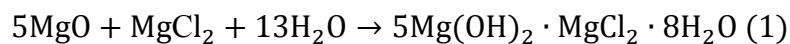
MOC cements have been previously studied for ISRU additive manufacturing approaches [12], where powder binder jetting printing was utilized to produce large scale components fabricated out of DNA-1 lunar simulant supplemented with MgO. This study evaluated the feasibility of producing MOC cements in vacuum conditions, leading to the suggestion that these cements could be utilized in off-planet applications [12]. Building from this previous study, here we investigate the impact of post processing on MOC cements, enabling a wider range of mechanical properties due

to the densification of the cement matrix and providing a method for water recovery, potentially allowing for increased application potential beyond large scale structures.

1.1 Scope

The goal of this work is to demonstrate the feasibility of sintering previously studied [12] MOC based lunar regolith cements utilized in additive manufacturing applications. Sintering these cements creates the possibility of precursor material recovery *via* the decomposition of the MOC cement, while producing a ceramic like material. This work explores how sintering affects the mineralogical composition of the binder, and its hardened state properties. Additionally, this study demonstrates that it is feasible to additively manufacture and sinter small scale non-structural components using this material.

2.0 Materials and Methods

2.1 Materials

Lunar Highland Simulant-1 (LHS-1) was supplied by the University of Central Florida Exolith Lab (Orlando, Fl, USA), **Table 9** shows the oxide composition of the material, as reported by the provider. Reagent grade magnesium chloride ($MgCl_2$) with 98% chemical purity was obtained from Sigma-Aldrich (St. Louis, MO, USA). Magnesium oxide (MgO) was procured from Inframat Advanced Materials (Manchester, CT, USA) with chemical purity of 99.5%. Lastly, ethanol (200 proof) was obtained from Fisher Scientific (Hampton, NH, USA).

Table 9: Oxide composition of LHS-1

Oxide	SiO_2	Al_2O_3	CaO	MgO	FeO_T	Na_2O	TiO_2	K_2O	SO_3
Wt.%	44.18	26.24	11.62	11.22	3.04	2.30	0.79	0.46	0.10

2.2 Methods

2.2.1 Mixture design

Powdered LHS-1, MgO, and $MgCl_2$ were manually blended into a homogenous mixture according to the proportions given in **Table 10**. The blended powders were subsequently mixed with DI H_2O. Samples were manually stirred for 3-minutes and cast in 14x34 mm cylindrical molds. Samples were then cured (*i.e.*, allowing the hydration reaction to move forward leading to the cement hardening) at room temperature and humidity for seven days. Note that for printed samples, a liquids-to-solids (l/s) ratio of approximately 0.23 was utilized.

Table 10: Magnesium oxychloride cement paste mixture design.

LHS-1 (g)	MgO (g)	H_2O (g)	$MgCl_2$ (g)	l/s (wt%)	liquid/binder (wt%)	$MgCl_2$:H_2O (wt%)
100	20	36	10.8	0.30	1.5	0.30

2.2.2 Thermogravimetric Analysis & Sintering

Thermogravimetric analysis (TGA) was performed on the cementitious samples with a TGA 5500. Samples were allowed to equilibrate to 25 □ before the temperature was increased to 110□ at a rate of 10□/min. The temperature was held at 110 □ for 30 min, and subsequently increased to 800□ at a rate of 100□/min. Temperature was held constant at 800 □ until no further mass loss was observed.

Samples were sintered in a Mellen Microtherm box furnace (The Mellen Company, Concord, NH), in an air atmosphere. Sintering was conducted at 1200 □ for 6.5 hrs with a ramp rate of 20 □ /min. Samples were cooled to room temperature with the same ramp rate. Two types of samples were sintered: samples containing pore water solution and oven dried samples. Samples containing pore water were sintered immediately after demolding, while pre-dried

samples underwent an ethanol solvent exchange and were oven dried at 60 ☐ for 24 hrs to remove all pore water prior to sintering.

2.2.3 X-Ray Diffraction

A SCINTAG X1 Diffraction System was utilized to obtain diffraction data. Samples were ground with a mortar and pestle and a powder layer was placed on a glass slide coated with petroleum jelly. All samples were analyzed from 10 to 75° 2θ using Cu Kα radiation with a step size of 0.05° and a 2.5 s dwell time per step.

2.2.4 Dimensional Shrinkage & Permeable Porosity

Shrinkage was calculated by subtracting the diameter of the mold from the average diameter of the specimens after post-curing and post-sintering. Height and diameter measurements were collected utilizing calipers, and subsequently samples were immersed in ethanol according to the following procedure. Initially samples were exposed to a 10% ethanol and water solution for one hour. Every subsequent hour the ethanol percentage was increased by 30%. Finally, samples were exposed to a 100% ethanol solution overnight to achieve saturation [6]. After samples were fully saturated, the masses were obtained (M_{sat}) and they were placed in an oven at 60 °C for 24 hours [6,38]. Subsequently, the dry masses (M_d) of the samples were obtained. Finally, the volume of permeable pores was calculated as the difference between M_{sat} and M_d normalized by the density of ethanol (0.803 g/cm^3) and divided by the sample cylindrical volume V_c (**Equation 2**).

$$Porosity = \frac{(M_{sat}-M_d)}{0.803*V_c} \ (2)$$

2.2.5 Compressive Strength

To determine the compressive strength, 14 mm x 34 mm (diameter x height) cylindrical samples were placed on an INSTRON 5889 compression load frame with a 50 kN load cell. Samples were strained at a rate of 0.025 mm/s. Due to the size of the samples, no

preloading was attempted. The average compressive strength of three trials is reported.

2.2.6 Powder Binder Jet Printing

A commercially available powder binder jet printer (Z Corp 650, Z Corporation, Burlington, MA) was used to demonstrate the printability of lunar regolith MOC cements. The printer has a volume of 254 mm x 381 mm x 203.2 mm (10 in x 15 in x 8 in) and prints at a rate of 2-4 layers per minute at 100 μm layer thickness. The printer uses five printheads (HP 11, Hewlett-Packard, Corvallis, OR) to deposit binder at a resolution of 600 x 540 dots per inch. The LHS-1, $MgCl_2$, and MgO were mixed and added to the powder feeder of the printer. A 99.5% water and 0.5% surfactant ink was deposited during printing. Parts were allowed to cure in the printer at 35 °C for 2 hrs. post print and allowed at least 24 hours to set at room temperature in the printer before de-powdering.

3.0 Results and Discussion

3.1 Thermogravimetric Analysis and Sintering

Thermogravimetric analysis was performed to assess the full decomposition of the magnesium oxychloride phases. **Figure 19** shows the decomposition of the cementitious binder at 800□. The initial mass loss at 110□ can be attributed to the loss of un-bound cement pore water in the paste, while subsequent mass loss is due to the decomposition of the MOC. MOCs undergo a multi-stage decomposition at temperatures of between 450-500 □ leaving residual MgO and releasing H_2O and HCl gas [268] as per the reaction in **Equation 3**. This decomposition results in an approximate mass loss of 14% from the cementitious binder, which accounts for approximately 54% of the of the total mass of chlorine and water added to the mixture.

$$5Mg(OH)_2 \cdot MgCl_2 \cdot 8H_2O(s) \rightarrow 6MgO(s) + 12H_2O(g) + 2HCl(g) \ (3)$$
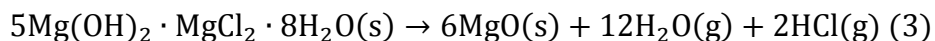
Understanding that the MOC cement fully decomposes over a period of approximately 100 min. at 800 □, several attempts at sintering were performed. Temperatures below 1200 □ yielded a material that crumbled upon removal from the furnace. Likewise, sintering times under 6.5 hours led to materials that failed upon removal from the furnace. The minimum sintering time was the time required for the full decomposition of the MOC paste, and time increments were tested until an optimum sintering time of 6.5 hours was selected. As **Figure 19** shows, no further mass-loss during the isothermal hold at 800 □ (250-300 □ above the MOC decomposition temperature) is observed, further increases in temperature tested beyond that threshold lead only to a densification of the microstructure and improved mechanical properties (*i.e.* increased compressive strength) without further mass-loss.

Pre-sintering sample processing was determined based on the results of samples sintered at 1200 □, as they were the first samples that did not fail upon removal from the furnace. Unprocessed MOC paste samples sintered at 1200 □ exhibited a large degree of cracking and warping due the flash heating of the cementitious pore water. Therefore, a drying process to initially remove the pore water was included for comparison. Pre-dried samples exhibited less external cracking and warping than their pore-water containing counterparts.
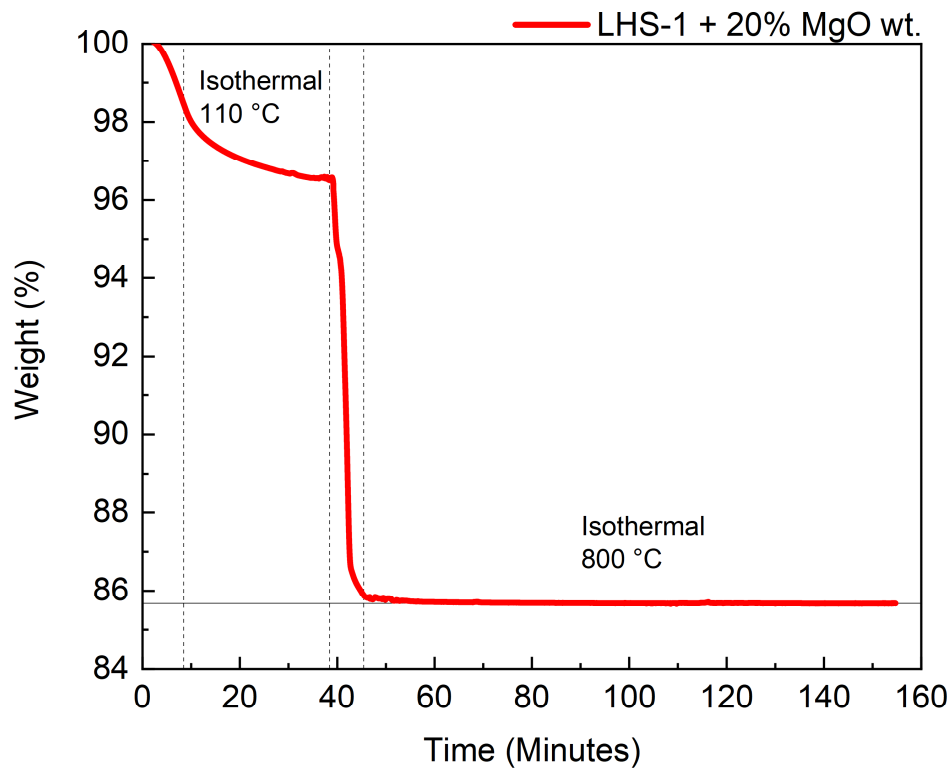
Figure 19: Thermal decomposition of MOC paste at 800 □. Samples were initially allowed to equilibrate to 25 □. The temperature was then increased to 110 □ at a rate of 10 □/min and an isothermal hold was set for 30 minutes to allow for pore water evaporation. Sub

The goal of sintering the MOC paste was to obtain a material that retained or improved upon the hardened state properties of the MOC paste (*i.e.,* increased compressive strength and reduced porosity), while providing a mechanism by which the magnesia, water and chlorine utilized in the mix could be recovered. Sintering has previously been suggested as a way to recover volatiles from lunar regolith, this methodology could be utilized to both recover volatiles from existing regolith and to recoup the water and other precursors invested into the development of ISRU materials [266].

3.2 X-Ray Diffraction

Figure 20 shows diffractograms of the precursor materials, the MOC paste after seven days of curing, and the sintered material. As expected, the precursor materials (LHS-1 + 20% MgO) shows primarily anorthosite and MgO peaks; the materials are predominantly crystalline. The MOC binder shows typical peaks of a phase 5 cement [269], and additionally the development of $Mg(OH)_2$. The MgO has been fully incorporated into these two phases, while the anorthosite remains unreactive. Post-sintering, the MOC has fully decomposed leaving behind some anorthosite peaks, and $Mg(OH)_2$. Additionally, the material has developed a glassy phase as evidenced by the appearance of an amorphous region. This development is not unexpected as LHS-1 is primarily composed of plagioclase feldspars and basaltic glass with melting points ranging from 1200-1400□ [270]. Typically, MOC decomposition would result in a return of the MgO phase, however, it appears that the MgO has been incorporated into the amorphous phase of the material. This is not surprising considering that rapid Mg diffusion into anorthosite glasses has been previously observed at the sintering temperature [271]. The diffusion of Mg into the glass phases of the materials makes the recovery of MgO as a precursor material unlikely. Additionally, the residual $Mg(OH)_2$ has not fully decomposed into MgO and H_2O indicating that all water might not be recoverable. This result is consistent with overall calculations of the mixture composition, as H_2O and Cl make up approximately 26% by mass of the MOC cement, with **Figure 19** showing a max mass-loss of 14%.
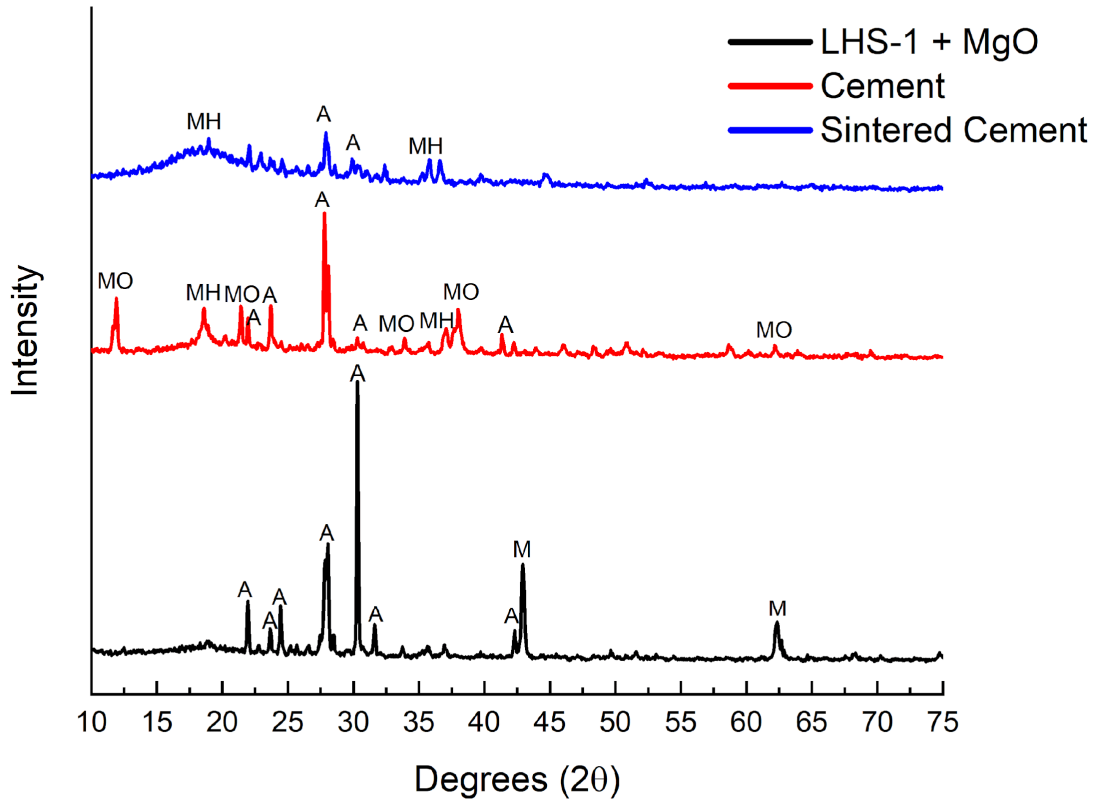
Figure 20: X-ray diffraction of precursor materials, magnesium oxychloride cement, sintered cement. Anorthosite (A), magnesium oxide (M), magnesium hydroxide (MH), and magnesium oxychloride (MO).

3.3 Hardened State Properties

Pre- and post-sintering shrinkage data is shown in **Figure 21a**. Pre-sintering shrinkage is to be expected, as there is some degree of self-desiccation as water evaporates from the binder matrix [272,273]. After seven days of curing at room temperature and humidity the dimensional shrinkage, on average, is under 5%. If needed, this shrinkage could be mitigated by curing samples in a higher humidity environment. Post-sintering shrinkage is based on the percent size reduction in comparison to the original casting mold, therefore it also includes this initial shrinkage induced by self-desiccation. The greatest overall shrinkage occurred in the pore water containing sintered samples where approximately 13% dimensional change was observed. Pre-dried sintered samples exhibited a lower average dimensional change of 8%. Post-sintering

shrinkage was expected to occur both due to the overall mass loss and reductions in pore volume as the quasi-molten material reduces void spaces. Interestingly, the maximum shrinkage was approximately equivalent to the total mass loss observed in **Figure 19**. The proportionality of the mass-loss and shrinkage likely indicates that it is the primary shrinkage mechanism. Although **Figure 21b** shows a clear densification of the cement matrix it does not completely account for all of the shrinkage observed.

Overall, the sintering process reduced the volume of permeable pores in the sintered paste samples. **Figure 21b** shows a decrease in pore volume in both pore solution containing and pre-dried sintered specimens, with a more significant decrease for the pre-dried samples. The higher porosity of the pore solution containing samples was likely due to the cracking induced by flash evaporation of the pore water. However, it is of note that the cracked samples still exhibited approximately a 7% reduction in permeable porosity compared to the unsintered ones, indicating that the process still led to a reduction in pore volume.

Sintering, both pore solution containing, and pre-dried samples led to significant increases in the compressive strength. **Figure 21c** shows that the MOC paste samples, on average, exhibited a compressive strength of approximately 7 MPa, while the pore solution containing and pre-dried sintered samples exhibited average compressive strengths of 15 MPa and 20 MPa, respectively. A higher liquid-to-binder (l/b) ratio (**Table 9)** leads to a MOC cement with a generally low compressive strength due to the increased porosity of the material. The sintering process reduces the overall porosity of the samples (**Figure 21b**), increasing the compressive strength of the material, with the least porous samples having the greatest compressive strength. In addition to reducing the overall porosity, the glassification of the anorthosite and diffusion of the Mg into the system creates a more homogenous matrix than that

of the cementitious binder, leading to increased compressive strength. Lastly, the previously

mentioned cracking of the pore solution containing samples is also likely responsible for the

difference in compressive strength between sintered specimens, as these defects would lead

greater stress concentrations, resulting in failure.
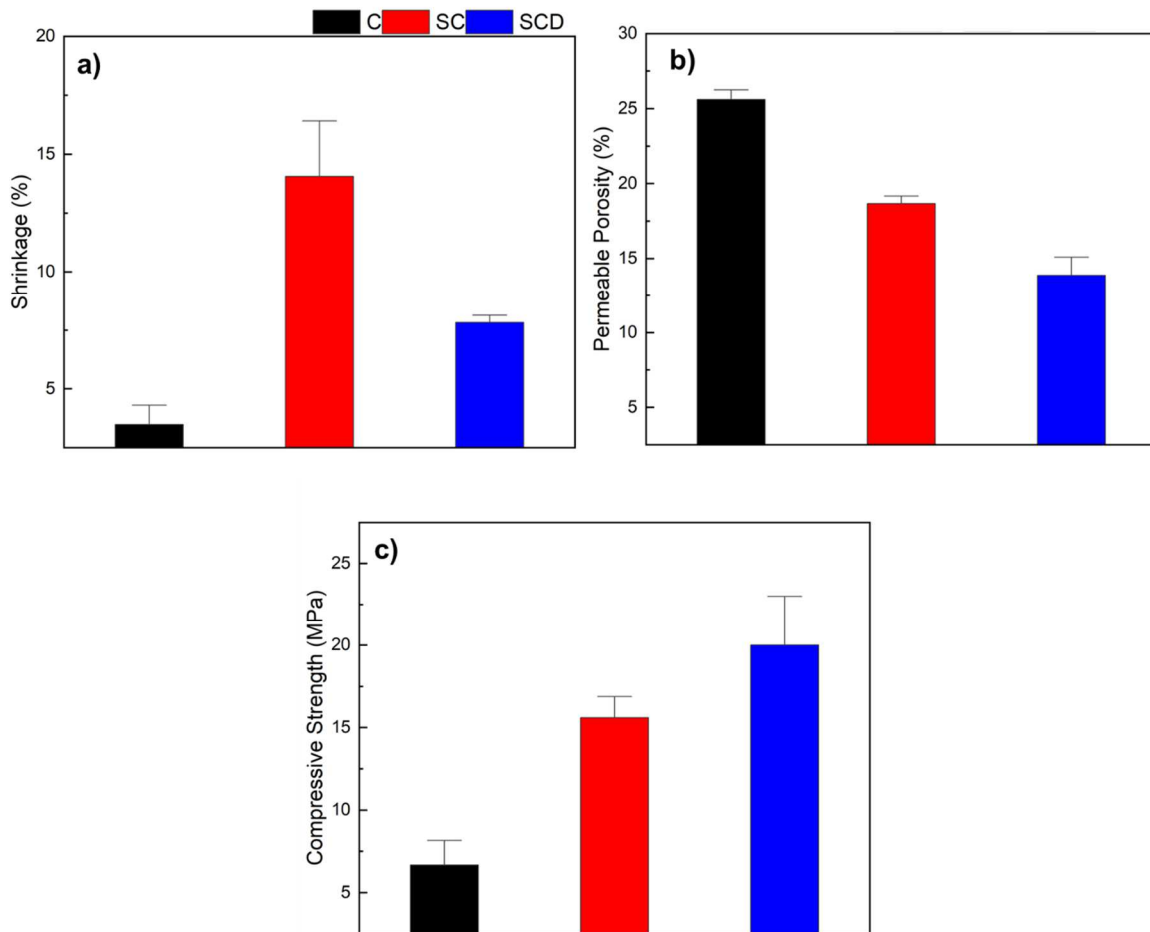
Figure 21: Hardened state properties of MOC cements unsintered (C), sintered (SC), and dried
and sintered (SCD); a) dimensional shrinkage b) permeable porosity and c) compressive
strength.

3.4 Powder Binder Jet Printing

To demonstrate the utility and fidelity of additive manufacturing of lunar regolith MOC

cements, two types of objects were 3D printed using a powder binder jet printing technique

(successive layer-by-layer ink-jet ejection of an aqueous binder solution into the mixture of

LHS-1, $MgCl_2$, and MgO powders). The first printed items were simple rectangular bars (**Figure 22a**) showing that small scale items could be accurately produced. In addition, **Figure 23** depicts

a more complex shape, a concave wrench mold. To obtain these printed parts and to allow them

to develop sufficient strength to be removed from the printer bed and subsequently sintered, an

ink saturation level of 0.51 mL/cm^3 was used, where ink saturation refers to the amount of fluid

deposited per cm^3 of object volume.

Figure 22: Examples of powder binder jet printed bars of simulated lunar regolith MOC cements a) as printed b) after sintering.

Some warping behavior is noticeable in these printed parts (**Figure 22**). This warping is

likely due to the self-desiccation of the material, as well as to the apparent hydrophobicity of the

powder mixture. When droplets impinge on the powder bed, they do not always fully intrude into

and completely wet the material, likely contributing to differential shrinkage. Sintered 3D printed

parts are shown in **Figure 22b** demonstrating that these materials are dimensionally stable, as

expected from their cast counterparts described previously.

In order to demonstrate fabrication of a more detailed design a wrench mold was also 3D printed (**Figure 23**), with reproduction of relatively fine features including the lettering along the length of the wrench (**Figure 23a**). As with the previous samples, some loss of powder and warping of these parts is observed (**Figure 23c**). Future studies could include a more exhaustive optimization of binder saturation levels and surfactant concentrations to improve binder infiltration and address these issues.

Figure 23: Powder binder jet printed wrench mold of simulated lunar regolith MOC cements. a) cross section b) length, and c) width

4.0 Conclusion

This work has demonstrated the feasibility of sintering lunar regolith containing MOC pastes to improve the hardened state properties of the material, and to potentially recover some water invested in its production. Sintering of the regolith MOC pastes leads to full decomposition of the MOC releasing HCl and water which can potentially be captured. Sintered samples exhibit higher compressive strength, reduced permeable porosity, and increased shrinkage. This study also demonstrated that a powder bed 3D printing technique can be used to

produce small-scale, sinterable parts from these regolith cements, potentially useful for lunar manufacturing of a wide range of useful objects.

5.0 Acknowledgements

CHAPTER 7: Development of Regolith-Based Lunar Glasses for the Construction of Lunar Colony

Chapter 7 continues the discussion of ISRU and its applications for the development of a lunar habitat. It provides a proof-of-concept study for the utilization of regolith-based lunar glasses as a structural material. Initially, the study utilizes finite element analysis to demonstrate the feasibility of a lunar glass habitat, and it proceeds to manufacture and characterize glasses made from two types of regolith, doped with varying contents of TiO_2. This chapter will be submitted to *Scientific Reports*.

1.0 Introduction

With a continued focus on space exploration, particularly with upcoming missions to the lunar surface, it behooves us to investigate methodologies to create lunar settlements. Many authors have proposed a variety of materials derived from in-situ resource utilization (ISRU) to develop the lunar landscape ranging from metals, cementitious binders, sintered regolith and more [8,12–14]. Manufacturing all these novel materials requires a variety of precursor materials, energy inputs, or both. This creates a set of tradeoffs that must be considered when creating a lunar settlement. Some examples of this resource demands include 1) the manufacture of cementitious binder which requires, thermal energy and water, 2) the manufacture of metals such as aluminum which require energy, fluids, and chemical additives and 3) sintered regolith parts which require heating. In addition to resource demands, each of these materials must be fabricated onto the lunar surface. Several authors have proposed a variety of additive manufacturing techniques to produce lunar structures ranging from direct ink writing, laser-melting techniques, to powder binder jetting to produce strong reliable structures [12,14,26,33,34]. Not

all these additive manufacturing techniques are suitable for every material, but they would allow for the remote production of facilities with minimal direct human involvement.

Lunar glass was proposed as a building material for lunar structures as early as 1984 [274]. It was lauded as an excellent candidate due to its high compressive strengths and its behavior in anhydrous environments [274]. In a hard vacuum environment, silica glasses exhibit improved mechanical properties as the lack of water in the environment mitigates the hydrolysis of the silica bonds [274]. Water can penetrate silica glass either during the manufacturing process or with exposure to at atmosphere via diffusion mechanisms, water then exists in the glass as molecules or hydroxyl groups [275]. The incorporation of both hydroxyl groups and water molecules leads to Si-O bonds breaking creating a loss of connectivity in the silica network leading to reduced Young's modulus and fracture toughness [275]. This also equates to a loss in compressive strength, a phenomenon that would not be experienced in the hard vacuum environment of the lunar surface due to the absence of water molecules in either the manufacture process or environment leading to a strong durable material. Additionally, glass has the benefit of being manufactured through laser or microwave-based powder-bed 3D-printing technologies, with a potential layer-by-layer approach being demonstrated in **figure 24.**
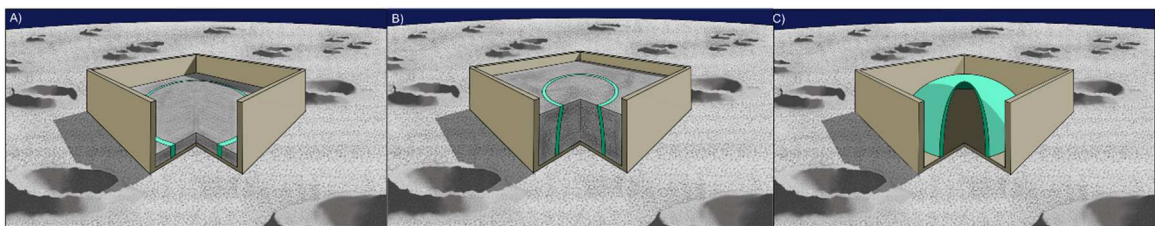
Figure 24: Proposed powder-bed based methodology for the construction of a lunar habitat demonstrating a layer-by-layer approach to the construction of a lunar dome utilizing technologies such as laser or microwave melting.

As previously discussed, many of the materials proposed for the development of a lunar habitat have several energy and precursor requirements to be implemented. **Figure 25** shows some of the steps all materials must undergo before being fabricated. Generally, all materials must be excavated and sorted into useful components via a variety of mechanisms to be transformed into useful feedstocks. This process even applies to materials that will be additively manufactured, as some of the manufacturing techniques (*e.g.,* powder binder jetting) need specific feedstocks to be feasibly implemented. The primary outlier to these processes is either the sintering or melting of lunar regolith. Unlike metals and cements the sintering and melting process simply requires energy to proceed. **Figure 25** shows an example of the energy and material inputs needed for a metal like aluminum compared to glass, and it demonstrates that glass can be feasibly produced after minimal processing. Similar comparisons could be applied to the use of cementitious binders where water, salts, activators, and chemical admixtures are necessary for their successful implementation as structural materials.
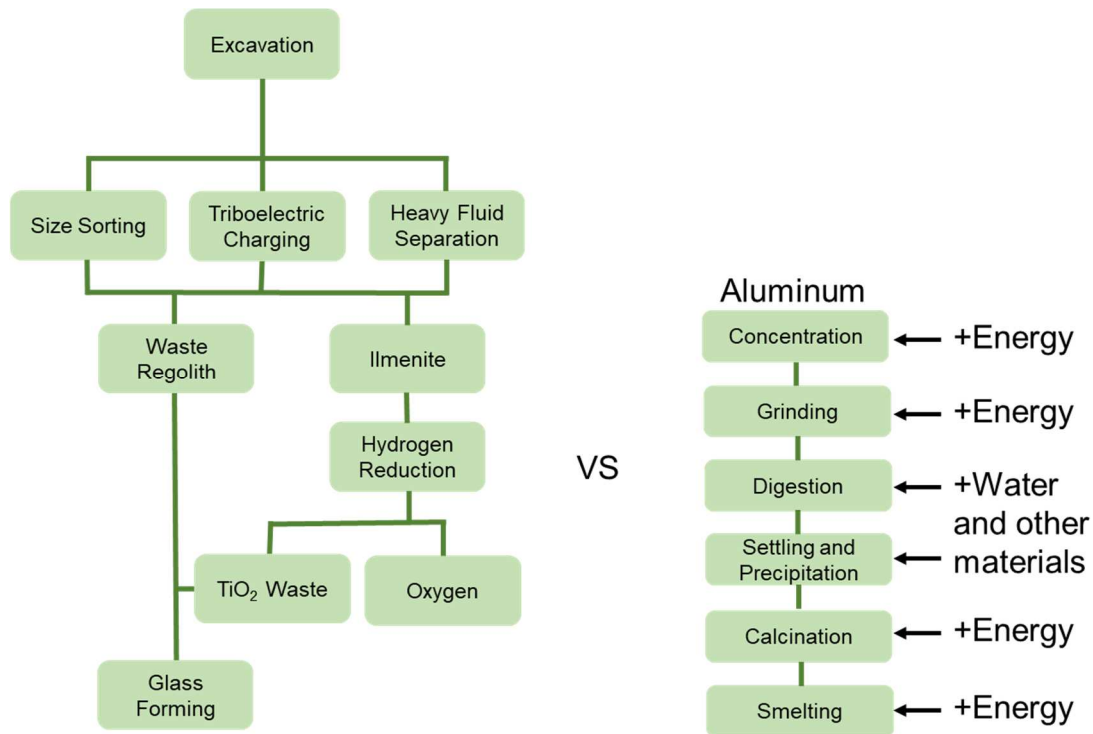
Figure 25: Processing requirements of titania-based lunar regolith glasses compared to processing requirements of a standard metal. Lunar glasses require minimal energy inputs when compared to the manufacturing of structural metals like aluminum, in addition to requiring extra materials for their manufacture.

1.1 Scope of the work

This work seeks to explore the feasibility of lunar-regolith based glasses as structural materials for the development of lunar habitats. This work addresses the manufacture of lunar glass from regolith, the energy requirements to melt lunar regolith, it provides some fundamental finite element analysis of proof-of-concept structures and lastly some initial characterization of simulated lunar regolith glasses.

2.0 Materials and Methods

2.1 Materials

Lunar highland (LHS-1) and lunar mare (LMS-1) simulants were procured from the Exolith Laboratory at the University of Central Florida (Orlando, Florida). The manufacturer provided

elemental composition by weight percent of both simulants can be found in **table 1**. **Figure 26** provides a diffractogram is the TiO_2 powder indicating that it is primarily in the rutile mineral phase.

Table 11: Elemental Composition of LHS-1 & LMS-1 lunar simulants as provided by the manufacturer.

Oxide	SiO₂	Al₂O₃	CaO	MgO	FeO_T	Na₂O	TiO₂	K₂O	SO₃
LHS-1	44.18	26.24	11.62	11.22	3.04	2.30	0.79	0.46	0.10
LMS-1	46.9	12.4	7.0	16.8	8.6	1.7	3.60	0.7	-
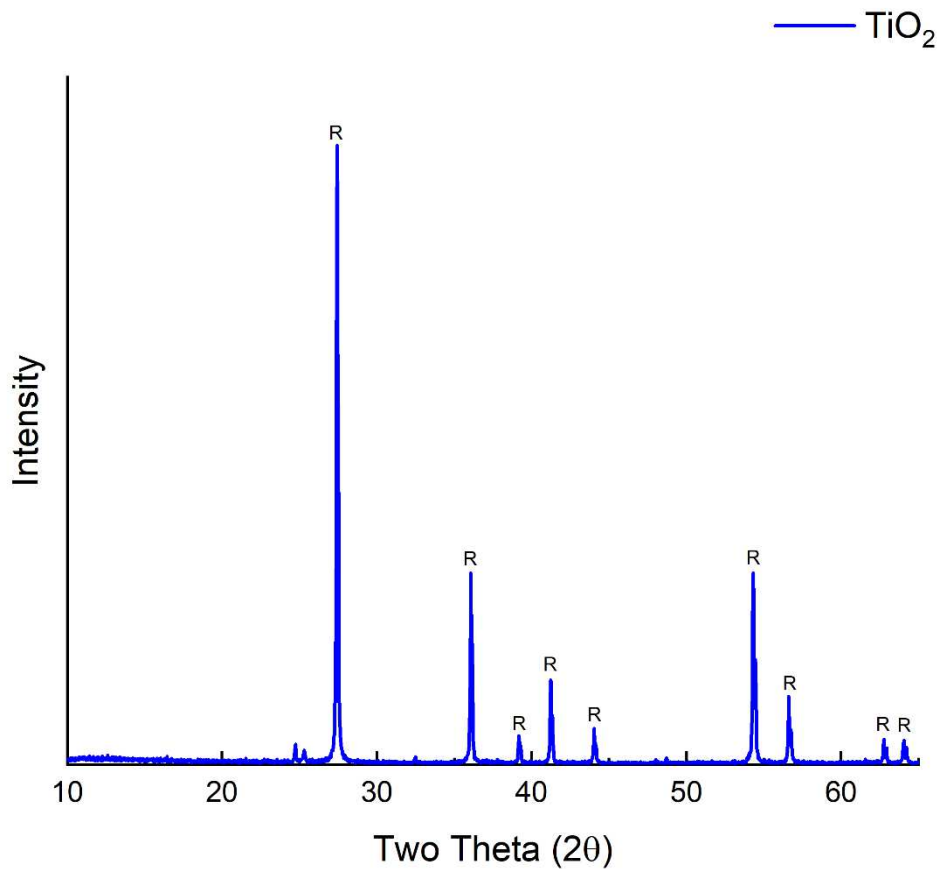
Figure 26: Powdered TiO_2, peaks (R) indicate rutile PDF 004-003-0648.

2.2 Methods

2.2.1 Energy Analysis

To better understand the feasibility of glass structures on the moon, a basic energy analysis was

be performed. The analysis is based on the work of Spedding et al. [276] where the authors have

performed an energy analysis of thermally processed regolith for radiation shielding applications.

The foundational equations are based on the work of Colozza [277] who developed an equation for

the heat capacity of lunar regolith (**Equation 1**). Using the heat capacity equation, we can

determine the amount of heat energy required to melt the lunar regolith at 1600°C (1873.15K).

$$C_{p,Colozza} = -1,848.5 + 1,047.41 \log(T) \left(\frac{J}{kgK} \right) (1)$$

This expression provides the minimum energy input to increase the temperature of the material

up to the melting point, without accounting for thermal losses [276]. This work, like Spedding et al.

assumes a 50% heating efficiency in its analysis, and it provides the energy requirements to melt

1 kg of lunar glass, while briefly discussing some of the means to provide that energy. It is worth

noting that this work does not provide the energy analysis for melting via selective laser

sintering, or other additive manufacturing techniques. This work provides simply provides an

estimate of the total energy cost. Varying manufacturing techniques might have greater or lesser

requirements that should be further studied.

2.2.2 Finite Element Analysis (FEA)

This work seeks to provide a basic FEA analysis of potential glass lunar structure. It utilizes

theoretical values for non-hydrolyzed silicate glasses (**table 12**) as a best guess for material

properties. The work was analysis was performed utilizing ANSYS 2021.

Table 12: Non-hydrolyzed theoretical silica glass properties [275].

Density kg/m^3	Young's Modulus (GPa)	Poisson's Ratio	Tensile Yield Strength (MPa)	Compressive Yield Strength (MPa)	Thermal Conductivity (W/m°C)	Coefficient of Thermal Expansion	Emissivity
2070	60	0.297	152.2	1552	1.38	5.5x10^{-7} /°C	0.93

The FEA analysis is based on the work of Mottaghi et al. and utilizes one types of structure was analyzed [278]. A domed lunar habitat (**figure 27**) was selected because most of the stresses experienced are compressive, leveraging the high compressive strength of glass. Additionally, three-hinged domes are statically determinate. The loading conditions of the lunar habitat are based on the work of Mottaghi et al. [278] and can be seen in **figure 28**. The loading conditions used in our analysis are an internal air pressure of 1.01325×10^5 Pa, a regolith weight per unit area of 8509 Pa, an acceleration of 1.625 m/s^2, and a fixed support at the bottom. The regolith weight per unit area represents regolith-filled sandbags that will be used as shielding for the structure. This shielding will protect the structure from radiation and micrometeoroid impacts. A program-controlled mesh was used with element size set to 0.3 m. This resulted in a total number of 81558 nodes and 61705 elements (consisting of 44271 SOLID187 and 17434 SURF154 elements).
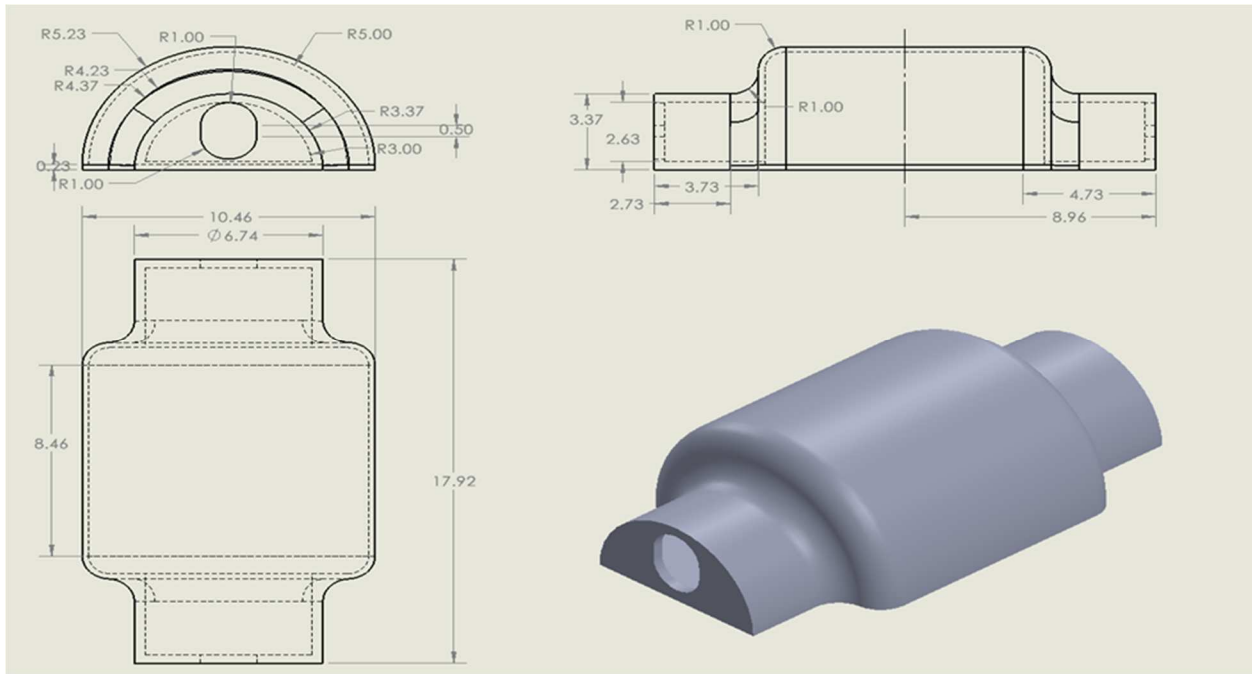
Figure 27: Engineering Drawing and CAD model of lunar habitat based on Mottaghi et al. [278].
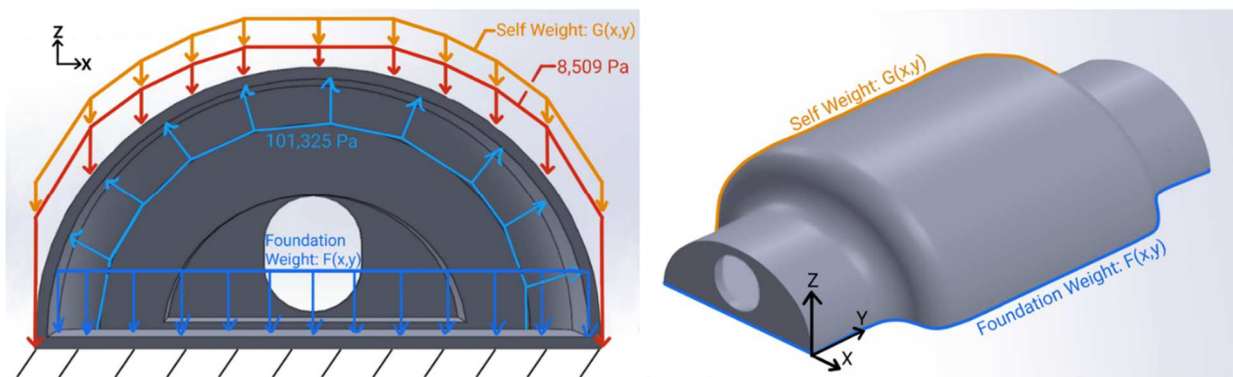
Figure 28: Static loading conditions for the lunar habitat, including internal air pressure, gravity, and radiation shielding.

In addition to analyzing the stresses the structures were subjected to, temperature profiles, their associated thermal stresses and deformations were obtained for the structures to better understand the potential thermal stresses they would be subjected to. For the thermal behavior of our structures, we look at two steady state conditions, lunar noon, and lunar night at the South Pole. We are interested in thermal loads because not every face of our structures will be at the same temperature. This means that some parts of the dome will be expanding while others will

be contracting. We need to make sure that stresses caused by these thermal loads and static loads combined do not cause yielding. The dome structure is on a foundation of sintered regolith. The foundation has thickness of 1 m, length of 25 m, and a width of 15 m. We are using Ansys 2021 R1 "Steady-State Thermal" solver for the simulation. We used a surface-to-ambient radiation condition. The model would need to be very large to use a surface-to-surface condition to model the lunar surface. We use the ambient temperatures found in Mottaghi et al. [278] They use a general heat transfer equation with configuration factors, emissivity factors, and constants to get the ambient temperatures and surface temperatures. We are assuming a constant internal temperature of 23°C with film coefficient of 10 W/m^2°C. **Figure 29a** and **29b** show the thermal conditions for lunar noon and lunar night at the South Pole.
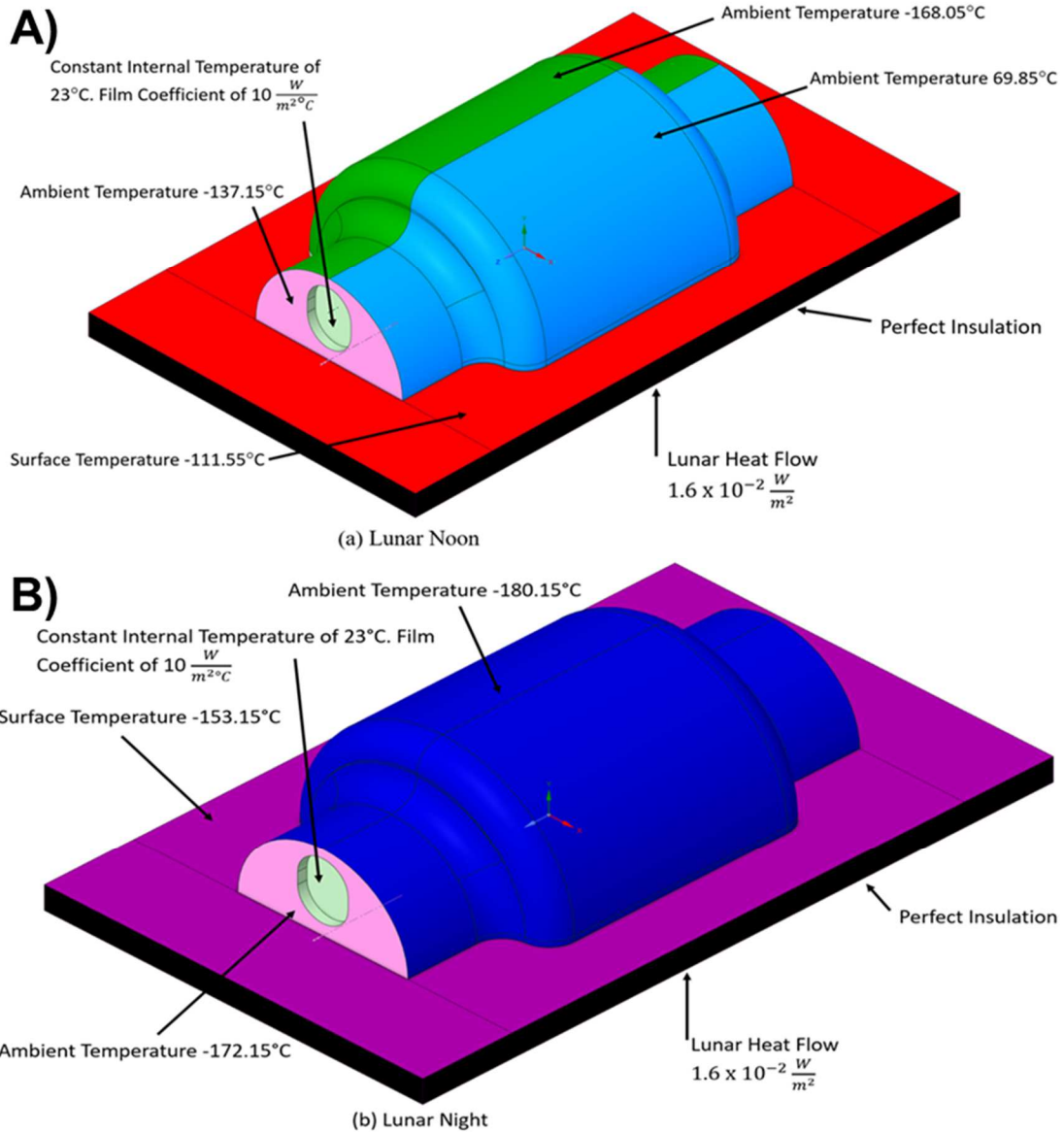
Figure 29: Temperature profiles and analysis conditions for a) Lunar noon and b) Lunar night

We used a program-controlled mesh and we set the element size to 0.4 m. We used these configurations for both the lunar noon and lunar night analysis of the dome. This resulted in a total number of 77596 nodes and 44425 elements (consisting of 20811 SOLID187, 7182 SOLID186, 3192 CONTA174, 3192 TARGE170 and 10048 SURF154 surf elements).

2.2.3 Sample Manufacture

Samples were manufactured utilizing both lunar highland (LHS-1) and mare (LMS-1) simulated lunar regolith along with TiO_2 powder. The powders were blended into a homogenous mixture and placed in zirconia crucibles. **Table 13** provides the composition of each powder mixture.

Table 13: TiO_2 Additions by wt% to LHS-1 and LMS-1

LHS-1	LMS-1
0% TiO_2	0% TiO_2
5% TiO_2	5% TiO_2
10% TiO_2	10% TiO_2
15% TiO_2	15% TiO_2
20% TiO_2	20% TiO_2

The crucibles were heated to 1600□ in an air atmosphere and the mixture was allowed to melt for 3 hours (Furnace, Model DT-31-RS-14-E3504, Deltech, Inc., Denver, CO). After melting samples were furnace cooled overnight, allowing the glass to solidify and anneal. **Figure 30** provides an image of the furnace cooled samples. Samples were extracted from the crucibles utilizing a water-cooled diamond saw and prepared for each characterization test. Thin petrographic sections were prepared for nanoindentation, and SEM/EDS. Thin petrographic sections were initially epoxied to level the surface, subsequently sections were ground in a heavy-duty lap-wheel with 220 grit sandpaper until a flat face was achieved. Afterwards, more epoxy was applied to the surface into a flat finish and the surface was further hand polished with 400 and 600 grit paper. Samples were then glued onto a glass slide, and excess material was removed with a cutoff saw. Subsequently the samples were polished with 220 grit sandpaper on a

heavy-duty lap-wheel until a thickness of 150μm was achieved. After grinding, the sample was hand polished with aluminum oxide powder of varying sizes, starting with 2μm, and finishing with 0.20μm. Final sample thickness is 100μm. Samples were sonicated in a water bath between powder polishing to remove residual powder. Samples were powdered with a mortar and pestle for XRD, HDSC.
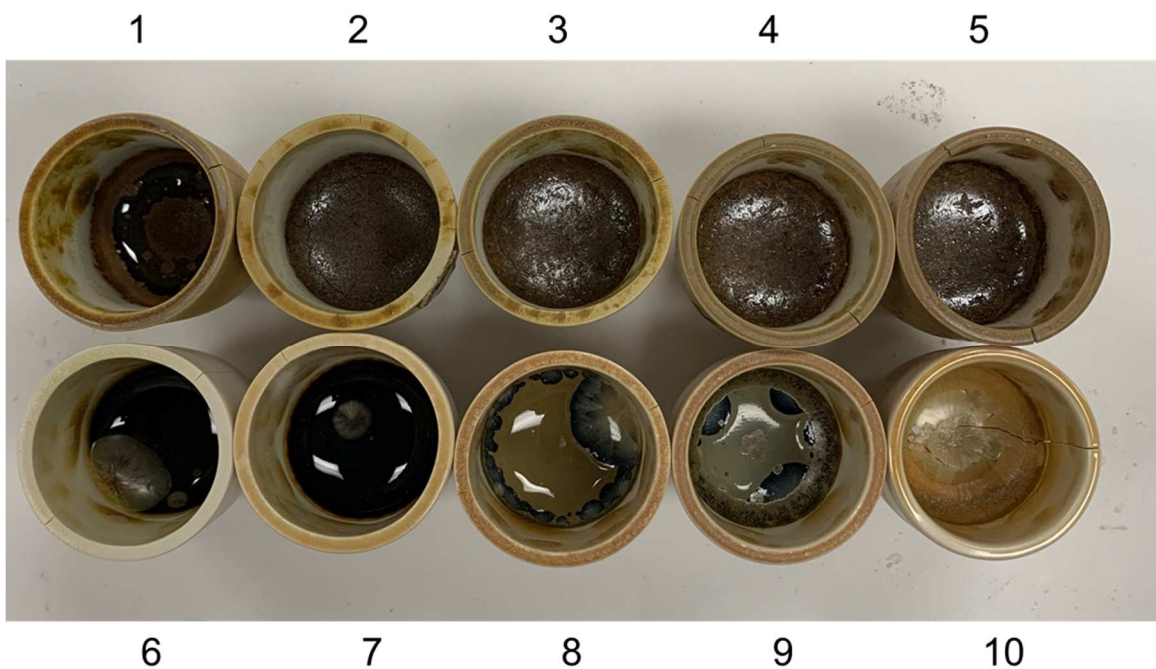
Figure 30: Furnace cooled titania-based lunar regolith glasses with increasing TiO_2 content. Samples 1-5 are LMS-1 while 6-10 are LHS-1. TiO_2 content increases sequentially.

2.2.4 X-ray diffraction

A Rigaku Diffraction System was utilized to obtain diffraction data. Samples were ground with a mortar and pestle and a powder layer was placed on a glass slide coated with petroleum jelly. All samples were analyzed from 15 to 65° 2θ using Cu Kα radiation with a step size of 0.05° and a 2.5 s dwell time per step.

2.2.5 Nanoindentation

Polished petrographic sections were indented with a KLA Tencor iMicro (Milpitas, CA).

Samples were indented in a 10x10 grid with a Berkovich tip until a target load of 5mN was

achieved. Loading was performed in 30 seconds and a dwell time of 20 seconds was applied. The

modulus was calculated using the Oliver Pharr approach, where the 45th-95th percentile of the

unloading curve is fitted with a second order polynomial [279]. Using a known tip modulus and

Poisson's ratio (1140GPa and 0.07 respectively) we calculated the indentation modulus.

2.2.6 Scanning Electron Microscopy and Energy Dispersive Spectroscopy

Using a JEOL-8230 electron microprobe (JEOL, Tokyo, Japan), EDS was utilized to initially

screen zeolites for improved chemical mapping. An acceleration voltage of 20 keV and a beam

current of 20 nA were used to obtain spectra. Samples were coated in platinum to an average

thickness of 10nm.

2.2.7 High Temperature Differential Scanning Calorimetry

Powdered candidate glass specimens were analyzed using Differential Scanning Calorimetry

(DSC, Jupiter, Netzsch, 95000 Selb, Germany), to determine the glass transition temperature

(T_G) and the melting temperature (T_M). Specimen size was approximately 20 mg and the heating

conditions were 20K/min to 1000°C. The data suggested that at least one of the specimens

exhibited phase separation, but that is not anticipated to be an important factor for these glasses

in this application.

2.2.8 Coefficient of Thermal Expansion

Samples extracted from the crucible melts were typically cracked and therefore did not produce

specimens of sufficient quality for dilatometer measurements. To solve this problems, chunks of

glass extracted from the crucibles were ground to a powder using an alumina mortar and pestle

and packed into 6mm x 25mm length cylinders using a small amount of organic binder. These

specimens were sintered at 800°C (above the second T_g) at a heating rate of 10K/min and no

dwelling at peak temperatures producing a relatively high-density sintered specimen for

dilatometer measurements. Thermal expansion was measured using a heating rate of 5K/min

using a dilatometer (Model 1600, Orton, Westerville, OH).

3.0 Results and Discussion

3.1 Finite Element Analysis

The finite element analysis performed on a silica glass lunar habitat yielded acceptable results.

The von-mises stresses for the self-weight, atmospheric pressure, and radiation shielding can be

seen in **figure 31.** The maximum stress is 2.9MPa, significantly lower than the theoretical

maximum tensile stress of 152.2MPa [275]. Although the difference is significant, this does not

account for failure due to fracture, the prevalent failure mechanism in glass. Experimental work

should be conducted to understand the influence of flaws and stress concentrations on the failure

of these structures.
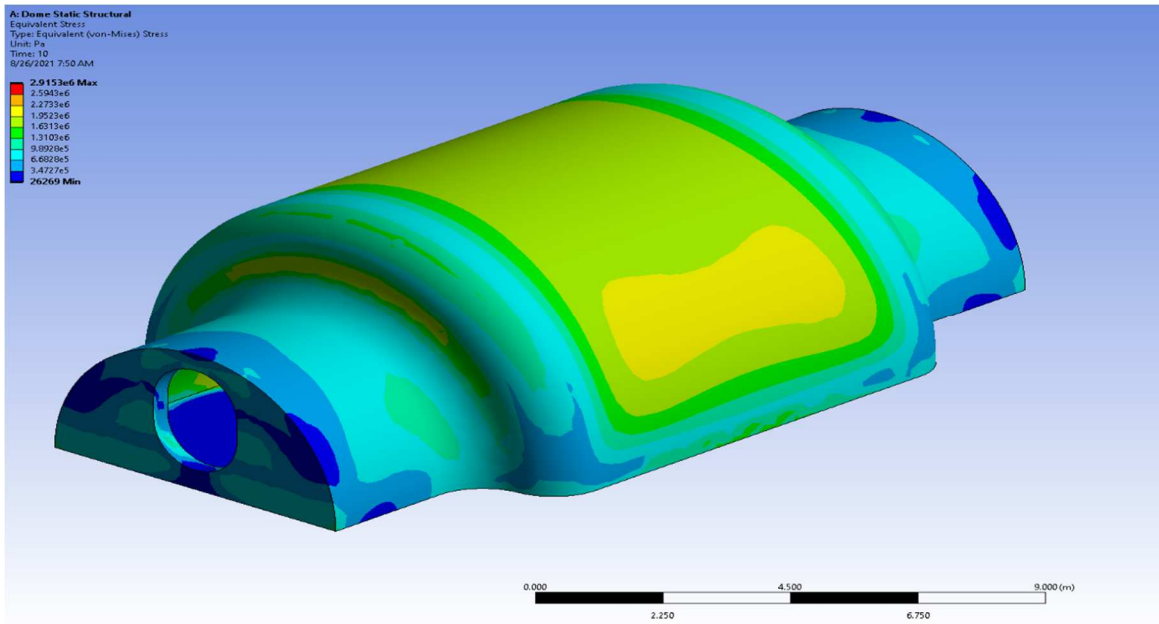
Figure 31: Von-Mises stresses from self-weight, radiation shielding, and atmospheric pressure on a lunar dome.

The results of the thermal analysis are like those of the static loading scenario. Initial temperature profiles for the surface of the materials were determined. **Figure 32 shows** the temperature profiles for lunar noon (**Figure 32a**) and night (**Figure 32b**).
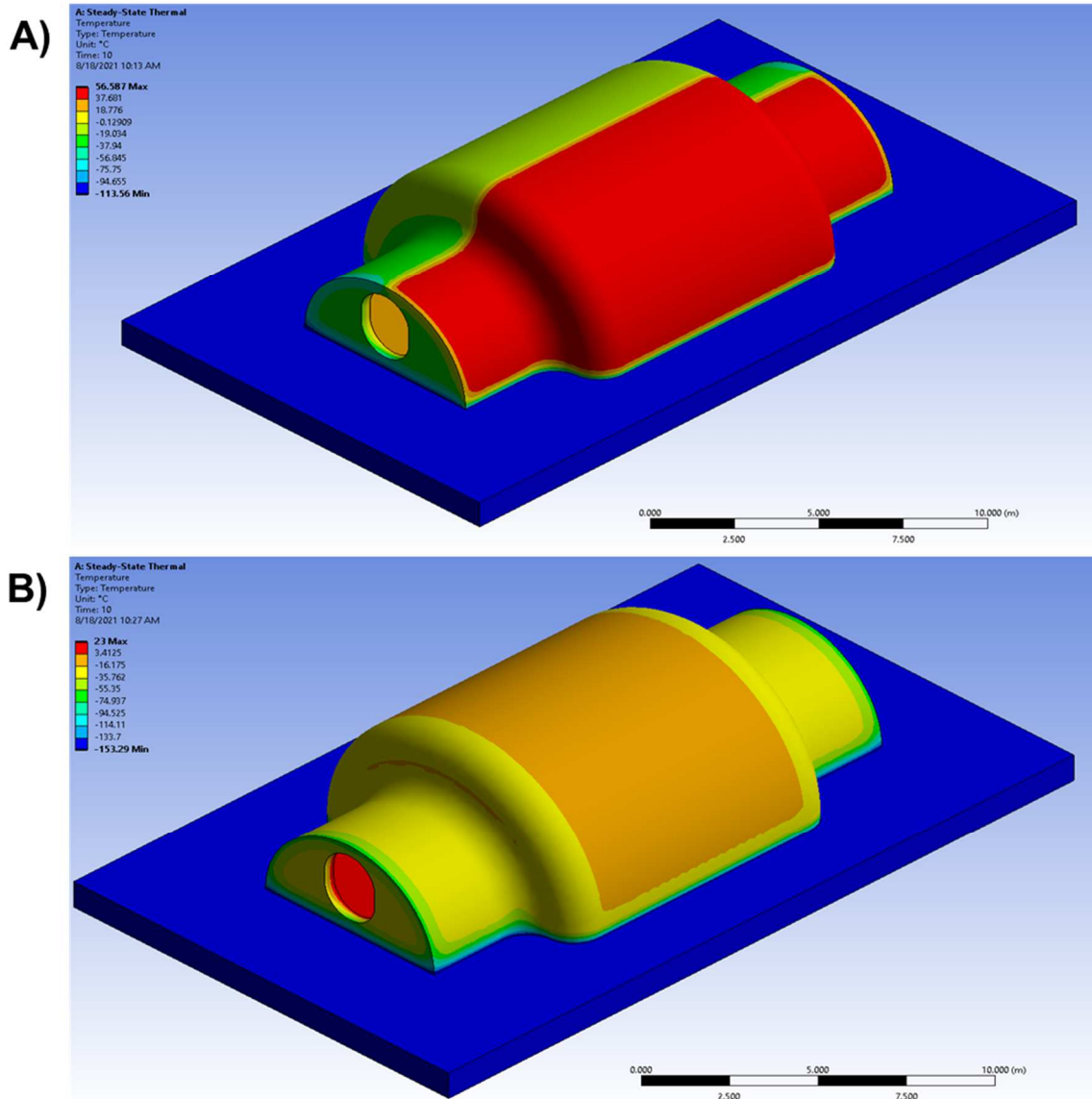
Figure 32: Temperature profiles of a lunar habitat during a) lunar noon b) lunar night.

The analysis for lunar noon shows a temperature ranging from -114°C to 57°C while the analysis

for lunar night shows temperature ranges from -153°C to 23°C. The temperature distribution for

the lunar noon is less uniform than that of the lunar night. The temperature values for the day

cycle match closely with those found in [278], while the values for the night temperatures are

significantly different. This disparity can be attributed to the different thermal properties of silica

glass, compared to the material used in the authors analysis. The thermal stresses induced by

114

these temperatures can be seen in **figure 33** while the deformation due to the stresses can be seen

in **figure 34.**
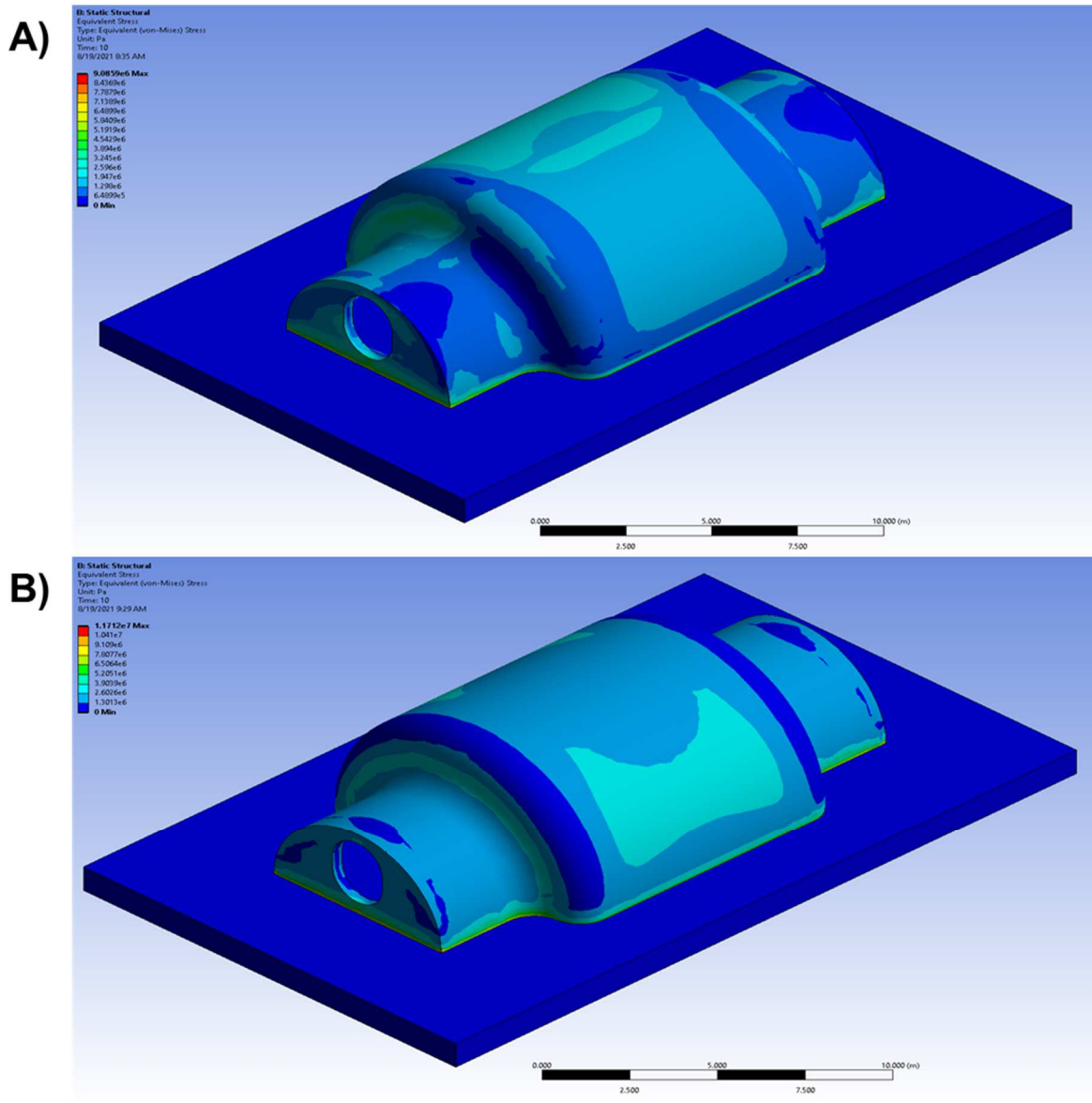
Figure 33: Thermal stresses in a lunar habitat at a) lunar noon b) lunar night

The thermal stresses on the habitat are all under the theoretical maximum tensile stress, ranging

from 10MPa-12MPa during the day-night cycle. These stresses would need to be monitored as

they lead to the expansion and contraction of the glass dome. **Figure 34** shows the preliminary

deflections induced by the thermal stresses.
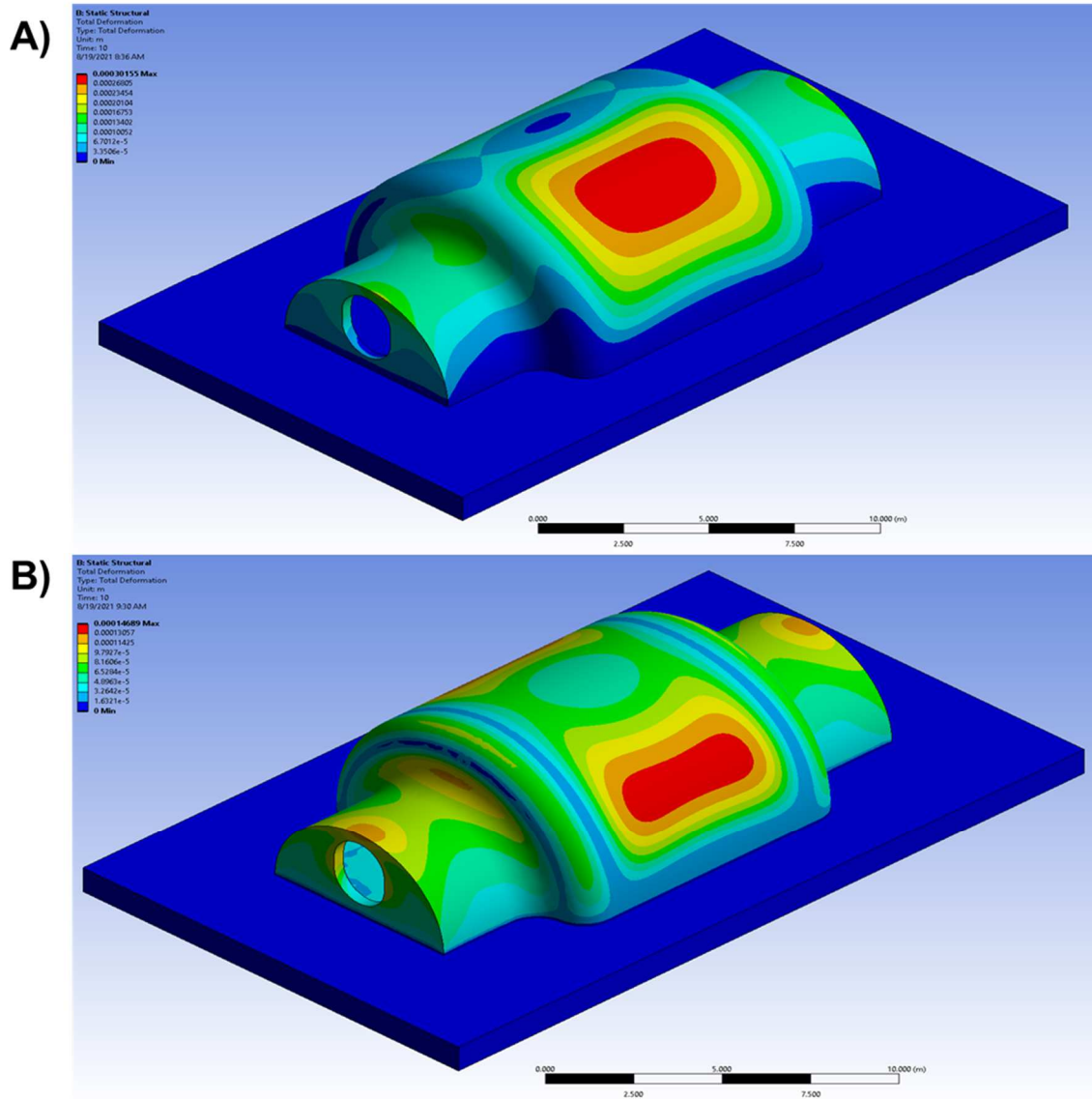
Figure 34: Deformations of a lunar habitat under thermal loading for a) lunar noon b) lunar night.

The greatest deformation is occurring in the middle hinge of the domed structure during both the

lunar day and night.

This analysis was conducted with a theoretical silica glass with a known CTE, Poisson's ratio,

and Young's modulus. The Young's modulus (YM) of the theoretical silica glass is 60GPa,

while the indentation moduli of the simulated lunar regolith glasses range from 100-135GPa.

This disparity on modulus indicates that the glasses are likely to have a greater ultimate tensile

strength than the pure silica glass. It should be noted that for silica glass, YM does not vary greatly within the temperature ranges of -150°C to 120°C. Indicating that our static and thermal analysis should be reliable.

This analysis indicates that a dome produced out of a silica-based glass can meet the minimum demands of an arduous lunar environment. More in-depth FEA work needs to be conducted to understand whether this dome is truly feasible. Work on moonquakes, micrometeoroids, and other conditions needs to be performed to understand the behavior of these domes, and what it means for a structure to withstand all possible loading scenarios. Further FEA work needs to focus on brittle material analysis and should be performed utilizing material properties derived from experimental work. This FEA remains a proof-of-concept study as to the feasibility of lunar glass as a building material.

3.2 Energy Analysis

Integrating equation 1 between 100K to a melting temperature of 1873K a value for energy requirements to melt one kilogram ton of glass is 9.17MJ, if like in Spedding et al. we assume a 50% thermal efficiency, that value doubles to 18.34MJ/kg [276]. The value for simply melting must be compared to the energy demand of other potential building materials. For example, the embodied energy of the aluminum smelting process on earth is approximately 100MJ/kg [280]. This disparity does not account for the energy costs of mining, grinding, refining, and other processes that must be considered. Other metals such as titanium have reported wider ranges for energy consumption during manufacture ranging from 95MJ/kg-361MJ/kg [281]. It is evident that meeting the energy needs to produce some of these metals is unrealistic compared to the production of glass. These numbers make the usage of glass appealing as it will need minimal power infrastructure for successful implementation.

Furthermore, these are the energy costs associated with the *production and manufacture* of both metals and cements. This obviates the associated energy cost, equipment, and processing techniques to transform the material into useable infrastructure. Metals and cements would have to be processed in such a way to be compatible with advanced manufacturing techniques, while glass can be built in-situ from available powder. Selective laser melting, an additive manufacturing technique, would allow for regolith to be transformed into glass without the need for a manufacturing facility [33,34]. Studies have shown that selective laser melting can be utilized to produce complex shapes, while utilizing lasers that require minimal power [33,34] potentially reduces the power demand glass melting.

3.3 Nanoindentation

Figure 11 shows the indentation modulus for LMS-1 samples with TiO_2 additions from 0-20%. The observed moduli are normally distributed with a generally left skew. The addition of TiO_2 seems to be accompanied by a decrease in the median value of the moduli. Samples with 0% TiO_2 addition have an observed median of 135GPa while samples containing TiO_2 in the 5-15% ranges show medians of 125GPa, 111GPa, and 133GPa respectively. Samples containing 20% TiO_2 show a median modulus of 107GPa, demonstrating a sharp decline in modulus. **Figure 35** shows that TiO_2 addition seems to have little to no influence the stiffness of LMS-1 based glasses. This is perhaps due to the formation of identical minerals in all samples. As seen in section 3.4 all LMS-1 samples formed the same mineral compounds indicating that the stiffness should be similar for all the samples.
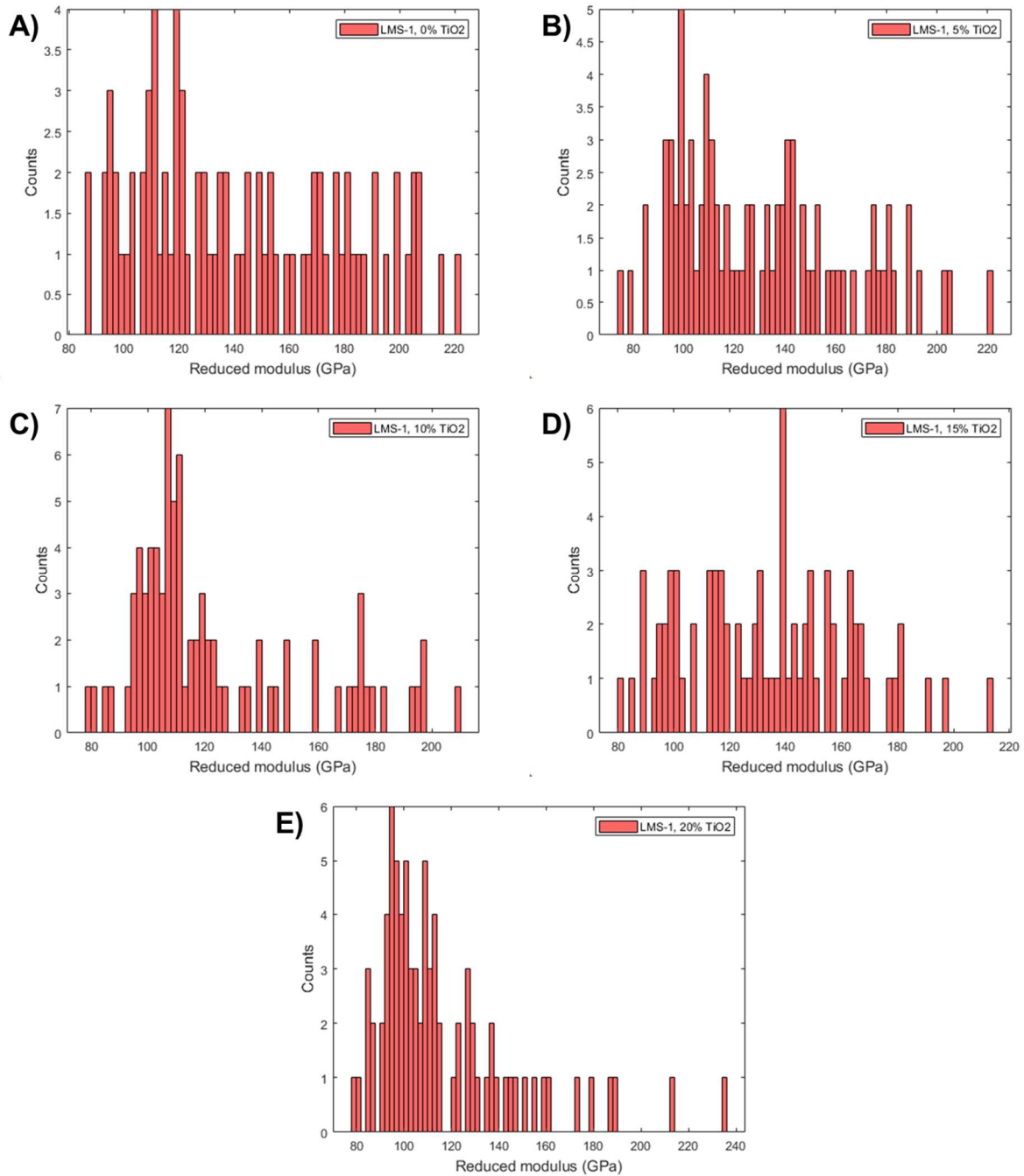
Figure 35: Reduced modulus of LMS-1 lunar glasses with a) 0% TiO$_2$ b) 5% TiO$_2$ c) 10% TiO$_2$ d) 15% TiO$_2$, e) 20% TiO$_2$
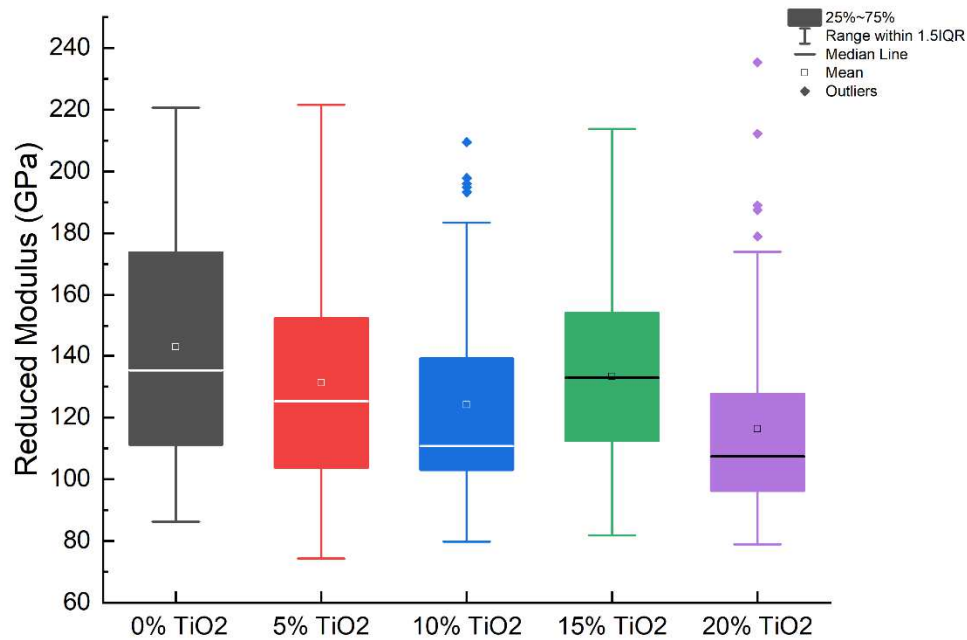
Figure 36: Boxplot comparing distribution of of LMS-1 samples with increasing TiO_2 content. Showing that TiO_2 content has no impact on reduced modulus.

Figure 36 shows the reduced modulus for LHS-1 samples with increasing TiO_2 content. Samples with 0% and 5% TiO_2 addition are normally distributed with no skew while samples with 10-20% TiO_2 are normally distributed with a left skew. Median reduced modulus ranges from 104-110GPa. All samples seem to have similar modulus, but due to the lack of replicates not assertions can be made about their differences. Much like the LMS-1 samples, LHS-1 samples exhibit similar mineralogical composition indicating that their modulus should be like each other as seen on **Figure 37**.
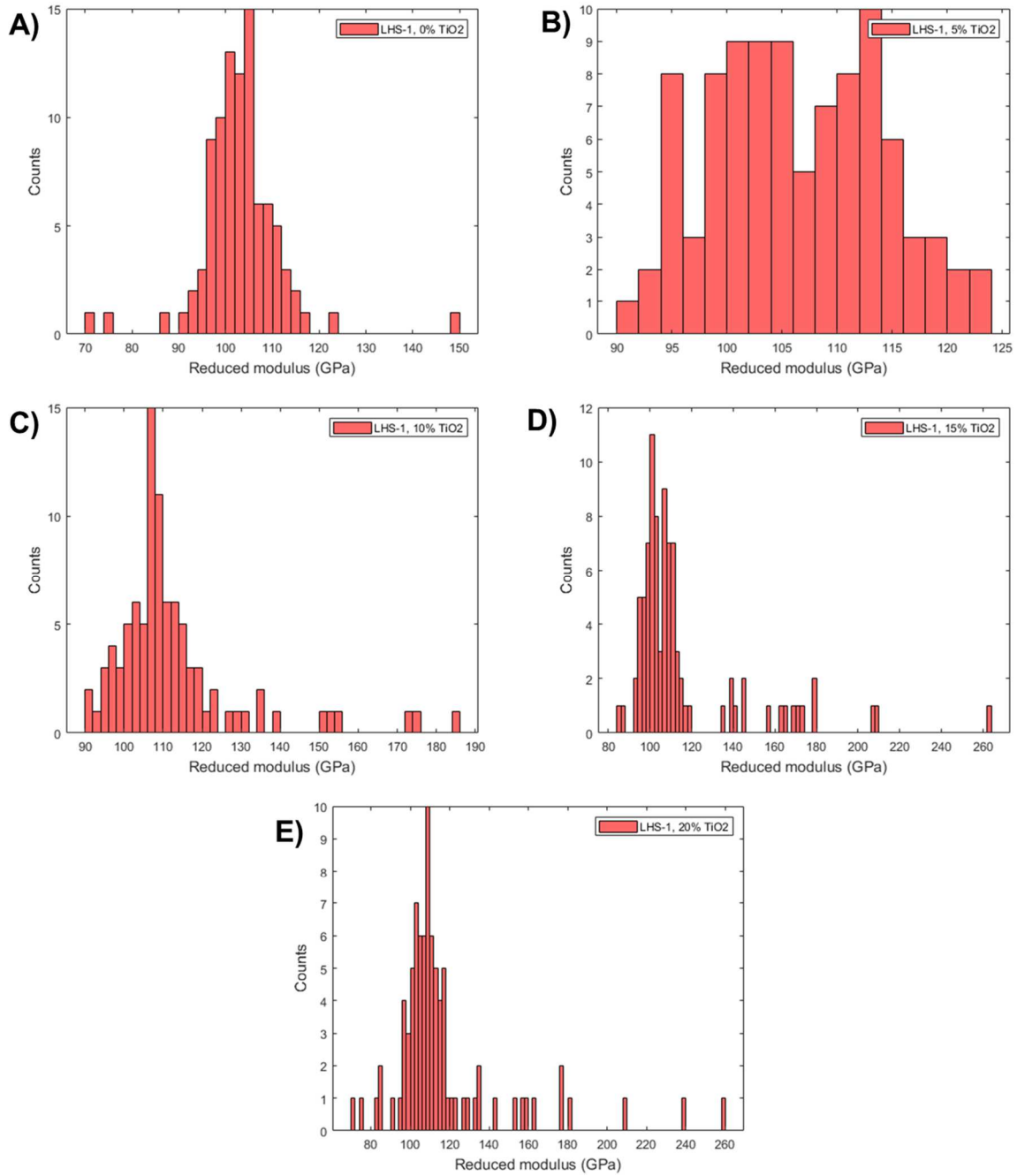
Figure 37: Reduced modulus of LHS-1 lunar glasses with a) 0% TiO_2 b) 5% TiO_2 c) 10% TiO_2 d) 15% TiO_2, e) 20% TiO_2
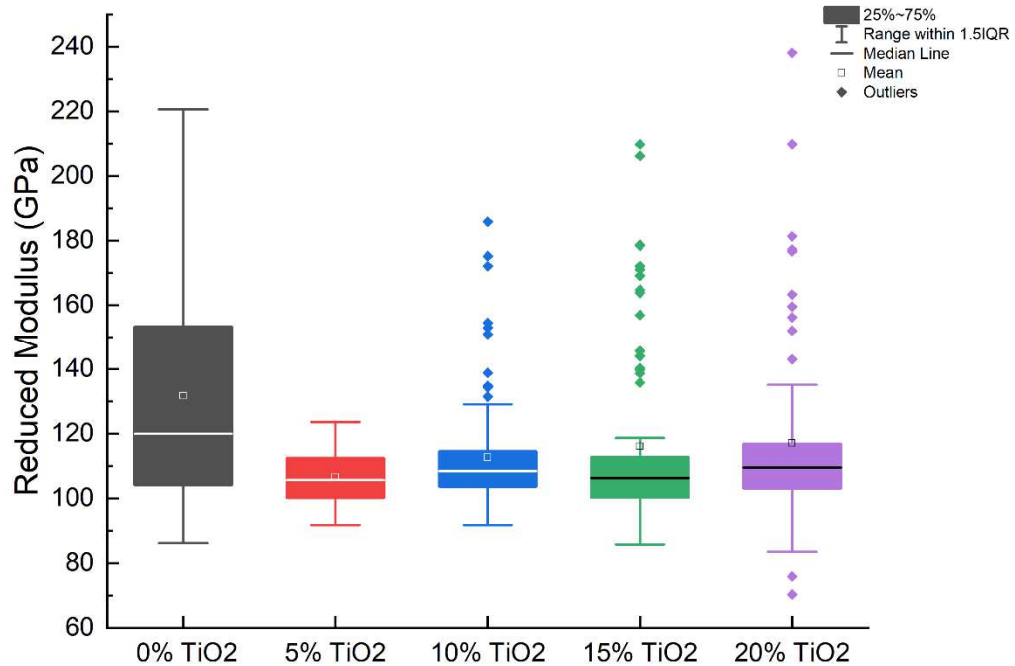
Figure 38: Boxplot comparing distribution of LHS-1 samples with increasing TiO$_2$ content. Showing that TiO$_2$ content has no impact on reduced modulus

Further analysis of both glasses was performed, and the hardness of the material was plotted against the reduced modulus to assess whether the range of observed reduced modulus was produced due to the presence of several phases within the material. **Figure 39** shows the hardness vs. reduced modulus for LMS-1 and LHS-1 glasses. **Figure 39a** shows that for LMS-1 a monotonic increase is observed, meaning that as modulus increases so does hardness. This is the case for glasses with 0% TiO$_2$ and all subsequent mixtures. **Figure 39b** LHS-1 glasses reveal a different picture, with increasing TiO$_2$ content different regions can be observed in the plot. This can mean that on the indented surface different material phases are appearing. This only occurs in samples with TiO$_2$ contents greater than 10%.
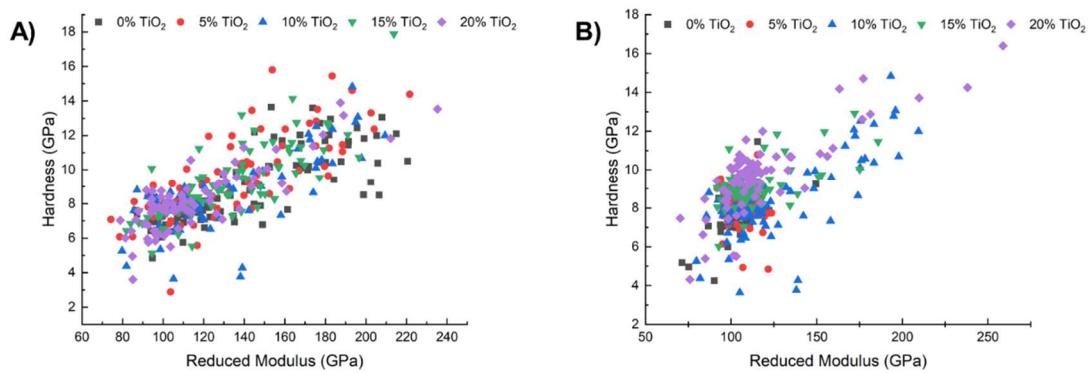
Figure 39: Hardness (GPa) vs. Reduced Modulus (GPa) for A) LMS-1 glasses B) LHS-1 glasses with increasing TiO_2 content

The main takeaways from indentation data are that LMS-1 samples are generally stiffer than their LHS-1 counterparts, at all TiO_2 addition levels LMS-1 samples produced stiffer glasses that could be more suitable for construction. Additionally, the stiffness of all regolith glasses exceeds the stiffness of the theoretical silica glass (60GPa) utilized in the earlier FEA work indicating that these materials exceed the parameters used in our analysis. What does this all mean for lunar construction in terms of mechanical properties? What this data shows is that lunar glasses can provide a single or multiphase material that is suitable for construction. In the case of LHS-1 where multiple phases are found this could provide benefits in terms of fracture toughness, providing different phases to dissipate crack energy, like in a traditional cement where the existence of aggregate mitigates crack propagation. Further research should be done into the fracture mechanics of these glasses.

It is important to note that in construction, the complexity of a material is generally beneficial to increased durability and performance. In cement structures reinforcing steel, and aggregate mitigate some of the pitfalls of pure cement. Although our proof of concept has demonstrated that glass is a viable material – it lacks some of the mechanical benefits of

reinforcing steel and aggregate. Glass structures could be possibly reinforced with basalt fibers, or some other hierarchical complexity to improve their tensile strength, and to mitigate the weaknesses of single-material construction.

This data set is very limited since n=1, therefore no claims can be made about the significance of the measurements beyond the fact LMS-1 and LHS-1 behave differently, with LMS-1 being stiffer.

3.4 SEM, EDS, and XRD

Figure 40 shows selected images of the glass samples containing 0% TiO_2 and 20% TiO_2. Samples with 0% TiO_2 appeared to be smooth and glassy in nature, uniform with no other visible mineral incorporations, EDS shows an even distribution of constituting elements found in LHS-1 and LMS-1 regolith's. As TiO_2 content increased, samples exhibited "stripes" that are distinct from the glassy composition, as seen in **Figure 39**. EDS of these stripes indicate concentrations of titanium, indicating the formation of distinct mineral phases.
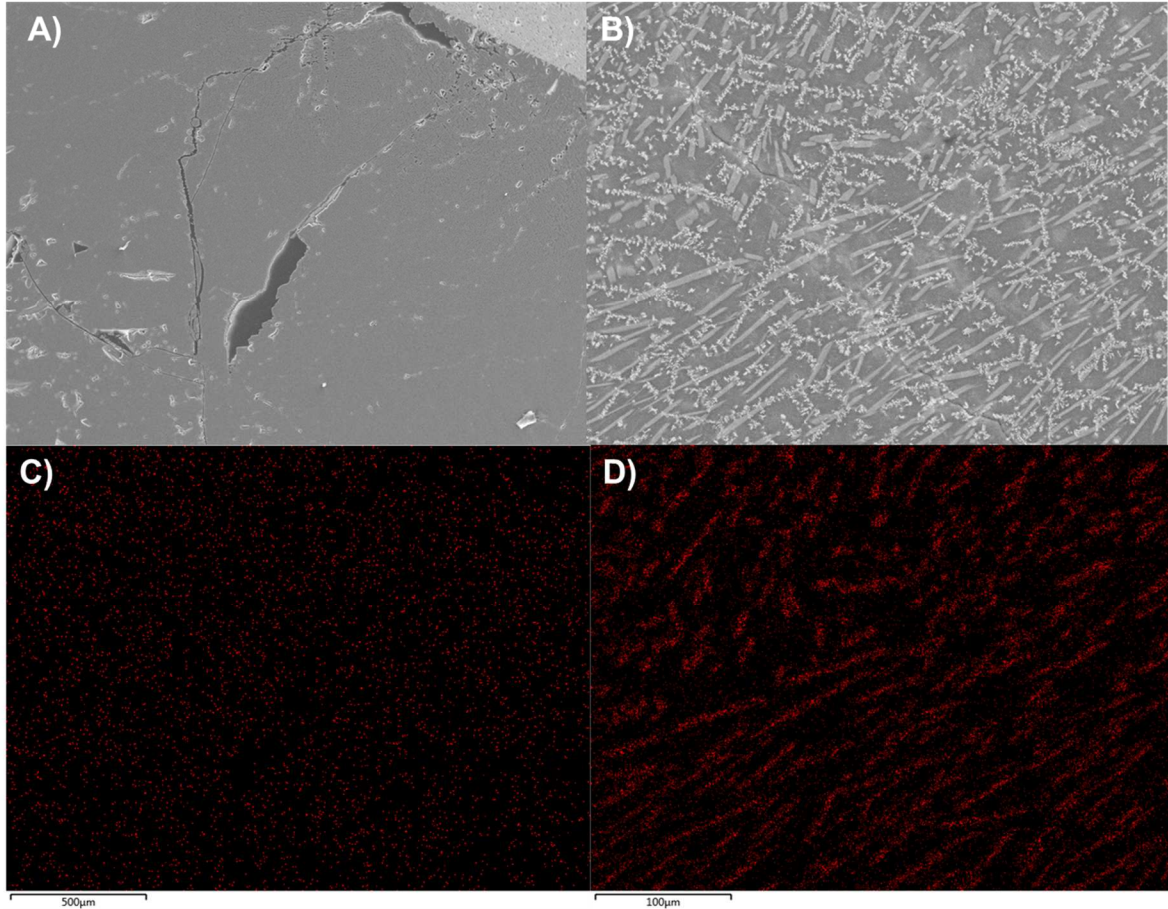
Figure 40: SEM and Ti EDS of lunar glass samples a) SEM MLS-1 0% TiO_2 b) SEM MLS-1 +20% TiO_2 C) MLS-1 0% TiO_2, titanium map D) MLS-1 + 20% TiO_2, titanium map.

X-ray diffraction (**Figure 41**) shows the formation of mineral augite, a titanium containing pyroxene, in the LMS-1 samples. Additionally, these samples exhibit increased formation of ilmenite, a mineral originally found in the simulant. Other minerals found in the sample seem to have become glassy, as they do not show up in the diffraction patterns. Studies have shown that at temperatures above 1000C adding TiO_2 to glass-ceramics containing pyroxene structures lead to the formation of diopside (an end member of the augite solid solution) and to the formation of fayalite [282]. These results can be both observed in all TiO_2 additions to the glasses (**Figure 41**). LHS-1 samples exhibit the presence of titanite, which forms at high temperatures in primarily anorthosite filled mixtures. The presence of titanite begins to occur with the addition of 5% TiO_2

by weight and becomes more pronounced upon further addition. Primarily the TiO_2 containing phases have been analyzed as the role of TiO_2 was elucidated. Further work should be performed on the impact the development of these mineral phases has on the mechanical and thermal properties of these materials. The coefficients of thermal diffusion should be assessed to understand their insulating properties, and the diffusion of oxygen across these minerals should be studied to better understand their suitability for habitat development.
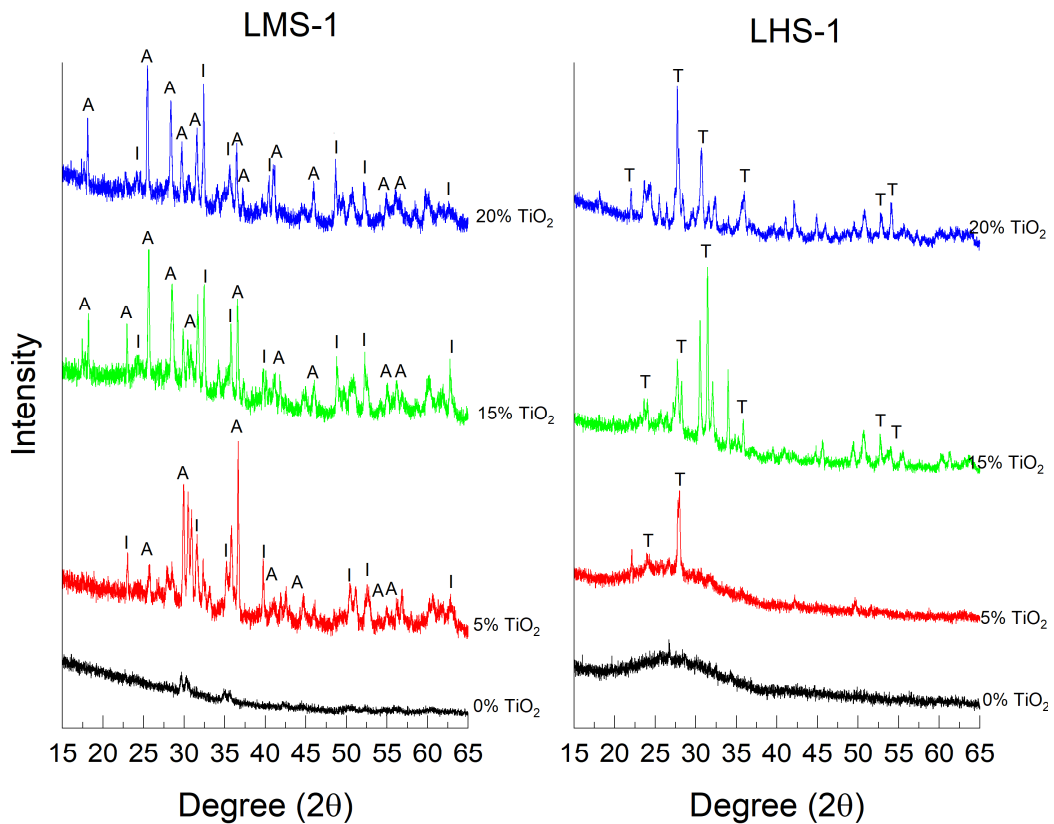
Figure 41: XRD of LHS-1 and LMS-1 glasses. Augite (A), Ilmenite (I), Titanite (T)

3.5 Differential Scanning Calorimetry and Dilatometry

  Figure 42 shows the results of HDSC, indicating that there is an increase in the glass transition temperature of the material when TiO_2 is added into the mixture. The addition of TiO_2

can be utilized to modify the T_g of the lunar regolith glasses, this has been primarily explored in the LMS-1 series and is consistent with the development of new mineral phases upon the addition of TiO_2. LHS-1 glasses have a higher T_g than their LMS-1 counterparts, at 480 °C which is to be expected noting the differing mineralogical compositions of the material. LMS-1 samples have a T_g of 330°C and 337°C with a 20% TiO_2 addition, is due to the development of augite in the material as indicated in **figure 41**. From these glass transition we can determine the optimal annealing temperatures for the various regolith glasses to ensure optimal strength and mechanical properties. This allows for the control of mineral phase formation, and for the tuneability of the material.
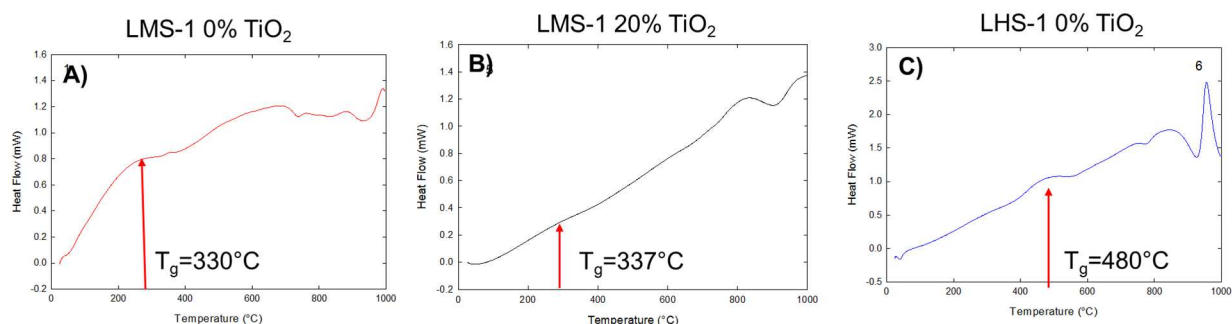
Figure 42: High Temperature Differential Scanning Calorimetry of Lunar Regolith Glasses a) LMS-1, b) LMS-1 +20% TiO_2, and c) LHS-1

Coefficients of thermal expansion (CTE) were obtained via standard dilatometry. Sampling was n=1. Samples were tested to compare the differences in CTE between LHS-1 and LMS-1, and one samples with 20% TiO_2 addition. All samples exhibited CTEs lower than those of common metals such as aluminum as seen in **Table 14.** These coefficients are all in the same order of magnitude, and due to sample restrictions replicate test could not be performed, however, it seems that LMS-1 sample has the highest CTE, while LHS-1 sample is lower and LHS-1 + TiO_2 samples exhibit decreasing CTE, indicating two things: 1) the different composition of mare and highland regolith's will lead to different CTE indicating that further

studies need to be conducted to find an optimal composition and 2) that TiO_2 addition might lower CTE, a beneficial property. This is perhaps a result of the various minerals formed in the melt process. There is a distinct mineral difference between all 3 samples, indicating that these coefficients might be representative. The significance of the CTE is that it is comparable to that of some commercially available metals, and sufficiently close to that of pure silica glass. Further studying the addition of chemical admixtures could further reduce this coefficient minimizing the stresses and deflections caused by thermal fluctuations.

Table 14: Coefficient of Thermal Expansion for Regolith Glasses

LHS-1	LHS-1 +20% TiO_2	LMS-1
6.30×10^{-6}	5.70×10^{-6}	7.48×10^{-6}

4.0 Limitations

The scope of this work is relatively limited due to a variety of constraints. Primarily, this work is limited in terms of the manufacturing technologies utilized to fabricate the regolith glasses. For more accurate data, the glasses should be manufactured in an inert gas or vacuum environment to prevent environmental oxygen from reacting with the melt, leading to the formation of various minerals. Additionally, glasses should be quickly quenched to more accurately reflect the fast-hardening that would be observed with powder-based microwave or laser-based additive manufacturing techniques.

Further research should be performed on the manufacturing process of these materials beyond those provided in this proof-of-concept study. Work should continue in additive manufacturing of regolith melt/glasses as they are the likely candidate to be utilized in space exploration with particular focus on the energy demand, and in-situ monitoring of material

property development. Manufacture in these high temperature processes leads to defects in the structure such as pore formation, that could be monitored in-situ using laser ultrasonics [283].

Research into the bulk-properties of regolith glasses, their strength and durability should be performed to better understand their long-term usage. Understanding the glasses' ability to weather thermal cycles, fatigue, micrometeoroids, moon-quakes and other arduous environments needs to be explored. This proof-of-concept study does not provide sufficient information to utilize glass as a building material, it merely provides a blueprint assessing the feasibility of such and endeavor.

5.0 Conclusion

We have shown that lunar-regolith based glasses are an energetically and structurally viable construction material for the development of lunar habitats. We have calculated the energy cost to produce 1kg of glass via melting is significantly below the energy cost of producing metals such as aluminum and titanium. Via FEA we have shown lunar glass structures can withstand the stresses induced by their self-weight, and by varying day-night cycles. Additionally, we have characterized glasses fabricated out of both simulated Highland and Mare regolith and demonstrated they have comparable properties to traditional silica glass. We have explored the addition of TiO_2 to these lunar glasses and observed the formation of titanium bearing minerals whose effects on mechanical and thermal properties need to be further explored, but that show promising results in reducing the coefficient of thermal expansion and modifying the glass transition temperature of the materials.

6.0 Acknowledgements

CHAPTER 8: Conclusions and Future Work
1.0 Conclusions

Throughout this work I have shown that various processing factors can be utilized to alter the structure of silicious materials to obtain improved performance in arduous environments. I have demonstrated various gaps in the literature, and targeted specific performance problems that lead to the production of resilient materials.

In **chapter 3,** I reviewed existing literature on the chloride diffusivity problem and identified important factors in the processing of alkali activated cements. From there, I identified various mineral phases naturally occurring in alkali activated cements and targeted their unexplored chloride binding potential. In **chapter 4,** I explored the binding potential of zeolitic minerals commonly found in alkali-activated cements and qualitatively found that the minerals can uptake some degree of chlorides, indicating their chloride binding potential in alkali activated cements. In **chapter 5,** I explored the controlled formation of zeolites in alkali activated cements pastes demonstrating the feasibility of the process – from these 3 studies I have drawn several conclusions, highlighted within:

- In **chapter 3**, I concluded zeolites for naturally in alkali-activated metakaolin and fly-ash pastes, mortars, and concretes and their role in chloride transport is not widely understood.

- In **chapter 4**, I concluded that 2 of the commonly formed zeolites in metakaolin alkali activated pastes, faujasite and chabazite, can uptake chloride ions.

- In **chapter 5**, I concluded that with the addition of a SDA we can form target zeolites. These zeolites have the potential to bind chlorides in alkali activated cement concretes, thereby reducing chloride diffusion coefficients.

In the subsequent chapters of the work, I perform studies on in-situ resource utilization, that yielded positive results for space exploration. In **chapter 6**, I explore the use of additive manufacturing techniques to produce sintered ceramics from magnesium oxychloride cements that can be utilize in the development of a lunar colony. In **chapter 7**, I developed a lunar glass that can be utilized to build habitats, and demonstrate its feasibility leading to the following conclusions:

- In **chapter 6**, I concluded that a strong ceramic can be formed from sintered magnesium oxychloride cements, allowing for the recovery of activating materials for subsequent recycling and use in an arduous environment.

- In **chapter 7**, I concluded that regolith-based lunar glasses can be utilized to construct lunar bases. Using finite element analysis, and traditional characterization techniques we demonstrated the development of a proof-of-concept material with sufficient properties for lunar construction.

2.0 Future Work

The work produced in this dissertation illuminates various aspects of the manufacture of silicates for arduous environments, however many questions remain. The following proposed studies are the next steps in advancing the field and filling several knowledge gaps. I plan to pursue some of this work in the next steps of my career.

- The effect of silica-modifying admixtures on slag and fly-ash alkali activated cement pastes: The work in this dissertation contains information with regards to the role of SDA in pure metakaolin systems. In the large body of work of alkali activated cements it is important to study the role of SDA in heterogenous impure systems to determine their efficacy in producing target minerals, and their interaction with the various cations found in these precursors. This study would be like the work in **chapter 5**, but it would utilize a wide range of well characterized available precursors to explore the role of SDAs.

- Physico-mechanical properties of SDA modified metakaolin alkali-activated cement pastes, mortars, and concretes: **Chapter 5** provided a proof-of-concept study to the usage of silica-modifying admixtures in metakaolin based AACs, however it does not study the impact of SDAs on physico-mechanical properties, a crucial factor in cement performance. This study would focus on developing mixes optimized for strength (compressive and tensile), and fracture toughness. Additionally, this study would seek to understand the strain behavior of these cements. The primary variables in this study would be SDA and alkali activator dosage, The formation of zeolites would be monitored via isothermal conduction calorimetry and X-ray diffraction.

- Chloride transport in SDA modified alkali activated cement mortars and concretes: This work would seek to quantify the chloride transport and binding of SDA modified alkali activated cements. This study would scale up the production of SDA modified metakaolin cements into mortar and concrete samples and it would conduct traditional chloride diffusivity and chloride binding ASTM tests to assess the diffusion across the cement matrix when compared to OPC.

- Microwave processing of magnesium oxychloride cements for water, and chlorine recovery: This study would seek to explore microwave sintering as a technique to recover water and chlorine from magnesium oxychloride cements. Microwave sintering is one of the most viable approaches to sintering on the lunar surface, and this study would focus on how important physico-mechanical properties develop based on different variables such as the power of the microwave, the time sintered, etc. Samples would be traditionally manufactured, and an enclosed chamber would be developed to attempt to capture the chlorine gas and water vapor emitted during sintering.

- Vacuum manufacture and testing of simulated-lunar regolith glasses: To better understand the performance of lunar glasses it becomes imperative to develop them in conditions that simulate the arduous environment of space. The presence of oxygen in the atmosphere causes reactions within the molten minerals, and it leads to the precipitation of various mineral compounds within the glass. Characterizing glasses produced in a vacuum will lead to glasses with minerals most like those produced in a lunar environment.

The studies above can all be conducted in a relatively short-term time frame; however, I want to discuss the overarching trends in the processing of silicates for arduous environments. In the cementitious binder world, a need for durable, resilient, low carbon material exists. Therefore, research needs to grow in an area where low-cost, low-dosage chemical modifications increase the durability of materials, and their resistance towards harmful ions, freeze-thaw damage, and other generally detrimental conditions. Modifying the fundamental chemistry of these cements is going to become of paramount importance. These same issues of resilience and durability impact materials derived from in-situ resources. As we have identified sintered or molten materials as energy and resource efficient construction materials on the moon, we need to begin assessing

their durability in the obviously arduous space environment. We need to device tests that simulate space conditions, from heating and cooling cycles to vacuum environments to test whether these structures can exist without the need for drastic short-term repairs. Overall, the processing of silicates for structural applications needs to move towards designing for long-term durability and increased service life in arduous environments by utilizing processing techniques that modify the fundamental structures of the material.

REFERENCES

1. Provis, J. L. Geopolymers and other alkali activated materials: Why, how, and what? *Materials and Structures/Materiaux et Constructions* **47**, 11–25 (2014).

2. Pacheco-Torgal, F., Castro-Gomes, J. & Jalali, S. Alkali-activated binders: A review. Part 1. Historical background, terminology, reaction mechanisms and hydration products. *Construction and Building Materials*. **22,** 1305–1314 (2008).

3. Fernández-Jiménez, A. & Palomo, A. *9 – Chemical durability of geopolymers*. *Geopolymers* (2009).

4. Provis, J. L., Duxson, P., Van Deventer, J. S. J. & Lukey, G. C. The Role of Mathematical Modelling and Gel Chemistry in Advancing Geopolymer Technology. *Chemical Engineering Research and Design* **83**, 853–860 (2005).

5. Provis, J. L., Lukey, G. C. & Van Deventer, J. S. J. Do geopolymers actually contain nanocrystalline zeolites? a reexamination of existing results. *Chemistry of Materials* **17,** 3075–3085 (2005).

6. Gevaudan, J. P., Campbell, K. M., Kane, T. J., Shoemaker, R. K. & Srubar, W. V. Mineralization dynamics of metakaolin-based alkali-activated cements. *Cement and Concrete Research* **94**, 1–12 (2017).

7. Pacheco-Torgal, F., Abdollahnejad, Z., Camões, A. F., Jamshidi, M. & Ding, Y. Durability of alkali-activated binders: A clear advantage over Portland cement or an unproven issue? *Construction and Building Materials* **30** 400–405 (2012).

8. Faierson, E. J. & Logan, K. V. Potential ISRU of Lunar Regolith for Planetary Habitation Applications. in *Moon: Prospective Energy and Material Resources* (ed. Badescu, V.) 201–234 (Springer, 2012).

9. Li, Y. *et al.* In-Situ Water Production by Reducing Ilmenite. in *Moon: Prospective Energy and Material Resources* (ed. Badescu, V.) 189–200 (Springer, 2012).

10. Schwandt, C., Hamilton, J. A., Fray, D. J. & Crawford, I. A. Oxygen from Lunar Regolith. in *Moon: Prospective Energy and Material Resources* (ed. Badescu, V.) 165–187 (Springer, 2012).

11. Schwandt, C., Hamilton, J. A., Fray, D. J. & Crawford, I. A. The production of oxygen and metal from lunar regolith. *Planetary and Space Science* **74**, 49–56 (2012).

12. Cesaretti, G., Dini, E., De Kestelier, X., Colla, V. & Pambaguian, L. Building components for an outpost on the Lunar soil by means of a novel 3D printing technology. *Acta Astronautica* **93**, 430–450 (2014).

13. Davis, G., Montes, C. & Eklund, S. Preparation of lunar regolith based geopolymer cement under heat and vacuum. *Advances in Space Research* **59**, 1872–1885 (2017).

14. Fateri, M. *et al.* Solar Sintering for Lunar Additive Manufacturing. *Journal of Aerospace Engineering* **32,** (2019).

15. Khoshnevis, B. *et al.* Lunar Contour Crafting - A Novel Technique for ISRU-Based Habitat Development. in *43rd AIAA Aerospace Sciences Meeting and Exhibit* (American Institute of Aeronautics and Astronautics).

16. Neves, J. M., Ramanathan, S., Suraneni, P., Grugel, R. & Radlińska, A. Characterization, mechanical properties, and microstructural development of lunar regolith simulant-portland cement blended mixtures. *Construction and Building Materials* **258**, 120315 (2020).

17. Moraes Neves, J., Collins, P. J., Wilkerson, R. P., Grugel, R. N. & Radlińska, A. Microgravity Effect on Microstructural Development of Tri-calcium Silicate (C3S) Paste. *Frontiers in Materials* **6**, (2019).

18. Zhou, S., Yang, Z., Zhang, R., Zhu, X. & Li, F. Preparation and evaluation of geopolymer based on BH-2 lunar regolith simulant under lunar surface temperature and vacuum condition. *Acta Astronautica* **189**, 90–98 (2021).

19. Zhou, S., Lu, C., Zhu, X. & Li, F. Preparation and Characterization of High-Strength Geopolymer Based on BH-1 Lunar Soil Simulant with Low Alkali Content. *Engineering* **7**, 1631–1645 (2021).

20. Zhou, S., Zhu, X., Lu, C. & Li, F. Synthesis and characterization of geopolymer from lunar regolith simulant based on natural volcanic scoria. *Chinese Journal of Aeronautics* **35**, 144–159 (2022).

21. Mills, J. N., Katzarova, M. & Wagner, N. J. Comparison of lunar and Martian regolith simulant-based geopolymer cements formed by alkali-activation for in-situ resource utilization. *Advances in Space Research* **69**, 761–777 (2022).

22. Meurisse, A., Beltzung, J. C., Kolbe, M., Cowley, A. & Sperl, M. Influence of Mineral Composition on Sintering Lunar Regolith. *Journal of Aerospace Engineering* **30**, 04017014 (2017).

23. Meurisse, A., Makaya, A., Willsch, C. & Sperl, M. Solar 3D printing of lunar regolith. *Acta Astronautica* **152**, 800–810 (2018).

24. Indyk, S. J. & Benaroya, H. A structural assessment of unrefined sintered lunar regolith simulant. *Acta Astronautica* **140**, 517–536 (2017).

25. Dou, R. *et al.* Sintering of lunar regolith structures fabricated via digital light processing. *Ceramics International* **45**, 17210–17215 (2019).

26. Taylor, S. L. *et al.* Sintering of micro-trusses created by extrusion-3D-printing of lunar regolith inks. *Acta Astronautica* **143**, 1–8 (2018).

27. Hunt, M., Ducut, A. & Lee, C. Microwave Sintering of Simulated Moon Rock. *Journal of Undergraduate Materials Research* **2**, (2006).

28. Fateri, M. *et al.* Localized Microwave Thermal Posttreatment of Sintered Samples of Lunar Simulant. *Journal of Aerospace Engineering* **32**, 04019051 (2019).

29. Hintze, P., Curran, J. & Back, T. Lunar Surface Stabilization via Sintering or the Use of Heat Cured Polymers. in *47th AIAA Aerospace Sciences Meeting including The New Horizons Forum and Aerospace Exposition* (American Institute of Aeronautics and Astronautics)..

30. Kim, Y.-J., Ryu, B.-H., Woo Jin, H., Lee, J. & Shin, H.-S. Microwave Sintering of Lunar Regolith Simulant for Manufacturing Building Elements. 985–991 (2021).

31. Taylor, L. A. & Meek, T. T. Microwave Sintering of Lunar Soil: Properties, Theory, and Practice. *Journal of Aerospace Engineering* **18**, 188–196 (2005).

32. Zocca, A., Fateri, M., Al-Sabbagh, D. & Günster, J. Investigation of the sintering and melting of JSC-2A lunar regolith simulant. *Ceramics International* (2020).

33. Fateri, M. & Gebhardt, A. Process Parameters Development of Selective Laser Melting of Lunar Regolith for On-Site Manufacturing Applications. *International Journal of Applied Ceramic Technology* **12**, 46–52 (2015).

34. Gerdes, N. *et al.* Selective Laser Melting for processing of regolith in support of a lunar base. *Journal of Laser Applications* **30**, 032018 (2018).

35. Lee, M. *X-Ray Diffraction for Materials Research: From Fundamentals to Applications*. (Apple Academic Press, 2017). doi:10.1201/b19936.

36. Ul-Hamid, A. Introduction. in *A Beginners' Guide to Scanning Electron Microscopy* (ed. Ul-Hamid, A.) 1–14 (Springer International Publishing, 2018)..

37. Osio-Norgaard, J. & Srubar, W. V. Zeolite Adsorption of Chloride from a Synthetic Alkali-Activated Cement Pore Solution. *Materials* **12**, 2019 (2019).

38. Gevaudan, J. P., Caicedo-Ramirez, A., Hernandez, M. T. & Srubar, W. V. Copper and cobalt improve the acid resistance of alkali-activated cements. *Cement and Concrete Research* **115**, 327–338 (2019).

39. Sun, Z. & Vollpracht, A. Isothermal calorimetry and in-situ XRD study of the NaOH activated fly ash, metakaolin and slag. *Cement and Concrete Research* **103**, 110–122 (2018).

40. Romano, R. C. de O., Maciel, M. H., Pileggi, R. G. & Cincotto, M. A. Monitoring of hardening of Portland cement suspensions by vicat test, oscillatory rheometry, and isothermal calorimetry. *Applied Rheology* **27**, (2017).

41. Walling, S. A., Bernal, S. A., Gardner, L. J., Kinoshita, H. & Provis, J. L. Phase Formation and Evolution in Mg(OH) 2 –Zeolite Cements. *Industrial & Engineering Chemistry Research* **57**, 2105–2113 (2018).

42. Frazier, S. D. *et al.* Inhibiting Freeze-Thaw Damage in Cement Paste and Concrete by Mimicking Nature's Antifreeze. *Cell Reports Physical Science* **1**, 100060 (2020).

43. Vahidi, G., Rux, C., Sherk, V. D. & Heveran, C. M. Lacunar-canalicular bone remodeling: Impacts on bone quality and tools for assessment. *Bone* **143**, 115663 (2021).

44. Hardiman, M., Vaughan, T. J. & McCarthy, C. T. A review of key developments and pertinent issues in nanoindentation testing of fibre reinforced plastic microstructures. *Composite Structures* **180**, 782–798 (2017).

45. Aytimur, A., Kocyigit, S. & Uslu, I. Calcia Stabilized Ceria Doped Zirconia Nanocrystalline Ceramic. *Journal of Inorganic and Organometallic Polymers and Materials* **24**, 927–932 (2014).

46. Hayes, A. C., Osio-Norgaard, J., Miller, S., Vance, M. E. & Whiting, G. L. Influence of Powder Type on Aerosol Emissions in Powder-Binder Jetting with Emphasis on Lunar Regolith for In Situ Space Applications. *ACS EST Eng.* **1**, 183–191 (2021).

47. Koch, G. *et al.* International Measures of Prevention , Application , and Economics of Corrosion Technologies Study. *NACE International* 1–3 (2016).

48. Broomfield, J. P. *Corrosion of Steel in Concrete: Understanding, Investigation and Repair, Second Edition*. (CRC Press, 2006).

49. Pacheco-Torgal, F., Castro-Gomes, J. & Jalali, S. Alkali-activated binders: A review. Part 2. About materials and binders manufacture. *Construction and Building Materials* **22**, 1315–1322 (2008).

50. Provis, J. L. Alkali-activated materials. *Cement and Concrete Research* **114**, 40-48 (2018).

51. Struble, L., Kim, E. & Gómez-Zamorano, L. Overview of Geopolymer Cement. in *Geopolymer Binder Systems* 1–10 (ASTM International, 2013).

52. Bernal, S. A. & Provis, J. L. Durability of alkali-activated materials: Progress and perspectives. *Journal of the American Ceramic Society* **97**, 997–1008 (2014).

53. Hossain, M. M., Karim, M. R., Hossain, M. K., Islam, M. N. & Zain, M. F. M. Durability of mortar and concrete containing alkali-activated binder with pozzolans: A review. *Construction and Building Materials* **93,** 95–109 Preprint at (2015).

54. Zhang, J., Shi, C., Zhang, Z. & Ou, Z. Durability of alkali-activated materials in aggressive environments: A review on recent studies. *Construction and Building Materials* **152,** 598–613 (2017).

55. Hooton, R. D., Thomas, M. D. A. & Standish, K. *Prediction of Chloride Penetration in Concrete.* (2001).

56. Bu, Y. & Weiss, J. Saturation of air entrained voids and its implication on the transport of ionic species in concrete. *4th International Conference on the Durability of Concrete Structures* (2014).

57. Lee, N. K. & Lee, H. K. Influence of the slag content on the chloride and sulfuric acid resistances of alkali-activated fly ash/slag paste. *Cement and Concrete Composites* **72**, 168–179 (2016).

58. Monticelli, C. *et al.* A study on the corrosion of reinforcing bars in alkali-activated fly ash mortars under wet and dry exposures to chloride solutions. *Cement and Concrete Research* **87**, 53–63 (2016).

59. Bakharev, T. Resistance of geopolymer materials to acid attack. *Cement and Concrete Research* **35**, 658–670 (2005).

60. Kovalchuk, G., Fernández-Jiménez, A. & Palomo, A. Alkali-activated fly ash: Effect of thermal curing conditions on mechanical and microstructural development – Part II. *Fuel* **86**, 315–322 (2007).

61. Skvára, F., Kopec, L., Smilauer, V. & Bittnar, Z. Material and structural characterization of alkali activated low-calcium brown coal fly ash. *Journal of Hazardous Materials* **168**, 711–720 (2009).

62. Winnefeld, F., Leemann, A., Lucuk, M., Svoboda, P. & Neuroth, M. Assessment of phase formation in alkali activated low and high calcium fly ashes in building materials. *Construction and Building Materials* **24**, 1086–1093 (2010).

63. Ma, Y., Hu, J. & Ye, G. The pore structure and permeability of alkali activated fly ash. *Fuel* **104**, 771–780 (2013).

64. Hlaváček, P., Šmilauer, V., Škvára, F., Kopecký, L. & Šulc, R. Inorganic foams made from alkali-activated fly ash: Mechanical, chemical and physical properties. *Journal of the European Ceramic Society* **35**, 703–709 (2015).

65. Roy, D. M., Jiang, W. & Silsbee, M. R. Chloride diffusion in ordinary, blended, and alkali-activated cement pastes and its relation to other properties. *Cement and Concrete Research* **30**, 1879–1884 (2000).

66. Collins, F. & Sanjayan, J. G. Effect of pore size distribution on drying shrinkage of alkali-activated slag concrete. *Cement and Concrete Research* **30**, 1401–1406 (2000).

67. Melo Neto, A. A., Cincotto, M. A. & Repette, W. Drying and autogenous shrinkage of pastes and mortars with activated slag cement. *Cement and Concrete Research* **38**, 565–574 (2008).

68. Ben Haha, M., Le Saout, G., Winnefeld, F. & Lothenbach, B. Influence of activator type on hydration kinetics, hydrate assemblage and microstructural development of alkali activated blast-furnace slags. *Cement and Concrete Research* **41**, 301–310 (2011).

69. Haha, M. Ben, Lothenbach, B., Saout, G. Le & Winnefeld, F. Cement and Concrete Research In fl uence of slag chemistry on the hydration of alkali-activated blast-furnace slag — Part I : Effect of MgO. *Cement and Concrete Research* **41**, 955–963 (2011).

70. Puertas, F. *et al.* A model for the C-A-S-H gel formed in alkali-activated slag cements. *Journal of the European Ceramic Society* **31**, 2043–2056 (2011).

71. Ye, H., Cartwright, C., Rajabipour, F. & Radlińska, A. Understanding the drying shrinkage performance of alkali-activated slag mortars. *Cement and Concrete Composites* **76**, 13–24 (2017).

72. Ortega, E. A., Cheeseman, C., Knight, J. & Loizidou, M. Properties of alkali-activated clinoptilolite. *Cement and Concrete Research* **30**, 1641–1646 (2000).

73. Duxson, P. *et al.* Understanding the relationship between geopolymer composition, microstructure and mechanical properties. *Colloids and Surfaces A: Physicochemical and Engineering Aspects* **269**, 47–58 (2005).

74. Pan, Z., Li, D., Yu, J. & Yang, N. Properties and microstructure of the hardened alkali-activated red mud-slag cementitious material. *Cement and Concrete Research* **33**, 1437–1441 (2003).

75. Lloyd, R. R., Provis, J. L. & van Deventer, J. S. J. Pore solution composition and alkali diffusion in inorganic polymer cement. *Cement and Concrete Research* **40**, 1386–1392 (2010).

76. Zhang, Z., Yao, X. & Zhu, H. Potential application of geopolymers as protection coatings for marine concreteII. Microstructure and anticorrosion mechanism. *Applied Clay Science* **49**, 7–12 (2010).

77. Provis, J. L., Myers, R. J., White, C. E., Rose, V. & van Deventer, J. S. J. X-ray microtomography shows pore structure and tortuosity in alkali-activated binders. *Cement and Concrete Research* **42**, 855–864 (2012).

78. Zhu, H., Zhang, Z., Zhu, Y. & Tian, L. Durability of alkali-activated fly ash concrete: Chloride penetration in pastes and mortars. *Construction and Building Materials* **65**, 51–59 (2014).

79. Ismail, I. *et al.* Modification of phase evolution in alkali-activated blast furnace slag by the incorporation of fly ash. *Cement and Concrete Composites* **45**, 125–135 (2014).

80. Yang, T., Yao, X. & Zhang, Z. Quantification of chloride diffusion in fly ash-slag-based geopolymers by X-ray fluorescence (XRF). *Construction and Building Materials* **69**, 109–115 (2014).

81. Yao, X., Yang, T. & Zhang, Z. Compressive strength development and shrinkage of alkali-activated fly ash–slag blends associated with efflorescence. *Materials and Structures/Materiaux et Constructions* **49**, 2907–2918 (2016).

82. Noor-ul-Amin, Nawab, L. & Ghani, U. Synthesis and characterization of chloride resistant cement from industrial waste through geopolymerization. *Journal of Cleaner Production* **156**, 577–580 (2017).

83. Long, W., Xiao, B., Zhou, B. & Liang, P. Research on the internal pores in alkali-activated slag cementing material via X-CT three-dimensional imaging microscopy. in *AIP Conference Proceedings* vol. 1794 (2017).

84. Ren, D. *et al.* Durability performances of wollastonite, tremolite and basalt fiber-reinforced metakaolin geopolymer composites under sulfate and chloride attack. *Construction and Building Materials* **134**, 56–66 (2017).

85. Miranda, J. M., Fernández-Jiménez, A., González, J. A. & Palomo, A. Corrosion resistance in activated fly ash mortars. *Cement and Concrete Research* **35**, 1210–1217 (2005).

86. Criado, M., Bastidas, D. M., Fajardo, S., Fernández-Jiménez, A. & Bastidas, J. M. Corrosion behaviour of a new low-nickel stainless steel embedded in activated fly ash mortars. *Cement and Concrete Composites* **33**, 644–652 (2011).

87. Asprogerakas, Aristeidis Koutelia, Aristea Kakali, Glykeria Tsivilis, S. Durability of Fly Ash Geopolymer Mortars in Corrosive Environments, Compared to that of Cement Mortars. *Advances in Science and Technology* **92**, 84–89 (2014).

88. Monticelli, C. *et al.* Corrosion behavior of steel in alkali-activated fly ash mortars in the light of their microstructural, mechanical and chemical characterization. *Cement and Concrete Research* **80**, 60–68 (2016).

89. Shi, C. Strength, pore structure and permeability of alkali-activated slag mortars. *Cement and Concrete Research* **12**, 1789-1799 (1996).

90. Brough, A. R. & Atkinson, A. Sodium silicate-based, alkali-activated slag mortars - Part I. Strength, hydration and microstructure. *Cement and Concrete Research* **32**, 865–879 (2002).

91. Zuda, L., Bayer, P., Rovnaník, P. & Černý, R. Mechanical and hydric properties of alkali-activated aluminosilicate composite with electrical porcelain aggregates. *Cement and Concrete Composites* **30**, 266–273 (2008).

92. Aydin, S. & Baradan, B. Mechanical and microstructural properties of heat cured alkali-activated slag mortars. *Materials and Design* **35**, 374–383 (2012).

93. Palomo, A. *et al.* Chemical stability of cementitious materials based on metakaolin. *Cement and Concrete Research* **29**, 997–1004 (1999).

94. Chi, M. & Huang, R. Binding mechanism and properties of alkali-activated fly ash/slag mortars. *Construction and Building Materials* **40**, 291–298 (2013).

95. Ismail, I. *et al.* Influence of fly ash on the water and chloride permeability of alkali-activated slag mortars and concretes. *Construction and Building Materials* **48**, 1187–1201 (2013).

96. Karim, M. R., Hossain, M. M., Zain, M. F. M., Jamil, M. & Lai, F. C. Durability properties of a non-cement binder made up of pozzolans with sodium hydroxide. *Construction and Building Materials* **138**, 174–184 (2017).

97. Arham, A. & Sc, A. M. Strength and Durability Properties of Alkali Activated Slag and Fly Ash-Based Geopolymer Concrete. (RMIT University, 2009).

98. Kupwade-Patil, K. & Allouche, E. N. Examination of Chloride-Induced Corrosion in Reindorced Geopolymer Concretes. *JOURNAL OF MATERIALS IN CIVIL ENGINEERING* **25**, (2013).

99. Chindaprasirt, P. & Chalee, W. Effect of sodium hydroxide concentration on chloride penetration and steel corrosion of fly ash-based geopolymer concrete under marine site. *Construction and Building Materials* **63**, 303–310 (2014).

100. Law, D. W., Adam, A. A., Molyneaux, T. K., Patnaikuni, I. & Wardhono, A. Long term durability properties of class F fly ash geopolymer concrete. *Materials and Structures* 1–11 (2014).

101. Gunasekara, C., Law, D. W. & Setunge, S. Long term permeation properties of different fly ash geopolymer concretes. *Construction and Building Materials* **124**, 352–362 (2016).

102. Nuaklong, P., Sata, V. & Chindaprasirt, P. Influence of recycled aggregate on fly ash geopolymer concrete properties. *Journal of Cleaner Production* **112**, 2300–2307 (2016).

103. Gunasekara, Chamila Bhuiyan, Shamir Law, David Setunge, Sujeeva Ward, L. Corrosion Resistance in Different Fly Ash Based Geopolymer Concretes. *HPC/CIC Tromsø 2017* (2017).

104. Al-Otaibi, S. Durability of concrete incorporating GGBS activated by water-glass. *Construction and Building Materials* **22**, 2059–2067 (2008).

105. Lim, N. G., Jeong, S. W., Her, J. W. & Ann, K. Y. Properties of cement-free concrete cast by finely grained nanoslag with the NaOH-based alkali activator. *Construction and Building Materials* **35**, 557–563 (2012).

106. Chi, M. Effects of dosage of alkali-activated solution and curing conditions on the properties and durability of alkali-activated slag concrete. *Construction and Building Materials* **35**, 240–245 (2012).

107. Law, D. W., Adam, A. A., Molyneaux, T. K. & Patnaikuni, I. Durability assessment of alkali activated slag (AAS) concrete. *Materials and Structures* **45**, 1425–1437 (2012).

108. Ravikumar, D. & Neithalath, N. Electrically induced chloride ion transport in alkali activated slag concretes and the influence of microstructure. *Cement and Concrete Research* **47**, 31–42 (2013).

109. Ma, Q., Nanukuttan, S. V., Basheer, P. A. M., Bai, Y. & Yang, C. Chloride transport and the resulting corrosion of steel bars in alkali activated slag concretes. *Materials and Structures* **49**, 3663–3677 (2016).

110. Balcikanli, M. & Ozbay, E. Optimum design of alkali activated slag concretes for the low oxygen/chloride ion permeability and thermal conductivity. *Composites Part B: Engineering* **91**, 243–256 (2016).

111. Parthiban, K. & Saravana Raja Mohan, K. Influence of recycled concrete aggregates on the engineering and durability properties of alkali activated slag concrete. *Construction and Building Materials* **133**, 65–72 (2017).

112. Behfarnia, K. & Rostami, M. Effects of micro and nanoparticles of SiO2on the permeability of alkali activated slag concrete. *Construction and Building Materials* **131**, 205–213 (2017).

113. Bondar, D., Lynsdale, C. J., Milestone, N. B. & Hassani, N. Oxygen and chloride permeability of alkali-activated natural pozzolan concrete. *ACI Materials Journal* **109**, 53–61 (2012).

114. Bernal, S. A., Mejía De Gutiérrez, R. & Provis, J. L. Engineering and durability properties of concretes based on alkali-activated granulated blast furnace slag/metakaolin blends. *Construction and Building Materials* **33**, 99–108 (2012).

115. Bernal, S. A., Provis, J. L., Mejía de Gutiérrez, R. & van Deventer, J. S. J. Accelerated carbonation testing of alkali-activated slag/metakaolin blended concretes: effect of exposure conditions. *Materials and Structures* **48**, 653–669 (2015).

116. Albitar, M., Mohamed Ali, M. S., Visintin, P. & Drechsler, M. Durability evaluation of geopolymer and conventional concretes. *Construction and Building Materials* **136**, 374–385 (2017).

117. Tennakoon, C., Shayan, A., Sanjayan, J. G. & Xu, A. Chloride ingress and steel corrosion in geopolymer concrete based on long term tests. *Materials & Design* **116**, 287–299 (2017).

118. Babaee, M. & Castel, A. Chloride-induced corrosion of reinforcement in low-calcium fly ash-based geopolymer concrete. *Cement and Concrete Research* **88**, 96–107 (2016).

119. Noushini, A. & Castel, A. The effect of heat-curing on transport properties of low-calcium fly ash-based geopolymer concrete. *Construction and Building Materials* **112**, 464–477 (2016).

120. Duan, W., Lopez, M., Juenger, M. C. G., Aughenbaugh, K. L. & Stutzman, P. identifying glass compositions in Fly ash. *Frontiers in Materials* **3**, 1 (2016).

121. Komljenović, M., Baščarević, Z. & Bradić, V. Mechanical and microstructural properties of alkali-activated fly ash geopolymers. *Journal of Hazardous Materials* **181**, 35–42 (2010).

122. Fernández-Jiménez, A. & Palomo, A. Characterisation of fly ashes. Potential reactivity as alkaline cements. *Fuel* **82**, 2259–2265 (2003).

123. Helmuth, R. A. *Fly Ash in Cement and Concrete*. (1987).

124. Manz, O. E. Coal fly ash: A retrospective and future look. *Fuel* **78**, 133–136 (1999).

125. Dunstan, E. R. What is a "Practical" (ASTM C 618) SAI--Strength Activity Index for Fly Ashes that can be used to Proportion Concretes Containing Fly Ash? in *2017 World of Coal Ash (WOCA) Conference* 25 (2017).

126. Monticelli, C. *et al.* A study on the corrosion of reinforcing bars in alkali-activated fly ash mortars under wet and dry exposures to chloride solutions. *Cement and Concrete Research* **87**, 53–63 (2016).

127. Criado, M., Bastidas, D. M., Fajardo, S., Fernández-Jiménez, A. & Bastidas, J. M. Corrosion behaviour of a new low-nickel stainless steel embedded in activated fly ash mortars. *Cement and Concrete Composites* **33**, 644–652 (2011).

128. Sweeney, J., Htut, T., Huen, W. Y. & Vimonsatit, V. Investigating Amorphous Composition Mix Design Performance and Properties of Fly Ash-Based Geopolymer. *Electronic Journal of Structural Engineering* **17**, 33-42 (2017).

129. Nuaklong, P., Sata, V. & Chindaprasirt, P. Properties of metakaolin-high calcium fly ash geopolymer concrete containing recycled aggregate from crushed concrete specimens. *Construction and Building Materials* **161**, 365–373 (2018).

130. Yi, C. *et al.* Study on chloride binding capability of coal gangue based cementitious materials. *Construction and Building Materials* **167**, 649–656 (2018).

131. Velandia, D. F., Lynsdale, C. J., Provis, J. L. & Ramirez, F. Effect of mix design inputs, curing and compressive strength on the durability of Na_2SO_4 -activated high volume fly ash concretes. *Cement and Concrete Composites* **91**, 11-20 (2018).

132. Dehghan, A., Peterson, K., Riehm, G. & Herzog Bromerchenkel, L. Application of X-ray microfluorescence for the determination of chloride diffusion coefficients in concrete chloride penetration experiments. *Construction and Building Materials* **148**, 85–95 (2017).

133. Newlands, K. C. & Macphee, D. E. The reactivity of aluminosilicate glasses in cements– effects of Ca content on dissolution characteristics and surface precipitation. *Advances in Applied Ceramics* **116**, 216–224 (2017).

134. Galibert, R. GLASS CONTENT INFLUENCE UPON HYDRAULIC POTENTIAL OF BLAST - FURNACE SLAG. *NATIONAL SLAG ASSOCIATION* 5–8.

135. Bernal, S. A. *et al.* Characterization of supplementary cementitious materials by thermal analysis. *Materials and Structures* **50**, 1–13 (2016).

136. Khale, D. & Chaudhary, R. Mechanism of geopolymerization and factors influencing its development: A review. *Journal of Materials Science* **42**, 729–746 (2007).

137. Shvarzman, A., Kovler, K., Grader, G. S. & Shter, G. E. The effect of dehydroxylation/amorphization degree on pozzolanic activity of kaolinite. *Cement and Concrete Research* **33**, 405–416 (2003).

138. Bumanis, G., Vitola, L., Bajare, D., Dembovska, L. & Pundiene, I. Impact of reactive SiO_2/Al_2O_3ratio in precursor on durability of porous alkali activated materials. *Ceramics International* **43**, 5471–5477 (2017).

139. Najimi, M., Ghafoori, N. & Sharbaf, M. Alkali-activated natural pozzolan/slag mortars: A parametric study. *Construction and Building Materials* **164**, 625–643 (2018).

140. Najimi, M., Ghafoori, N., Radke, B., Sierra, K. & Sharbaf, M. Comparative Study of Alkali-Activated Natural Pozzolan and Fly Ash Mortars. *Journal of Materials in Civil Engineering* **30** (2018).

141. Khale, D. & Chaudhary, R. Mechanism of geopolymerization and factors influencing its development: A review. *Journal of Materials Science* **42**, 729–746 (2007).

142. Provis, J. L. & Palomo, A. Advances in understanding alkali-activated materials. *Cement and Concrete Research* **78**, 110–125 (2015).

143. Ariffin, M. A. M. & Hussin, M. W. Chloride resistance of blended ash geopolymer concrete. *Journal of Civil Engineering, Science and Technology* **6**, 23–33 (2015).

144. Lloyd, R. R., Provis, J. L., Smeaton, K. J. & van Deventer, J. S. J. Spatial distribution of pores in fly ash-based inorganic polymer gels visualised by Wood's metal intrusion. *Microporous and Mesoporous Materials* **126**, 32–39 (2009).

145. Duan, P., Yan, C. & Zhou, W. Influence of partial replacement of fly ash by metakaolin on mechanical properties and microstructure of fly ash geopolymer paste exposed to sulfate attack. *Ceramics International* **42**, 3504–3517 (2015).

146. Fernandez-Jimenez, A., García-Lodeiro, I. & Palomo, A. Durability of alkali-activated fly ash cementitious materials. *Journal of Materials Science* **42**, 3055–3065 (2007).

147. Ke, X., Bernal, S. A., Hussein, O. H. & Provis, J. L. Chloride binding and mobility in sodium carbonate-activated slag pastes and mortars. *Materials and Structures* **50**, 252 (2017).

148. Ke, X., Criado, M., Provis, J. L. & Bernal, S. A. Slag-Based Cements That Resist Damage Induced by Carbon Dioxide. *ACS Sustainable Chemistry & Engineering* **6**, 5067–5075 (2018).

149. Ke, X., Bernal, S. A. & Provis, J. Assessing the chloride binding capacity of synthetic cementitious phases in alkali- activated slag simulated pore solution. *Ist International Conference on Construction Materials for Sustainable Future* (2017).

150. Walkley, B., Nicolas, R. S., Bernal, S. A., Provis, J. L. & Sani, M. The role of MgO content in the phase assemblage of alkali-activated synthetic precursors within the system CaO-MgO-Al_2O_3 -SiO_2. *14th International Congress on the Chemistry of Cement* (2015).

151. Walkley, B. *et al.* Synthesis of stoichiometrically controlled reactive aluminosilicate and calcium-aluminosilicate powders. *Powder Technology* **297**, 17–33 (2016).

152. Bernal, S. A. *et al.* MgO content of slag controls phase evolution and structural changes induced by accelerated carbonation in alkali-activated binders. *Cement and Concrete Research* **57**, 33–43 (2014).

153. Silva, P. De, Sagoe-Crenstil, K. & Sirivivatnanon, V. Kinetics of geopolymerization: Role of Al_2O_3 and SiO_2. *Cement and Concrete Research* **37**, 512–518 (2007).

154. Ke, X., Bernal, S. A. & Provis, J. L. Controlling the reaction kinetics of sodium carbonate-activated slag cements using calcined layered double hydroxides. *Cement and Concrete Research* **81**, 24–37 (2016).

155. Ke, X., Bernal, S. A. & Provis, J. L. CHLORIDE BINDING CAPACITY OF SYNTHETIC C - (A) - S - H TYPE GELS IN ALKALI - ACTIVATED SLAG SIMULATED PORE SOLUTIONS.

156. Ke, X., Bernal, S. A. & Provis, J. L. Uptake of chloride and carbonate by Mg-Al and Ca-Al layered double hydroxides in simulated pore solutions of alkali-activated slag cement. *Cement and Concrete Research* **100**, 1–13 (2017).

157. Khan, M. S. H. & Kayali, O. Chloride binding ability and the onset corrosion threat on alkali-activated GGBFS and binary blend pastes. *European Journal of Environmental and Civil Engineering* 22,1–17 (2016).

158. Jun, Y., Yoon, S. & Oh, J. A Comparison Study for Chloride-Binding Capacity between Alkali-Activated Fly Ash and Slag in the Use of Seawater. *Applied Sciences* **7**, 971 (2017).

159. Weitkamp, J. Zeolites and catalysis. *Solid State Ionics* **131**, 175–188 (2000).

160. Ofer-Rozovsky, E., Arbel Haddad, M., Bar Nes, G. & Katz, A. The formation of crystalline phases in metakaolin-based geopolymers in the presence of sodium nitrate. *Journal of Materials Science* **51**, 4795–4814 (2016).

161. Huang, X., Hu, S., Wang, F., Liu, Y. & Mu, Y. Properties of alkali-activated slag with addition of cation exchange material. *Construction and Building Materials* **146**, 321–328 (2017).

162. Tänzer, R., Jin, Y. & Stephan, D. Alkali activated slag binder: effect of cations from silicate activators. *Materials and Structures* **50**, 91 (2017).

163. Fernández-Jiménez, A., Palomo, A. & Criado, M. Microstructure development of alkali-activated fly ash cement: a descriptive model. *Cement and Concrete Research* **35**, 1204–1209 (2005).

164. Xu, H. & Van Deventer, J. S. J. The geopolymerisation of alumino-silicate minerals. *International Journal of Mineral Processing* **59**, 247–266 (2000).

165. van Deventer, J. S. J., Provis, J. L., Duxson, P. & Lukey, G. C. Reaction mechanisms in the geopolymeric conversion of inorganic waste to useful products. *Journal of Hazardous Materials* **139**, 506–513 (2007).

166. Xie, Z. & Xi, Y. Hardening mechanisms of an alkaline-activated class F fly ash. *Cement and Concrete Research* **31**, 1245–1249 (2001).

167. Blyth, A., Eiben, C. A., Scherer, G. W. & White, C. E. Impact of activator chemistry on permeability of alkali-activated slags. *Journal of the American Ceramic Society* **100**, 4848–4859 (2017).

168. Krivenko, P. V., Cao, H. L., Weng, L. Q. & Petropavlovskii, O. N. High-Performance Alkali-Activated Cement Concretes for Marine Engineering Applications. in *High Performance Concrete Technology and Applications* (InTech, 2016).

169. Zhang, Z., Provis, J. L., Wang, H., Bullen, F. & Reid, A. Quantitative kinetic and structural analysis of geopolymers. Part 2. Thermodynamics of sodium silicate activation of metakaolin. *Thermochimica Acta* **565**, 163–171 (2013).

170. Garcia-Lodeiro, I., Fernandez-Jimenez, A. & Palomo, A. Hydration kinetics in hybrid binders: Early reaction stages. *Cement and Concrete Composites* **39**, 82–92 (2013).

171. Bastidas, D. M., Fernández-Jiménez, A., Palomo, A. & González, J. A. A study on the passive state stability of steel embedded in activated fly ash mortars. *Corrosion Science* **50**, 1058–1065 (2008).

172. Mundra, S., Criado, M., Bernal, S. A. & Provis, J. L. Chloride-induced corrosion of steel rebars in simulated pore solutions of alkali-activated concretes. *Cement and Concrete Research* **100**, 385–397 (2017).

173. Deir, E., Gebregziabiher, B. S. & Peethamparan, S. Influence of starting material on the early age hydration kinetics, microstructure and composition of binding gel in alkali activated binder systems. *Cement and Concrete Composites* **48**, 108–117 (2014).

174. Shi, J., Ming, J. & Sun, W. Passivation and chloride-induced corrosion of a duplex alloy steel in alkali-activated slag extract solutions. *Construction and Building Materials* **155**, 992–1002 (2017).

175. Katz, A. Microscopic study of alkali-activated fly ash. *Cement and Concrete Research* **28**, 197–208 (1998).

176. Yang, K., Yang, C., Magee, B., Nanukuttan, S. & Ye, J. Establishment of a preconditioning regime for air permeability and sorptivity of alkali-activated slag concrete. *Cement and Concrete Composites* **73**, 19–28 (2016).

177. Giasuddin, H. M., Sanjayan, J. G. & Ranjith, P. G. Strength of geopolymer cured in saline water in ambient conditions. *Fuel* **107**, 34–39 (2013).

178. Lee, N. K. & Lee, H. K. Influence of the slag content on the chloride and sulfuric acid resistances of alkali-activated fly ash/slag paste. *Cement and Concrete Composites* **72**, 168–179 (2016).

179. Promentilla, M. A. B., Sugiyama, T., Hitomi, T. & Takeda, N. Quantification of tortuosity in hardened cement pastes using synchrotron-based X-ray computed microtomography. *Cement and Concrete Research* **39**, 548–557 (2009).

180. Games, P. A., Keselman, H. J. & Clinch, J. J. Tests for homogeneity of variance in factorial designs. *Psychological Bulletin* **86**, 978–984 (1979).

181. Kupwade-Patil, K., Allouche, E. N. & Eng, P. Examination of Chloride-Induced Corrosion in Reinforced Geopolymer Concretes. *Journal of Materials in Civil Engineering* **25**, 1465–1476 (2012).

182. Ismail, I., Bernal, S. A., Provis, J. L., Hamdan, S. & Van Deventer, J. S. J. Drying-induced changes in the structure of alkali-activated pastes. *Journal of Materials Science* **48**, 3566–3577 (2013).

183. Caré, S. Influence of aggregates on chloride diffusion coefficient into mortar. *Cement and Concrete Research* **33**, 1021–1028 (2003).

184. Li, W., Pour-Ghaz, M., Castro, J. & Weiss, J. Water Absorption and Critical Degree of Saturation Relating to Freeze-Thaw Damage in Concrete Pavement Joints. *Journal of Materials in Civil Engineering* **24**, 299–307 (2012).

185. Bu, Y. & Weiss, J. The influence of alkali content on the electrical resistivity and transport properties of cementitious materials. *Cement and Concrete Composites* **51**, 49–58 (2014).

186. Andrade, C. Calculation of chloride diffusion coefficients in concrete from ionic migration measurements. *Cement and Concrete Research* **23**, 724–742 (1993).

187. Noushini, Amin Castel, A. A resistivity-Based Approach to Indicate Chloride Permeability of Geopolymer Concrete. in *Concrete 2015* 10 (Researchgate, 2015).

188. Ravikumar, D. & Neithalath, N. An electrical impedance investigation into the chloride ion transport resistance of alkali silicate powder activated slag concretes. *Cement and Concrete Composites* **44**, 58–68 (2013).

189. Jason Weiss, W., Spragg, R. P., Burkan Isgor, O., Tyler Ley, M. & Van Dam, T. Toward performance specifications for concrete: Linking resistivity, RCPT and diffusion predictions using the formation factor for use in specifications. in *High Tech Concrete: Where Technology and Engineering Meet - Proceedings of the 2017 fib Symposium* 2057–2065 (Springer International Publishing, 2017).

190. Provis, J. L., Myers, R. J., White, C. E., Rose, V. & van Deventer, J. S. J. X-ray microtomography shows pore structure and tortuosity in alkali-activated binders. *Cement and Concrete Research* **42**, 855–864 (2012).

191. Ismail, I., Bernal, S. A., Provis, J. L., Hamdan, S. & Van Deventer, J. S. J. Drying-induced changes in the structure of alkali-activated pastes. *Journal of Materials Science* **48**, 3566–3577 (2013).

192. Criado, M., Bernal, S. A., Garcia-Triñanes, P. & Provis, J. L. Influence of slag composition on the stability of steel in alkali-activated cementitious materials. *Journal of Materials Science* **53**, 5016–5035 (2018).

193. Duxson, P. *et al.* Geopolymer technology: The current state of the art. *Journal of Materials Science* **42**, 2917–2933 (2007).

194. Osio-Norgaard, J., Gevaudan, J. P. & Srubar, W. V. A review of chloride transport in alkali-activated cement paste, mortar, and concrete. *Construction and Building Materials* **186**, 191–206 (2018).

195. Machner, A. *et al.* Chloride-binding capacity of hydrotalcite in cement pastes containing dolomite and metakaolin. *Cement and Concrete Research* **107**, 163–181 (2018).

196. Birnin-Yauri, U. A. & Glasser, F. P. Friedel?s salt, $Ca_2Al(OH)_6(Cl,OH)_2H_2O$: its solid solutions and their role in chloride binding. *Cement and Concrete Research* **28**, 1713–1723 (1998).

197. Vujaković, A. D., Tomašević-Čanović, M. R., Daković, A. S. & Dondur, V. T. The adsorption of sulphate, hydrogenchromate and dihydrogenphosphate anions on surfactant-modified clinoptilolite. *Applied Clay Science* **17**, 265–277 (2000).

198. NING, P., BART, H.-J., LI, B., LU, X. & ZHANG, Y. Phosphate removal from wastewater by model-La(III) zeolite adsorbents. *Journal of Environmental Sciences* **20**, 670–674 (2008).

199. Ruiz-Santaquiteria, C., Fernández-Jiménez, A., Skibsted, J. & Palomo, A. Clay reactivity: Production of alkali activated cements. *Applied Clay Science* **73**, 11–16 (2013).

200. Ruiz-Santaquiteria, C., Skibsted, J., Fernández-Jiménez, A. & Palomo, A. Alkaline solution/binder ratio as a determining factor in the alkaline activation of aluminosilicates. *Cement and Concrete Research* **42**, 1242–1251 (2012).

201. Li, N., Shi, C., Wang, Q., Zhang, Z. & Ou, Z. Composition design and performance of alkali-activated cements. *Materials and Structures* **50**, 178 (2017).

202. Uzal, B. & Turanlı, L. Blended cements containing high volume of natural zeolites: Properties, hydration and paste microstructure. *Cement and Concrete Composites* **34**, 101–109 (2012).

203. Xiaodong, S., Sheng, Y., Xuequan, W., Mingshu, T. & Liji, Y. Immobilization of stimulated high level wastes into AASC waste form. *Cement and Concrete Research* **24**, 133–138 (1994).

204. Vigil de la Villa, R., Fernández, R., García, R., Villar-Cociña, E. & Frías, M. Pozzolanic activity and alkaline reactivity of a mordenite-rich tuff. *Microporous and Mesoporous Materials* **126**, 125–132 (2009).

205. Hu, M., Zhu, X. & Long, F. Alkali-activated fly ash-based geopolymers with zeolite or bentonite as additives. *Cement and Concrete Composites* **31**, 762–768 (2009).

206. Rodríguez, E. D. *et al.* Geopolymers based on spent catalyst residue from a fluid catalytic cracking (FCC) process. *Fuel* **109**, 493–502 (2013).

207. Cornejo, M. H. *et al.* Effect of Calcium Hydroxide and Water to Solid Ratio on Compressive Strength of Mordenite-Based Geopolymer and the Evaluation of its Thermal Transmission Property. in *Volume 12: Materials: Genetics to Structures* **12**, 11-22 (ASME, 2018)..

208. Lynch, J. L. V., Baykara, H., Cornejo, M., Soriano, G. & Ulloa, N. A. Preparation, characterization, and determination of mechanical and thermal stability of natural zeolite-based foamed geopolymers. *Construction and Building Materials* **172**, 448–456 (2018).

209. Rożek, P., Król, M. & Mozgawa, W. Geopolymer-zeolite composites: A review. *Journal of Cleaner Production* **230**, 557–579 (2019).

210. Hermassi, M. *et al.* Powdered Ca-activated zeolite for phosphate removal from treated waste-water. *Journal of Chemical Technology & Biotechnology* **91**, 1962–1971 (2016).

211. Castaldi, P., Santona, L., Enzo, S. & Melis, P. Sorption processes and XRD analysis of a natural zeolite exchanged with Pb^{2+}, Cd^{2+} and Zn^{2+} cations. *Journal of Hazardous Materials* **156**, 428–434 (2008).

212. Jha, B. & Singh, D. N. Fly Ash Zeolites. **78**, (2016).

213. Juenger, M., Winnefeld, F., Provis, J. L. & Ideker, J. Advances in alternative cementitious binders. *Cement and concrete research* **41**, 1232–1243 (2011).

214. Gevaudan, J. P., Osio-Norgaard, J. & Srubar, W. V. Alternative Cements: Recent Developments and Future Directions. in *AEI 2019* 294–308 (American Society of Civil Engineers, 2019). doi:10.1061/9780784482261.035.

215. Walkley, B. *et al.* A New Structural Model of Sodium Aluminosilicate Gels and the Role of Charge Balancing Extra-Framework Al. *The Journal of Physical Chemistry C* **4**, acs.jpcc.8b00259 (2018).

216. Duxson, P., Provis, J. L., Lukey, G. C. & van Deventer, J. S. J. The role of inorganic polymer technology in the development of 'green concrete'. *Cement and Concrete Research* **37**, 1590–1597 (2007).

217. Xu, Z. *et al.* Immobilization of strontium-loaded zeolite A by metakaolin based-geopolymer. *Ceramics International* **43**, 4434–4439 (2017).

218. Kirkpatrick, T. J., Weyers, R. E., Anderson-Cook, C. M. & Sprinkel, M. M. Immobilization of Cr^{6+}, Cd^{2+}, Zn^{2+} and Pb^{2+} in alkali-activated slag binders. *Cement and Concrete Research* **32**, 1971–1979 (2002).

219. Cruciani, G. Zeolites upon heating: Factors governing their thermal stability and structural changes. *Journal of Physics and Chemistry of Solids* **67**, 1973–1994 (2006).

220. Sturm, P., Gluth, G. J. G., Jäger, C., Brouwers, H. J. H. & Kühne, H. C. Sulfuric acid resistance of one-part alkali-activated mortars. *Cement and Concrete Research* **109**, 54–63 (2018).

221. Javadian, H., Ghorbani, F., Tayebi, H. & Asl, S. H. Study of the adsorption of Cd (II) from aqueous solution using zeolite-based geopolymer, synthesized from coal fly ash; kinetic, isotherm and thermodynamic studies. *Arabian Journal of Chemistry* **8**, 837–849 (2015).

222. Li, Y. *et al.* Removal of Zn $^{2+}$, Pb $^{2+}$, Cd $^{2+}$, and Cu $^{2+}$ from aqueous solution by synthetic clinoptilolite. *Microporous and Mesoporous Materials* **203**, 203-211 (2019).

223. Cundy*, C. S. & Cox, P. A. The Hydrothermal Synthesis of Zeolites: History and Development from the Earliest Days to the Present Time. *Chem. Rev.* **103**, 663–702 (2003).

224. Cundy, C. S. & Cox, P. A. The hydrothermal synthesis of zeolites: Precursors, intermediates and reaction mechanism. *Microporous and Mesoporous Materials* **82**, 1–78 (2005).

225. Gómez-Hortigüela, L. & Camblor, M. Á. Introduction to the Zeolite Structure-Directing Phenomenon by Organic Species: General Aspects. in *Structure and Bonding* **119**, 193–223 (Springer, Berlin, Heidelberg, 2017).

226. Davis, M. E. & Lobo, R. F. Zeolite amd Molecular Sieve Synthesis. *Chemical Materials* **4**, 756–768 (1992).

227. Amrhein, C. *et al.* Synthesis and properties of zeolites from coal fly ash. *Environmental Science & Technology* **30**, 735–742 (1996).

228. Carreon, M. A., Li, S., Falconer, J. L. & Noble, R. D. SAPO-34 seeds and membranes prepared using multiple structure directing agents. *Advanced Materials* **20**, 729–732 (2008).

229. Gallego, E. M. *et al.* Simple organic structure directing agents for synthesizing nanocrystalline zeolites. *Chemical Science* **12**, (2017).

230. Burkett, S. L. & Davis, M. E. Mechanism of Structure Direction in the Synthesis of Pure-Silica Zeolites. 2. Hydrophobic Hydration and Structural Specificity. *Chemistry of Materials* **7**, 1453–1463 (1995).

231. Xiao, F.-S. & Meng, X. *Zeolites in Sustainable Chemistry*. (Springer, 2016).

232. Olivas, A., Ferraris, C. F., Guthrie, W. & Toman, B. *Re-Certification of SRM 2492: Bingham Paste Mixture for Rheological Measurements*. (2015).

233. Ferraris, C. F. Measurement of the rheological properties of high performance concrete: State of the art report. *Journal of Research of the National Institute of Standards and Technology* **104**, 461 (1999).

234. Zhang, Z. *et al.* Effect of drying procedures oaftn pore structure and phase evolution of alkali-activated cements. *Cement and Concrete Composites* **96**, 194–203 (2019).

235. Scherer, G. W. Effect of shrinkage on the modulus of silica gel. *Journal of Non-Crystalline Solids* **109**, 183–190 (1989).

236. Poulesquen, A., Frizon, F. & Lambertin, D. Rheological behavior of alkali-activated metakaolin during geopolymerization. *Journal of Non-Crystalline Solids* **357**, 3565–3571 (2011).

237. Favier, A., Hot, J., Habert, G., Roussel, N. & D'Espinose De Lacaillerie, J. B. Flow properties of MK-based geopolymer pastes. A comparative study with standard Portland cement pastes. *Soft Matter* **10**, 1134–1141 (2014).

238. McCormick, A., Bell, A. & Radke, C. Multinuclear NMR investigation of the formation of aluminosilicate anions. *The Journal of Physical Chemistry* **93**, 1741–1744 (1989).

239. Criado, M., Fernández-Jiménez, A., Palomo, A., Sobrados, I. & Sanz, J. Effect of the SiO2/Na2O ratio on the alkali activation of fly ash. Part II: 29Si MAS-NMR Survey. *Microporous and Mesoporous Materials* **109**, 525–534 (2008).

240. Provis, J. L., Duxon, P, Lukey G. C., Separovic, F., Kriven W. M., Deventer J. S. J., Modeling Speciation in Highly Concentrated Alkaline Silicate Solutions. *Industrial Engineering Chemistry Research.* **44**, 8899–8908 (2005).

241. Jelfs, K. E., Slater, B., Lewis, D. W. & Willock, D. J. The role of organic templates in controlling zeolite crystal morphology. in *Studies in surface science and catalysis* **170**, 1685–1692 (Elsevier, 2007).

242. Xu, R., Chen, J., Gao, Z. & Yan, W. *From Zeolites to Porous MOF Materials-the 40th Anniversary of International Zeolite Conference, 2 Vol Set: Proceedings of the 15th International Zeolite Conference, Beijing, PR China, 12-17th August 2007*. (Elsevier, 2007).

243. Gittleman, C., Watanabe, K., Bell, A. & Radke, C. A mechanistic study of the synthesis of zeolite SSZ-24. *Microporous materials* **6**, 131–150 (1996).

244. Romagnoli, M., Leonelli, C., Kamse, E. & Lassinantti Gualtieri, M. Rheology of geopolymer by DOE approach. *Construction and Building Materials* **36**, 251–258 (2012).

245. Baur, W. H. On the cation and water positions in faujasite. *American Mineralogist: Journal of Earth and Planetary Materials* **49**, 697–704 (1964).

246. Calligaris, M., Nardin, G. & Randaccio, L. Cation site location in hydrated chabazites. Crystal structure of potassium-and silver-exchanged chabazites. *Zeolites* **3**, 205–208 (1983).

247. Felsche, J., Luger, S. & Baerlocher, C. Crystal structures of the hydro-sodalite Na_6 [$AlSiO_4$] $_6 8H_2O$ and of the anhydrous sodalite Na6 [AlSiO4] 6. *Zeolites* **6**, 367–372 (1986).

248. Ji, Y., Wang, Y., Xie, B. & Xiao, F. S. Zeolite Seeds: Third Type of Structure Directing Agents in the Synthesis of Zeolites. *Comments on Inorganic Chemistry* **36**, 1–16 (2016).

249. Burkett, S. L. & Davis, M. E. Mechanism of Structure Direction in the Synthesis of Si-ZSM-5 : An Investigation by Intermolecular 1H-29Si CP MAS NMR Mechanism of Structure Direction in the Synthesis of Si-ZSM-5 : An Investigation by Intermolecular 1H-29Si CP MAS NMR. *Journal of Physical Chemistry* **98**, 4647–4653 (1994).

250. Catlow, C. R. A., Coombes, D. S., Lewis, D. W. & Pereira, J. C. G. Computer Modeling of Nucleation, Growth, and Templating in Hydrothermal Synthesis. *Chemistry of Materials* **10**, 3249–3265 (1998).

251. Jorge, M., Auerbach, S. M. & Monson, P. A. Modeling spontaneous formation of precursor nanoparticles in clear-solution zeolite synthesis. in *AIChE Annual Meeting, Conference Proceedings* 13926 (American Chemical Society, 2005).

252. Lloyd, R. Accelerated ageing of geopolymers. in *Geopolymers* 139–166 (Elsevier, 2009).

253. Moliner, M., Rey, F. & Corma, A. Towards the Rational Design of Efficient Organic Structure□Directing Agents for Zeolite Synthesis. *Angewandte Chemie International Edition* **52**, 13880–13889 (2013).

254. Criado, M., Fernández-Jiménez, A. & Palomo, A. Alkali activation of fly ash. Part III: Effect of curing conditions on reaction and its graphical description. *Fuel* **89**, 3185–3192 (2010).

255. McCormick, A. V., Bell, A. T. & Radke, C. J. Quantitative determination of siliceous species in sodium silicate solutions by 29Si n.m.r. spectroscopy. *Zeolites* **7**, 183–190 (1987).

256. Hould, N. D., Foster, A. & Lobo, R. F. Zeolite beta mechanisms of nucleation and growth. *Microporous and Mesoporous Materials* **142**, 104–115 (2011).

257. Zones, S. I. Conversion of faujasites to high-silica chabazite SSZ-13 in the presence of N,N,N-trimethyl-1-adamantammonium iodide. *Journal of the Chemical Society, Faraday Transactions* **87**, 3709–3716 (1991).

258. Zones, S. I., Hwang, S. & Davis, M. E. Studies of the Synthesis of SSZ□25 Zeolite in a "Mixed□Template" System. *Chemistry – A European Journal* **7**, 1990–2001 (2001).

259. Chen, X., Sutrisno, A., Zhu, L. & Struble, L. J. Setting and nanostructural evolution of metakaolin geopolymer. *Journal of the American Ceramic Society* **100**, 2285–2295 (2017).

260. Suraneni, P. *et al.* Monitoring Setting of Geopolymers. *Advances in Civil Engineering Materials* **3**, 177–192 (2014).

261. Pacheco-Torgal, F., Abdollahnejad, Z., Camões, A. F., Jamshidi, M. & Ding, Y. Durability of alkali-activated binders: A clear advantage over Portland cement or an unproven issue? *Construction and Building Materials* **30**, 400–405 (2012).

262. Mastali, M., Kinnunen, P., Dalvand, A., Mohammadi Firouz, R. & Illikainen, M. Drying shrinkage in alkali-activated binders – A critical review. *Construction and Building Materials* **190**, 533–550 Preprint at https://doi.org/10.1016/j.conbuildmat.2018.09.125 (2018).

263. Thompson, J. F. *et al.* Intrinsic Thermal Desorption in a 3D Printed Multifunctional Composite CO_2 Sorbent with Embedded Heating Capability. *ACS Applied Materials & Interfaces* **11**, 43337–43343 (2019)

264. Scott, A., Oze, C. & Hughes, M. W. Magnesium-Based Cements for Martian Construction. *Journal of Aerospace Engineering* **33**, (2020).

265. Sakamoto, K. & Wajima, T. PREPARATION OF GEOPOLYMER CEMENT FROM SIMULATED LUNAR ROCK SAND USING ALKALI FUSION. *International Journal of GEOMATE* **18**, 62–67 (2020).

266. Buchner, C., Pawelke, R. H., Schlauf, T., Reissner, A. & Makaya, A. A new planetary structure fabrication process using phosphoric acid. *Acta Astronautica* **143**, 272–284 (2018).

267. Walling, S. A., Provis, J. L., Magnesia-Based Cements: A Journey of 150 Years, and Cements for the Future? *Chemical Reviews.* **116**, 4170-4204 (2016)

268. Cole, W. F. & Demediuk, T. X-Ray, thermal, and Dehydration studies on Magnesium oxychlorides. *Australian Journal of Chemistry* **8**, 234–251 (1955).

269. Li, Z. & Chau, C. K. Influence of molar ratios on properties of magnesium oxychloride cement. *Cement and Concrete Research* **37**, 866–870 (2007).

270. Chen, X., Zhang, Y., Hui, D., Chen, M. & Wu, Z. Study of melting properties of basalt based on their mineral components. *Composites Part B: Engineering* **116**, 53–60 (2017).

271. LaTourrette, T. & Wasserburg, G. J. Mg diffusion in anorthite: implications for the formation of early solar system planetesimals. *Earth and Planetary Science Letters* **158**, 91–108 (1998).

272. Chan, J. The development of magnesium oxychloride cement as repairing materials. (The Hong Kong University of Science and Technology, 2006).

273. Averina, G. F., Chernykh, T. N. & Kramar, L. Y. Investigation of Interrelation between Deformation, Composition and Structural Characteristics of Magnesium Oxychloride Cements. *IOP Conf. Ser.: Mater. Sci. Eng.* **262** (2017).

274. Blacic, J. D. *Mechanical properties of lunar materials under anhydrous, hard vacuum conditions: applications of lunar glass structural components* (1984).

275. Mei, H. *et al.* Effects of water on the mechanical properties of silica glass using molecular dynamics. *Acta Materialia* **178**, 36–44 (2019).

276. Spedding, C. P., Nuttall, W. J. & Lim, S. Energy requirements of a thermally processed ISRU radiation shield for a lunar habitat. *Advances in Space Research* **65**, 2467–2474 (2020).

277. Colozza, A. J. Analysis of Lunar Regolith Thermal Energy Storage. 9.

278. Mottaghi, S. & Benaroya, H. Design of a Lunar Surface Structure. I: Design Configuration and Thermal Analysis. *Journal of Aerospace Engineering* **28**, (2015).

279. Vahidi, G. *et al.* Bone biomechanical properties and tissue-scale bone quality in a genetic mouse model of familial dysautonomia. *Osteoporos Int* **32**, 2335–2346 (2021).

280. Farjana, S. H., Huda, N. & Mahmud, M. A. P. Impacts of aluminum production: A cradle to gate investigation using life-cycle assessment. *Science of The Total Environment* **663**, 958–970 (2019).

281. Xia, Y., Lefler, H. D., Fang, Z. Z., Zhang, Y. & Sun, P. Chapter 17 - Energy consumption of the Kroll and HAMR processes for titanium production. in *Extractive Metallurgy of Titanium* (eds. Fang, Z. Z., Froes, F. H. & Zhang, Y.) 389–410 (Elsevier, 2020).

282. Khater, G. A. Influence of Cr2O3, LiF, CaF2 and TiO2 nucleants on the crystallization behavior and microstructure of glass-ceramics based on blast-furnace slag. *Ceramics International* **37**, 2193–2199 (2011).

283. Morales, R. E., Harke, K. J., Tringe, J. W., Stobbe, D. M. & Murray, T. W. Real-time laser ultrasonic monitoring of laser-induced thermal processes. *Scientific Reports* **12**, 1–11 (2022).